THREE DIMENSIONAL KINEMATICS OF LOCAL LUMINOUS COMPACT BLUE GALAXIES

By

JORGE PÉREZ GALLEGO

A DISSERTATION PRESENTED TO THE GRADUATE SCHOOL
OF THE UNIVERSITY OF FLORIDA IN PARTIAL FULFILLMENT
OF THE REQUIREMENTS FOR THE DEGREE OF
DOCTOR OF PHILOSOPHY

UNIVERSITY OF FLORIDA

2009

To my sister, mother, and grandmother

ACKNOWLEDGMENTS

And then, one morning,

after a quiet night's sleep,

you realize there are just two kinds of travelers.

There are those who depart,

and there are those who return.

The former wander around maps,

the latter look for themselves in the mirror.

And then, one morning,

after a quiet night's sleep,

you realize life is a journey.

And you need to figure out,

what is that you have in front of your eyes.

Mirrors or maps?

And then, one morning,

after a quiet night's sleep,

you let go one tear,

and draw a bittersweet smile.

And then, one morning,

after a quiet night's sleep,

you wake up.

Is there someone there?

You$^{\heartsuit}$ were,

and I thank you for that.

♡ *You* are:

- *Anna, Marta, & Mireia:* I thank you for defining friendship for me.
- *Nuria, Trinidad, & Trinidad:* I thank you for the way you look at me.
- *aNnA:* I thank you for opening my mind to the arts of the soul.
- *Anna:* I thank you for sharing random useless thoughts with me.
- *Bruno:* I thank you not only for being there all these years and the quality time we have spent together, but for making of "The Temple of Love" a state o mind I was proud to achieve. A state of mind that will always swim, ride, and run with us
- *Carlos:* I thank you for being there since you were born, for being like a brother to me, and for letting me be like a brother to you.
- *Constantino:* I thank you for planting my garden with curiosity only when the soil was ready.
- *Heidi:* I thank you for your strength, and your ability to pass it on to the people you love.
- *María:* I thank you for unknowingly teaching me how to fly.
- *Manuel:* I thank you for showing me the way even though you left the train for love and I respect you for that.
- *Miguel:* I thank you for asking me nothing and quietly waiting for the answers I have been willing to give.
- *Rafael:* I do not thank you for what graduate students usually thank their advisors. I do not thank you for giving me the opportunity to work on such an interesting project. I do not thank you for many enlightening scientific conversations. I do not thank you for your advices. I thank you for listening to me with both your mind and your heart.
- *Soung-Chul:* I thank you for being patient with me every single time I have started singing to "Don't Stop Believing" by Journey.
- *Sun Mi:* I thank you for letting yourself believe that change is possible.
- *Zeus:* I thank you for letting your inner self build a symbiotic relationship with mine.
- *Krishna Lunch:* I thank you for feeding me for the past five years and eight months.

- *The A-Team:* I thank you, Jairo, Teo, Norberto, and Rubén, for encouraging me to take the chance and cross the Atlantic.

- *Collaborators:* I thank you for being patient with my patience. I am specially thankful to África, Ana, Carlos, Catherine, and Daniel.

- *Officemates:* I thank Margaret's sweet treats, Lauren's English lectures, Carlos' funny jokes, Joanna's dance moves, Izaskun's quiet silence, Mark's soda empire, Enrique's isolated guffaws, Conor's drilling keyboard, and Ji's hidden cookies. I thank all of you for succeeding at sharing an office with me. And I thank also those among the graduate students who were never that lucky. I will specially miss having shared one with Ileana, Paola, and Ashley.

- *Professors:* I thank some more than other, but I thank them all, since kindergarten to graduate school. Among those I will always remember Pep, Cesc, and María Dolores.

- *New Friends:* I thank those who have welcomed me with open arms in their lives, for as long as they might stay: Alix, Armando, Ashley, Beatriz, Brent, Coral, Esther, Eugenia, Iván, Javier, Kathryn, Lisa, Li Wei, Margarita, Rodrigo, Sarah, Víctor, and a fistful more.

- *Old Friends:* I thank those who were and no longer are, and those who were and will always be: Alicia, Begoña, Èlia, Ethel, Filomena, Gabriella, Irene, Jesús, Joan, Jordi, Jose Alejandro, Juan, Luis, Nayra, Raúl, Rosa, Víctor, and a fistful more.

TABLE OF CONTENTS

LIST OF TABLES

LIST OF FIGURES

Abstract of Dissertation Presented to the Graduate School
of the University of Florida in Partial Fulfillment of the
Requirements for the Degree of Doctor of Philosophy

THREE DIMENSIONAL KINEMATICS OF LOCAL LUMINOUS COMPACT BLUE GALAXIES

By

Jorge Pérez Gallego

May 2009

Chair: Rafael Guzmán
Major: Astronomy

In the local universe, galaxies fall into one of two populations: a star-forming "blue cloud" and a "red sequence" lacking star formation. At $z \sim 1.5$, however, the red sequence has yet to develop. Over the past 9 Gyr some process has quenched the enhanced star formation in blue galaxies, and caused them to evolve onto the "red sequence" by fading and/or merging of their stellar populations. While such a transformation may be occurring across the full range of masses, the highest rate of evolution occurs in massive starbursts at the luminous end of the blue cloud. These galaxies are the Luminous Compact Blue Galaxies (LCBGs). We use three dimensional (3D) optical spectroscopy observations of a representative sample of 22 local LCBGs to address the following three fundamental questions through the study of their kinematics: *(i) what processes are triggering the current starbust in LCBGs?* We use velocity maps to search for signatures of recent minor/major mergers/interactions that may be the trigger for the current enhanced star formation found in our sample. In addition, we look for nearby companions that could be interacting with these LCBGs. We find 5% of objects show evidence of a major merger and 10% of objects to show evidence of a minor merger. On the other hand, 45% of objects have a companion. This argues in favor of a companion as responsible for the enhanced star formation in these galaxies. *(ii) what processes are quenching the current starbust in LCBGs?* Velocity and velocity width maps, together with emission-line ratio maps, may reveal signatures of Active Galactic Nuclei (AGN) activity or supernova (SN)

driven galactic winds that could halt the current burst. We find 95% of objects with no evidence of AGN activity, and 5% of objects with clear evidence of AGN activity. On the other hand we find 27% of objects with spectrally resolved kinematic components in agreement with SN-driven galactic winds. This argues in favor of of these mechanisms not being typical in LCBGs. *(iii) What can the study of local LCBGs tell us about the distant population of LCBGs?* We provide velocity and velocity width maps of a representative sample of LCBGs that allow us to classify the kinematics of these galaxies between three different classes: Rotating Disks (RDs), Perturbed Rotation (PRs), and Complex Kinematics (CK). We find 48% of RDs, 28% of PRs, and 24% of CKs. We find for RDs rotational velocities that range between $\sim$50 and $\sim$200 km s^{-1} and dynamical masses that range between $\sim 1 \times 10^9$ and $\sim 3 \times 10^{10} M_\odot$. We find velocity widths of RDs, rather than accounting exclusively for the rotation nature of these objects, may account as well for other kinematic components, and may not be good tracers of their dynamical masses. We, therefore, need to be careful with dynamical mass estimates from integrated properties of distant LCBGs. Finally, we use 3D spectroscopy data of local LCBGs to simulate observations of distant LCBGs. These simulations may help in the correct interpretation and discussion of results linked to current and future observations of distant LCBGs, and compensate for any possible biases introduced by the intrinsic limitations of distant surveys.

CHAPTER 1
INTRODUCTION

1.1 Luminous Compact Blue Galaxies in the Distant Universe

If we were able to go on an instantaneous journey through the Universe we would be as close as we are now to disentangling the enigma of the physical processes that drive the formation and evolution of spiral and elliptical galaxies. At different epochs we would encounter different galaxy populations, but for them to evolve into different ones, we would have to wait for billions of years. However, by learning about the properties of different populations at different epochs we have already started to understand the physical mechanisms that drive the formation and evolution of galaxies. Observational cosmology today, with the inestimable help of the forthcoming new generation of instruments and observational facilities, is closer to solving the mysteries of the history of galaxy formation and evolution.

Nearby galaxies, according to their colors and absolute magnitudes, and their position in color-magnitude diagrams (CMDs; Blanton et al., 2003) fall into two categories: (i) those belonging to the "red sequence," typically brighter and redder; and (ii) those belonging to the "blue cloud," bluer. While the "blue cloud" extends along a wide range of luminosities and colors, the "red sequence" extends along a wide range of luminosities, and a narrow range of redder colors. An interesting recent finding is that in the nearby universe this bi-modality is not only seen in CMDs, but also in other diagrams such as the following: (i) the galaxy luminosity functions (LFs; Baldry et al., 2004; Bell et al., 2003); (ii) the galaxy stellar mass functions (Baldry et al., 2004; Balogh et al., 2004; Hogg et al., 2004); (iii) the star formation rates (SFRs; Kauffmann et al., 2003); (iv) the stellar population ages (Kauffmann et al., 2003); (v) the gas-to-stellar mass ratio (Kannappan, 2004); and (vi) the galaxy environment (Blanton et al., 2006).

Furthermore, the same color bi-modality has been observed up to $z \sim 1$ (Bell et al., 2004). CMD morphologies are rather constant over the last ∼9 Gyr, which suggests that

both area and location of the "red sequence" and the "blue cloud" are stable for such period of time. Nevertheless, there are well-established correlations between the number of red and blue galaxies and redshift.

The fraction of galaxies in the "red sequence" decreases with redshift, up to the point of being negligible by $z \sim 1.5$ (Driver et al., 1998; Bell et al., 2004; Faber et al., 2007). This behavior can be seen in the evolution of the optical and the infrared (IR) LFs of the "red sequence" galaxies with time. The number density of red $L^\star$ galaxies has grown by a factor of $\sim$10 in the last $\sim$9 Gyr. This growth implies that those galaxies that merged and evolved into red $L^\star$ galaxies must populate the "blue cloud" when the Universe was just $\sim$4 Gyr old.

On the other hand, we can take a similar look at the evolution of the ultraviolet (UV) and the optical LFs of the "blue cloud" galaxies with time. Instead of an increase, there has been a decrease with time in the number density of blue $L^\star$ galaxies for the past $\sim$9 Gyr. In particular, those galaxies that are brightest in the UV are the ones which have experienced the highest decrease ($\sim$30%; Schiminovich et al., 2005).

Since the Universe was $\sim$6 Gyr old, the average SFR per unit comoving volume–the so-called cosmic SFR–has decreased by an order of magnitude (Madau et al., 1998; Hogg et al., 1998; Hopkins, 2004; Lilly et al., 2007). It is well known that the main contributors to the cosmic SFR up to $z \sim 1$ are spiral galaxies (Madau et al., 1998; Hogg et al., 1998; Hopkins, 2004; Lilly et al., 2007). Nevertheless, at higher redshifts the star formation taking place in bulge-, irregular-, and interacting-like blue galaxies, becomes equally important.

From a morphological point of view, galaxies from the "blue cloud" are, up to $z \sim 1$, mostly spiral galaxies. Later Hubble type galaxies, or galaxies showing either bulge-, peculiar-, or interacting-like morphologies represent only up to 30% (Wolf et al., 2005; Bell et al., 2005; Ilbert et al., 2006). However, this galaxy population is responsible for most of

the observed number density evolution of the UV and the optical LFs for the past ∼9 Gyr (Arnouts et al., 2005; Zucca et al., 2006; Ilbert et al., 2006; Zamojski et al., 2007).

Furthermore, closer than $z \sim 1$, most of the star formation activity takes place in morphologically undisturbed galaxies. This suggests that while gas-rich mergers may be responsible for the enhanced star formation activity and peculiar morphologies of the rapid evolving population seen in the "blue cloud" beyond $z \sim 1$ (Zucca et al., 2006), they are not for the low star formation activity seen closer (Wolf et al., 2005; Bell et al., 2005; Zamojski et al., 2007). Gas supply and consumption in a quiescent mode accounts for the star formation activity closer than $z \sim 1$.

If all this is taken into account we are left with two different epochs, one closer and one further away than $z \sim 1$. Further away, we are left with a universe dominated by young, blue, active, late-type galaxies; while closer, we are left with a universe dominated by older, redder, quiescent, more massive, early-type galaxies. This implies that galaxies from the "blue cloud" must evolve into the "red sequence." In order for this to happen, galaxy merging and star formation quenching must play a role. Most massive, spheroidal-like early-type galaxies can be explained by means of mergers between less massive, disk-like galaxies. Furthermore, for the stellar populations of young, blue, active, late-type galaxies to age into the "red sequence" both the star formation and the gas supply need to fade away. With no gas left, stars cannot be formed anymore, and galaxies from the "blue cloud" enter the "red sequence" via "wet"–gas-rich–mergers, and then evolve along the "red sequence" via "dry"–stellar–mergers. Nevertheless, the physical processes that rule the migration of galaxies between these two populations starting at $z \sim 1.5$ are not yet understood.

This implies that a large fraction of today's red $L^\star$ galaxies ancestors must be visible among the galaxies in the "blue cloud" at $z \sim 1.5$ and later. The crux of the matter is to accurately establish which galaxy population or populations have these galaxies evolved into. So far, several scenarios have been proposed. If they are intrinsically low-mass

systems that rapidly consume their current supply of gas, they could fade and become present-day low-mass early-type galaxies, the so-called dwarf elliptical galaxies (Koo et al., 1994; Guzmán et al., 1996, 1997, 1998; Phillips et al., 1997; Noeske et al., 2006; Barton et al., 2006). On the other hand, if they are more massive systems they could fade little and remain luminous, becoming the centers of more massive disk galaxies (Phillips et al., 1997; Guzmán et al., 1998; Hammer et al., 2001; Barton & van Zee, 2001; Barton et al., 2006; Puech et al., 2006). Finally, if they remain luminous and blue, they could evolve into present-day Magellanic irregular or small spiral galaxies (Phillips et al., 1997; Guzmán et al., 1998; Barton et al., 2006).

One of the most intriguing observational clues to the origin of this galaxy bi-modality is the fact that while the "red sequence" extends along a wide range of masses, the "blue cloud" seems to be truncated at $M_\star \sim 3 \times 10^{10}\ M_\odot$ (Kauffmann et al., 2003). Therefore, stars need not to be formed anymore for such an upper limit to exist. Star formation quenching may play then an important role in galaxy evolution.

An interesting scenario is the one proposed by Cattaneo et al. (2006). According to Cattaneo et al. (2006), a massive halo quenching model is able to explain this truncation. Galaxies would grow along the blue sequence through cold filamentary flows until the host halo grows above a critical shock-heating mass ($M_{Halo} \sim 10^{12}\ M_\odot$) and, in consequence, the gas accretion is halted. After reaching this critical mass, galaxies from the "blue cloud" would redden and fade, moving up along the CMD towards the "red sequence". Once there, the bright end would be reached through "dry" mergers. At this point, mergers might combine with several other gas removal mechanisms such as starburst heating (Mihos & Hernquist, 1994; Sanders & Mirabel, 1996), supernova (SN) driven galactic winds (Murray et al., 2005), merger orbital energy injection (Cox et al., 2006), and active galactic nucleus (AGN) feedback (Granato et al., 2004; Springel et al., 2005). These phenomena have been already integrated in a unified model to explain the formation of spheroids, quasars, and black holes (Hopkins et al., 2006). Nevertheless,

the process of cold-flow induced or merger-triggered star formation, and the subsequent shutdown above the critical mass at later times (as well as its cause) are still to be studied in detail.

With all we have discussed so far in mind, if we wish to improve the current view on the origin of the galaxy color bi-modality and the evolution from the "blue cloud" into the "red sequence," the ubiquitous population of young, blue, active, late-type galaxies that dominate the universe beyond the transition epoch in the star formation history of the universe beyond $z \sim 1$, is one of our best candidates. Most of these galaxies are luminous, small, and blue (Ferguson et al., 2004). The typical $L^{\star}$ galaxy at $z > 1$, as seen in deep optical surveys, is neither a grand-design spiral, nor a massive elliptical, but a bright, small, blue, starburst galaxy. These are the so-called Luminous Compact Blue Galaxies (LCBGs)

Galaxies in which star formation and associated phenomena dominate the total energetics are known as starburst galaxies (Weedman, 1983). These objects have a large SFR per unit area compared to normal galaxies, and the time it would take to produce the current stellar mass at the current star formation rate is much less than the age of the Universe. These equivalent definitions (Kennicutt, 1998) cover galaxies with a wide variety of properties at different redshifts. Distant Lyman-break galaxies (Steidel et al., 1996; Lowenthal et al., 1997), and LCBGs (Werk et al., 2004) fall under this category. This denotes their cosmological relevance and turns local starburst galaxies into unique laboratories to study the complex ecosystem of the star formation process throughout time when they can be properly and equally selected at different epochs of the Universe.

The launch of the Hubble Space Telescope (HST), and the advent of the 10-m class telescopes resulted in the tipping point for distant LCBG detailed information regarding their morphologies, kinematics, SFRs, and masses. Most of what we know today specifically about LCBGs at $z \sim 1$ we have learned in the last decade. Keck Observatory observations showed that their integrated emission line velocity width are

typically smaller than $\sim$100 km s^{-1} (Koo et al., 1995; Guzmán et al., 1996; Phillips et al., 1997). On the other hand, HST observations showed their complex and knotted structure, and that their typical half-light radii are $r_{1/2} < 5$ kpc (Phillips et al., 1997; Guzmán et al., 1998; Noeske et al., 2006). LCBGs, although intrinsically luminous ($L \sim 0.2$–$5.0\ L^{\star}$), have low mass-to-light ratios ($M/L \sim 0.1$–$1.0\ M_{\odot}{L_{\odot}}^{-1}$), smaller than a typical nearby $L^{\star}$ galaxy (Guzmán et al., 1997). LCBGs are undergoing vigorous episodes of star formation that involve up to $\sim$10% of their total mass (Koo et al., 1994; Guzmán et al., 1996, 1997, 1998; Phillips et al., 1997; Hammer et al., 2001; Noeske et al., 2006; Puech et al., 2006; Rawat et al., 2007). Furthermore, while morphologically and spectroscopically heterogeneous, Phillips et al. (1997) and Guzmán et al. (1998) were able to divide them into two categories: (i) "SBN-like," featuring a nuclear starburst and a spiral disk morphology; and "HII-like," featuring a high resemblance to giant HII regions and an irregular morphology. And last, but not least, the typical stellar mass of LCBGs ranges from $\sim 5 \times 10^9\ M_{\odot}$ to $\sim 10^{11}\ M_{\odot}$ (Guzmán et al., 2003), which places this galaxy population approximately right at the location of the critical mass value observed in the "blue cloud," ultimately turning them into the key population to study in order to understand the nature of the color bi-modality of galaxies.

Recent progress suggest that LCBGs may arguably hold the key to study the two main physical mechanisms that rule galaxy formation and evolution since $z \sim 1.5$ (i.e., merging and quenching). In particular, LCBGs may provide the answer to three fundamental questions:

i What is the mechanism responsible for triggering the burst of star formation?

ii What is the mechanism responsible for quenching the burst of star formation and limiting the stellar mass?

iii What can the study of the local population of LCBGs tell us about the distant population of LCBGs?

These three questions are the foundations of this dissertation and are introduced below. To answer them, this dissertation focuses on the optical kinematic properties of local LCBGs and what we can learn from the investigation of ionized gas velocity and velocity width maps, kinematic signatures of minor or major mergers, AGN and SN-driven galactic wind feedback, dynamical masses, etc. Different complementary approaches are being lead by members of an international collaboration, whose aim is to disentangle the mysteries of LCBGs by means of a multi-wavelength study.

1.2 Luminous Compact Blue Galaxies in the Local Universe

Recent technological advances both in ground- and space-based observatories put us on the verge of a major take off regarding the study of distant LCBGs. Several surveys have already started a detailed study of the distant population of LCBGs (e.g., Yang et al., 2008; Epinat et al., 2009; Förster Schreiber et al., 2009). Nevertheless, we need to be very careful with the intrinsic limitations of these surveys when discussing their results, as shown in Chapters 3 and 4. Alternatively, we focus on a comprehensive multi-wavelength study of a sample of nearby, young, blue, active, late-type galaxies that best resemble the properties of the distant population of LCBGs. Our sample can be used as the necessary reference for interpreting and understanding the nature of the distant population of LCBGs. This dissertation is one of the cornerstones of this multi-wavelength study.

The optical range is the best understood in nearby galaxies, and will be systematically studied in distant galaxies with the forthcoming new generation of instruments on 10-m class telescopes. On top of that, three dimensional (3D) optical spectroscopy data provide a complete description of the physical properties of galaxies as a function of spatial position within the galaxy, which allows for a proper analysis of the physical processes responsible for the formation and evolution of LCBGs. Furthermore, kinematic properties themselves are able to shed some light into the questions stated above and addressed next. The 3D optical kinematic study of a sample of 22 local LCBGs –our representative

sample– is the main focus of this dissertation, and is designed to shed light into three fundamental questions about the nature, formation, and evolution of LCBGs.

1.2.1 What Is the Mechanism Responsible for Triggering the Burst of Star Formation?

Answering this question would primarily allow us to understand why the cosmic SFR is seen to increase at $z \sim 1$. LCBGs are vigorous star-forming galaxies with high SFRs per unit mass, which are undergoing a vigorous episode of star formation that involve up to ∼10% of the total mass of the galaxy (Koo et al., 1994; Guzmán et al., 1996, 1997, 1998; Phillips et al., 1997; Gil de Paz et al., 2000; Hammer et al., 2001; Noeske et al., 2006; Puech et al., 2006; Rawat et al., 2007), and contribute the most to the cosmic SFR increase in the last ∼9 Gyr. Such episodes may be caused by both major and minor mergers, and the efficient transformation of accreted cool gas into stars. For answering this question neutral atomic, ionized, and molecular gas content and kinematic estimates are necessary. Morphological information and accurate SFR estimates may help as well to fully isolate the triggering mechanism in LCBGs.

UV-continuum images, and [OII]λ3727 and Hα optical emission line flux maps can trace star formation in LCBGs as a function of spatial position within the galaxy. In particular, the Hα optical emission line flux maps of the LCBGs in our representative sample show that star formation takes place in multiple giant HII regions throughout the galaxy. The SFR of these regions range between ∼0.1–10 $M_{\odot}$ yr^{-1} (Castillo-Morales, Gallego, Pérez-Gallego, et al., 2009a,b). On the other hand, near- and far-UV color images show red halos, which show that star formation takes place out to the low surface brightness outskirts of the galaxy. Accurate estimates of the SFRs in LCBGs are essential to investigate the triggering mechanisms in this galaxy population.

While major mergers are known to trigger intense star formation and evolve into spheroidal-like remnants (Mihos & Hernquist, 1994, 1996), most LCBGs show disk-like morphologies ranging from "SBN-" spiral-like galaxies to "HII -" irregular-like galaxies

(Guzmán et al., 1997, 1998). Therefore, from a morphological point of view, major mergers, responsible for spheroidal-like morphologies, are not favored as the main triggering mechanism in these galaxies. On the other hand, minor mergers are a plausible triggering mechanism for the current bursts of star formation in LCBGs. Minor merger models account for enhanced SFRs, and peculiar photometric features (Smith et al., 1996). The study of optical emission line velocity maps has the potential to discriminate between the nature of these mergers, as shown in Chapters 3 and 4. Furthermore, merger signatures can also be seen in HI maps (Garland et al., 2007).

Results, previous and current, show that while about 50% of local LCBGs are not isolated and have close optical or radio companions (some gas-rich companions are only revealed by means of HI observations; Garland et al., 2004; Pisano, Garland, Pérez-Gallego, et al., 2009a), only $\leq$30% of field galaxies have them (James et al., 2008; Pisano et al., 2002). Nevertheless, LCBGs from the Sloan Digital Sky Survey (SDSS), with and without companions, show no difference in luminosity, color, size, emission line width, HI mass, total mass, or SFR. The possibility of a correlation between the kinematic signatures of recent interactions in LCBGs and their environment is discussed in Chapter 3. Such a correlation would imply that these interactions are responsible for triggering the enhanced star formation in LCBGs.

Kinematic signatures of recent interactions should be easy to identify in optical and HI velocity and velocity width maps, as shown in Chapters 3 and 4. In particular, both major and minor mergers show deviations from smooth rotations, and the quality of our data allow us to look for those. As an example, Homeier & Gallagher (1999) discussed whether a minor or a major merger in NGC 7673, one of the galaxies studied in depth in Chapter 4, was responsible for triggering the enhanced star formation in this particular galaxy. In general, from a kinematic point of view, minor mergers are easier to identify when they affect an overall rotating system. An alternative option is that the presence of bars driving gas to the center of the galaxy (e.g., Jogee et al., 2005) is responsible for

the enhanced star formation in LCBGs. Nevertheless, we do not see evidence for bars in almost any of the LCBGs investigated.

1.2.2 What Is the Mechanism Responsible for Quenching the Star Formation and Limiting the Stellar Mass?

Both the existence of an upper stellar mass limit in the "blue cloud" (i.e., $M_\star \sim 3 \times 10^{10}\ M_\odot$), and the stellar mass range of LCBGs (i.e., from $\sim 5 \times 10^9$ to $\sim 10^{11}\ M_\odot$) have been highlighted above. Their typical stellar masses, place LCBGs at the location of this upper limit. Before evolving into the "red sequence," star formation in galaxies from the "blue cloud" is quenched, limiting that way further stellar mass growth. Therefore, their stellar masses turn LCBGs into unique laboratories to investigate why the star formation and the stellar mass growth stop in blue galaxies.

Triggering mechanisms include massive halos, AGNs, and SN-driven galactic winds. Halo mass measurements are needed to study the effects of massive halos, while both flux and kinematic signatures, as shown in Chapter 3, are needed to study the presence of AGNs and SN-driven galactic winds in these galaxies.

We have already mentioned before that the existence of a maximal halo mass (i.e., $M_{halo} \sim 10^{12}\ M_\odot$) might be responsible for the star formation quenching (Cattaneo et al., 2006). This maximal halo mass arises from shock heating of accreting gas above this mass. Since this gas is needed to keep the star formation activity going, when its temperature increases and the accretion ceases, so does the star formation. In order to study this scenario, accurate halo mass estimates are needed.

Halo mass estimates can be inferred from HI dynamical masses. Instead of ionized gas, neutral atomic gas is used because it traces the gravitational potential to larger radii. Typical HI dynamical mass estimates of LCBGs are below $10^{12}\ M_\odot$ as shown by (Pisano, Garland, Pérez-Gallego, et al., 2009a), who also find a few outliers with HI dynamical mass estimates up to $\sim 10^{13}\ M_\odot$. In addition, by comparing resolved HI dynamical

masses with dynamical masses derived from our optical analysis, we can infer the actual dynamical masses of distant LCBGs, where we can measure neutral atomic gas fluxes.

Other quenching mechanisms include AGNs and SN-driven galactic winds (Mihos & Hernquist, 1994, 1996; Sanders & Mirabel, 1996; Murray et al., 2005; Granato et al., 2004; Springel et al., 2005; Hopkins et al., 2006). While the presence of quasars can be ruled out, we cannot discard the presence of AGNs in LCBGs, after investigating the SDSS spectra of these galaxies. In particular, 3D optical spectroscopy has the potential of revealing the presence of low-level AGN by means of unusually high line ratios [OIII]/Hβ and [NII]/Hα (Brinchmann et al., 2004), and spectrally resolved kinematic components, as shown in Chapter 3. The extent and strength of these kinematical subcomponents allows us to quantify the outflow/inflow of gas from/onto galaxies (Marlowe et al., 1995). It is important to notice that we can derive these properties as a function of position within the galaxy, and that our observational technique, explained in depth in Chapter 2, allows us to fully resolve each of the objects in our representative sample down to a spatial resolution of 1 arcsec. At the average redshift of our sample 1 arcsec translates into less than 400 pc across.

1.2.3 What Can the Study of the Local Population of LCBGs Tell Us About the Distant Population of LCBGs?

Nearby LCBGs can be used as a proxy for learning about the formation, nature, and evolution of distant LCBGs, including Lyman-break galaxies, and to simulate observations of those in order to help us properly interpret the results of current and forthcoming distant surveys, Furthermore, the study of the kinematics of nearby LCBGs can shed light on whether or not these objects are virialized. Knowing this is crucial for interpreting distant LCBG data, and avoiding wrong conclusions regarding, for example, their masses, and therefore, their evolution.

A multi-wavelength study of a representative sample of nearby LCBGs can be used as a reference for studies of distant young, blue, active, late-type galaxies, including

Lyman-break galaxies. This can be done because they share not only the observational properties used to define our selection criteria, but also physical properties intrinsically linked to their formation and evolution. Furthermore, distant LCBGs extend up to $z > 2$ nearby LCBG correlations, such as the one found by Melnick et al. (1987) involving their Hβ luminosities and their integrated velocity widths, which can be used as a distance indicator and is discussed in depth in Chapter 5. Such a reference is necessary in order to correctly interpret results coming from the analysis of data from distant surveys and compensate for any possible bias associated to the limitations of distant observations. But also, different properties can be inferred by understanding how different observational and physical properties of the nearby population relate to each other. An obvious example, we have already mentioned, is the possible relation between dynamical masses derived from the ionized gas in LCBGs and the HI which cannot be measured for distant LCBGs.

Current 3D spectroscopy surveys include Yang et al. (2008), Epinat et al. (2009), and Förster Schreiber et al. (2009). These studies use 3D spectrographs GIRAFFE (intermediate-redshift) and SINFONI (high-redshift with adaptive optics) at the Very Large Telescope of the European Southern Observatory. All together they cover a broad redshift range ($0.4 < z < 2.6$). They conclude that galaxy kinematics have rapidly evolved because of the high percentage of objects with complex kinematics that might be linked to the presence of mergers, versus the percentage found nearby (Le Fèvre et al., 2000). When interpreting these results one needs to be cautious because of their intrinsic limitations. Yang et al. (2008), for example, base their analysis on a sample of galaxies at $z \sim 0.6$, and a spatial sampling consisting in, on average, 12 micro-lenses with a spatial resolution of 0.52 arcsec (over 3 kpc at the average redshift of their sample). In Chapter 3 we show that relevant spatially and spectrally resolved kinematic components are found in these galaxies in smaller scales. This may have an important impact at the time of trying to classify these objects based on their kinematic properties.

Furthermore, as explained in Chapter 5, we can use 3D spectroscopy data of our representative sample of local LCBGs to simulate observations of distant analogs. By doing so, we can shed light into the limitations of the distant surveys, and compensate for any possible biases introduced by cosmological factors, low signal-to-noise ratios, and instrumental constraints, associated to observations of high-redshift galaxies.

The bulk of this dissertation is to be published in Pérez-Gallego et al. (2009a), Pérez-Gallego et al. (2009b), and Pérez-Gallego et al. (2009c). Pérez-Gallego et al. (2009a), already submitted, includes the discussion carried out in Section 4.2, while citetperez09b, about to be submitted, inlcudes Sections 4.3 to 4.5. Finally, Pérez-Gallego et al. (2009c), includes the discussion carried out in Chapter 4. This dissertation uses also material from Siegel, Guzmán, Pérez-Gallego, et al. (2005), Gruel, Guzmán, & Pérez-Gallego (2009), Castillo-Morales, Gallego, Pérez-Gallego, et al. (2009a), Castillo-Morales, Gallego, Pérez-Gallego, et al. (2009b), and Castillo-Morales, Gallego, Pérez-Gallego, et al. (2010), all studies I have actively been involved in.

Throughout this dissertation we adopt the concordance cosmology, i.e., a flat universe with $\Omega = 0.7$, $\Lambda = 0.3$, and $h = 0.7$, unless otherwise explicitly stated. This dissertation is structured as follows. In Chapter 2 we describe our sample selection, observations and data reduction. In Chapter 3 we show the statistical properties of our representative sample of 22 local LCBGs. An in depth analysis of four local LCBGs is discussed in Chapter 4. In Chapter 5 we state the connexion between local LCBGs and more distant populations. Conclusions are highlighted in Chapter 6.

CHAPTER 2
SAMPLE SELECTION, OBSERVATIONS, AND DATA REDUCTION

2.1 Sample Selection

The "blue cloud" is made up of galaxies which form a continuous distribution in luminosity, surface brightness, and color. In order to ensure the analogy between nearby and distant LCBGs seen in deep surveys we need to define an accurate observational selection criteria that allow us to select objects with the same optical observational properties up to $z \sim 2.5$. Our observational selection criteria selects objects with (i) absolute blue magnitude (M_B) brighter than -18.5; (ii) effective surface brightness (SB_e) brighter than 21 B-mag arcsec^{-2}; and (iii) $B - V$ color bluer than 0.6. These borders ensure the analogy between nearby LCBGs and those seen in wide-field Hubble Space Telescope imaging surveys. For extended objects with $SB_e(I_{AB}) = 24.5$ mag arcsec^{-2}, the typical limiting magnitude is $I_{AB} = 26$ mag (Scoville et al., 2007). At $z \sim 1$ these limits correspond to rest-frame $M_B^{Vega} \sim -18.5$ mag, and $SB_e(B)^{Vega} \sim 21$ mag arcsec^{-2}, respectively. Furthermore, LCBGs at $z \sim 1$ are characterized by having colors bluer than a typical spiral galaxy as seen nearby (Phillips et al., 1997).

The Sloan Digital Sky Survey (SDSS) is a major multi-filter imaging and spectroscopic redshift survey using a dedicated 2.5-m wide-angle optical telescope at Apache Point Observatory in New Mexico. The Data Release 4, released in 2005, is the fourth major SDSS data release and provides images, imaging catalogs, spectra, and redshifts for 180 million objects within an area equal to 6,670 square degrees. We have examined more than 560,000 galaxies with spectroscopic data over almost 5,000 square degrees on the sky in the DR4 of the SDSS (Adelman-McCarthy et al., 2006) and found ∼1,632 local ($D < 200$ Mpc) LCBGs which satisfy our criteria. LCBGs are a small subset of the total galaxy population in the local universe, as expected for the fastest evolving population since $z \sim 1$. Figure 2-1 illustrates how extreme and rare local LCBGs are as compared to the distribution of a representative sample of the galaxy population in the

local universe. As expected from our selection criteria, local LCBGs share the same region of the observational parameter space with their analogs at intermediate redshifts. Both $z \sim 1$ and $z \sim 0$ LCBGs are spectroscopically and morphologically diverse (Figures 2-2 and 2-3), and can be grouped into the same two broad categories: "SBN-like" and "HII -like" galaxies (Guzmán et al. 1997; Gil de Paz et al. 2000).

LCBGs near and far overlap in every parameter in which we can compare them. They have similar values of effective radii ($R_e \sim$ 1–4 kpc), Star Formation Rates (SFR $\sim$ 5-–20 $M_\odot$ yr^{-1}), metallicities ($Z \sim$ 0.3–0.7 $Z_\odot$), emission line velocity widths ($\sigma \sim$ 30-–100 km s^{-1}), dynamical and stellar masses ($\sim 10^9$–10^{11} $M_\odot$), and SFR per unit mass (Phillips et al., 1997; Guzmán et al., 1997; Gil de Paz et al., 2000). Preliminary results also show nearby LCBGs are preferentially found in over-dense regions in the sky, as are LCBGs at $z \sim 1$ (Capak et al., 2007; Castander, Guzmán, Pérez-Gallego, et al., 2009). As such, we believe that our sample of $z \sim 0$ LCBGs are the best analogs for inferring the properties of the distant population of LCBGs. Note that we will be applying the results of our study of local LCBGs to LCBGs at $z \sim 1$, not to higher mass galaxies such as grand-design spirals.

The SDSS LCBG sample at $D < 200$ Mpc will be used to study the statistical properties of local LCBGs as compared to the general galaxy population in the nearby universe. In particular, the analysis of the optical photometric and spectroscopic data in the SDSS, already in hand, will allow us to derive the number density of local LCBGs, their contribution to both luminosity function and the stellar mass function of local blue galaxies, and their clustering properties (Castander, Guzmán, Pérez-Gallego, et al., 2009). Far- and near-ultraviolet (UV) Galaxy Evolution Explorer (GALEX) data already exist for $\sim$200 local LCBGs allowing us to derive UV-based SFRs (Gil de Paz et al., 2007), and study their contribution to the cosmic SFR of local UV galaxies. In addition, we already have single-dish HI data on a total of 142 local LCBGs including original observations of 57 LCBGs using Arecibo and the Green Bank Telescope. The integrated flux of the HI

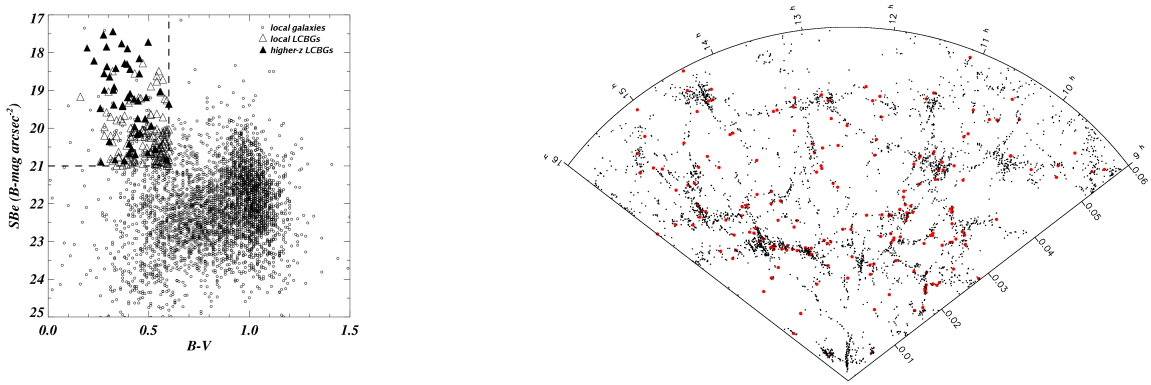

Figure 2-1. A) $B-V$ color versus average surface brightness (B-mag arcsec^{-2}) within R_e. Open circles show the properties of ∼4,000 galaxies in the local Universe from Prugniel & Maubon (2000); filled triangles show a representative sample of LCBGs at intermediate redshifts from Phillips et al. (1997); triangles represent a subset of SDSS-selected LCBGs in the local Universe. The dashed lines demark the color and surface brightness criteria used to select LCBGs. B) Wedge diagram of SDSS DR5 galaxies with $r \leq 16.5$ and available spectra up to redshift $z = 0.06$ (black dots). Galaxies are plotted in a declination range from 0° to 5°. The larger red dots represent local LCBGs in this range.

line allows us to derive the mass of atomic hydrogen in each galaxy, giving us an estimate of the total supply of fuel for future star formation. When combined with the SFR, this yields limits on the potential length of the current burst in each LCBG (Garland et al., 2004, 2005; Pisano, Garland, Pérez-Gallego, et al., 2009a).

The statistical analysis is needed to characterize the global properties of LCBGs compared to the general galaxy population in the local universe, and with similar statistical studies currently being carried out for LCBGs at higher redshifts. However, an understanding of the nature and evolution of local LCBGs ultimately requires detailed mapping of the physical properties at various wavelengths, including kinematics, metallicity, age, and SFR as a function of spatial position within each galaxy. Our goal is to build a complete data-set for these local LCBGs including far- and near-UV images using GALEX, optical 3D spectroscopy using PPAK at Calar Alto (CAHA), and HI mapping using the Very Large Array and the Giant Metrewave Radio Telescope. This

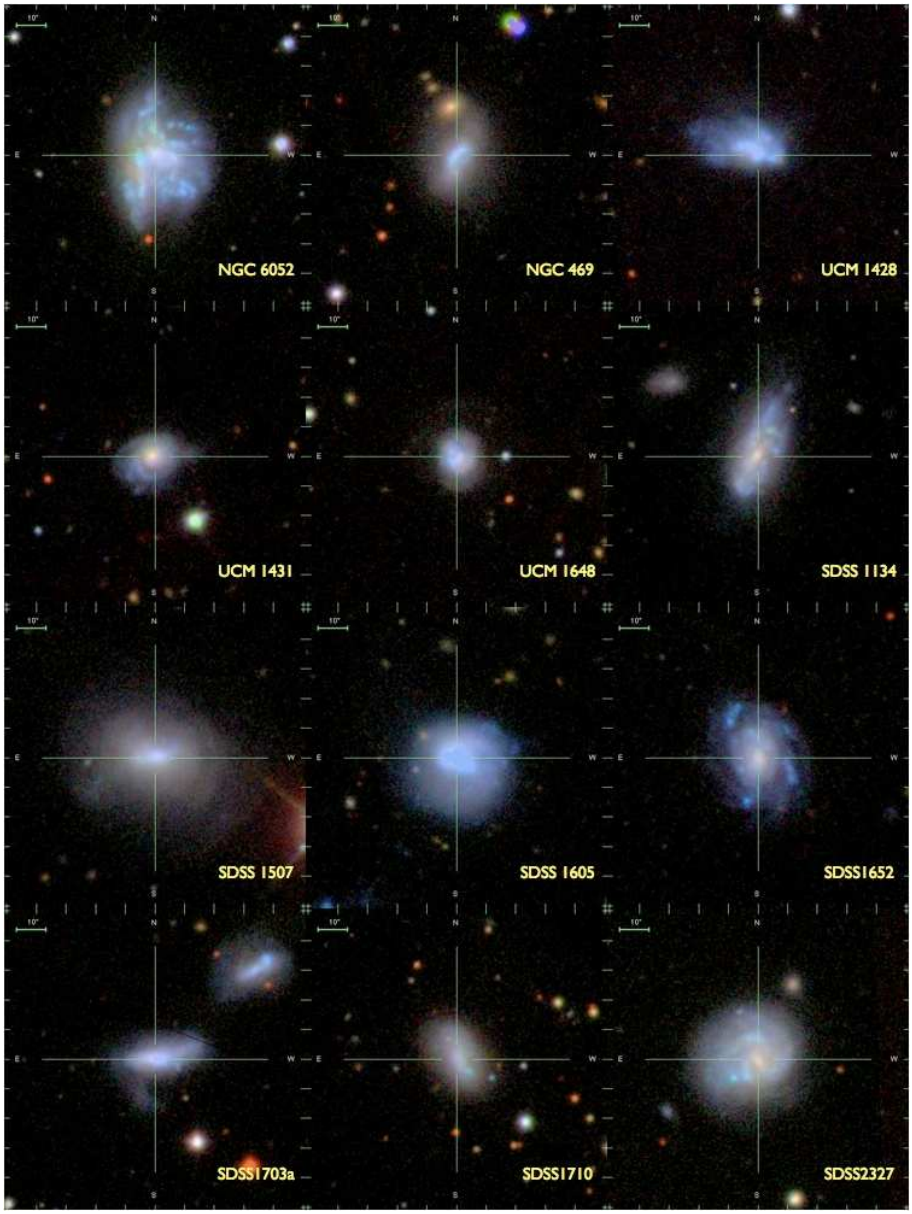

Figure 2-2. SDSS images of the 12 SDSS LCBGs.

unique data-set will provide a complete picture of the star formation history and mass assembly of local LCBGs.

We emphasize that while the color and surface brightness criteria imply that our sample belongs to the widely studied category of Blue Compact Dwarf galaxies (BCDs) (e.g., Kunth & Östlin, 2000, and references therein), LCBGs are a distinct class. BCDs are faint, with absolute magnitudes -18 mag $\leq M_B \leq -11$ mag, while LCBGs have

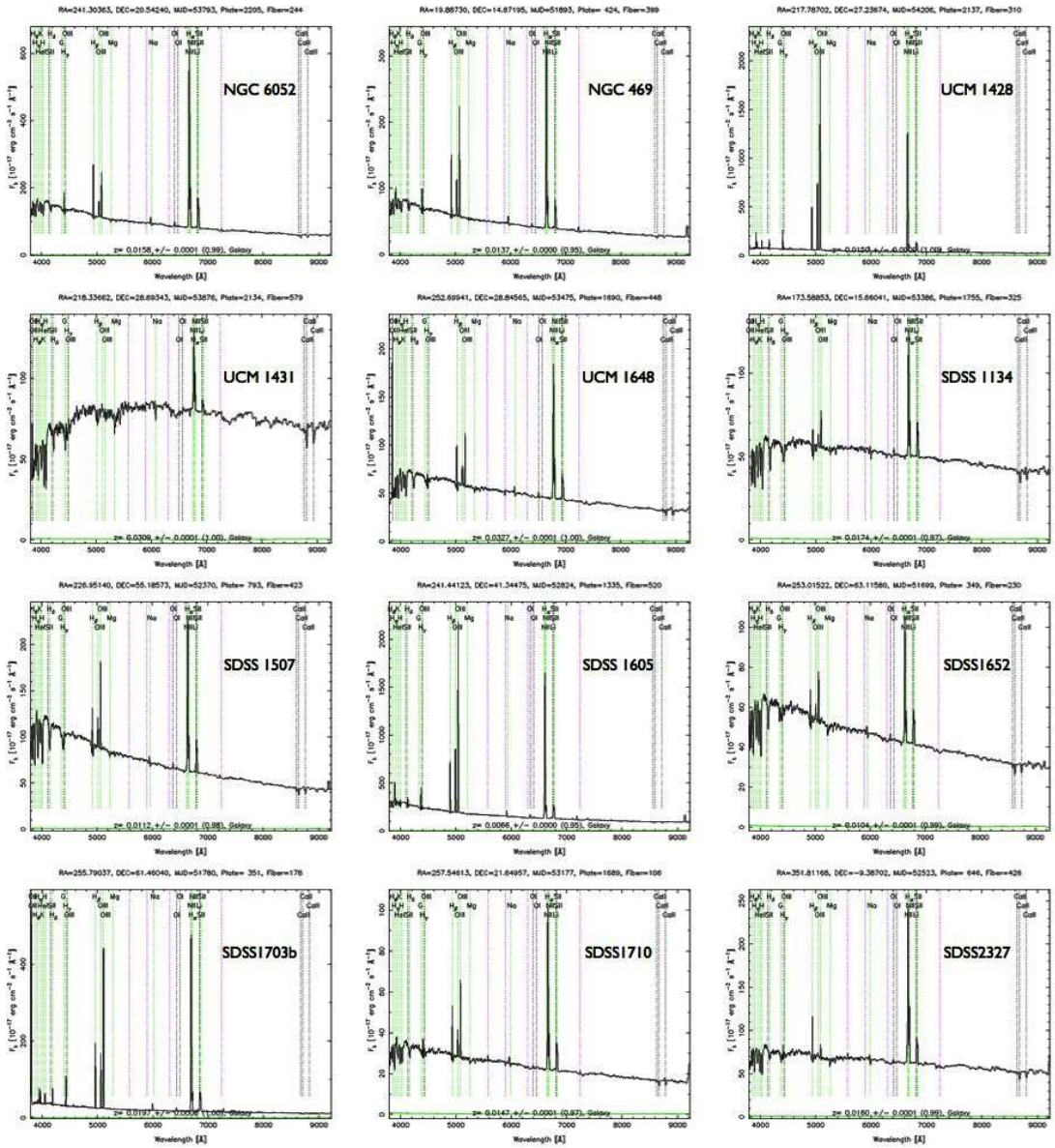

Figure 2-3. SDSS spectra of the 12 SDSS LCBGs.

luminosities $M_B \leq -18$ mag. The lower luminosities of BCDs imply they cannot be seen at intermediate redshifts in most wide-field, deep HST surveys, and thus are not counterparts to the observed population of distant LCBGs. Although a small number of $M_B \leq -18$ mag blue, compact galaxies have been studied in the last few years (e.g., Homeier & Gallagher, 1999; Östlin et al., 2001, 2004; Werk et al., 2004), our investigation

will be the first comprehensive, multi-wavelength study of a representative sample of local LCBGs.

The specific aim of this dissertation is the analysis of the 3D kinematic properties of a local representative sample of LCBGs. Out of the 1,632 LCBGs closer than 200 Mpc we selected 12 LCBGs from the DR4 of the SDSS. We also selected SDSS 1703b, which is the companion of LCBG SDSS 1703a, and whose observational properties are close enough to those of an LCBG to be considered as one (i.e., it satisfies the color criterion, and if the uncertainties of its observational properties are considered, it is within 1-σ of satisfying the other two selection criteria). We note here that a study of the accuracy of our selection criteria which deals, among other things, with the sharp borders used to classify LCBGs, is in progress (Castander, Guzmán, Pérez-Gallego, et al., 2009). Furthermore, we selected seven LCBGs from the Universidad Complutense de Madrid (UCM) survey catalog (Zamorano et al., 1994). We completed our sample with LCBG NGC 7714. We selected objects with a range of properties that best resemble the range of M_B, $SB_e(B)$, and $B-V$ shown by LCBGs in our vicinity. LCBGs with effective radii larger than 4 arcsec and closer than 100 Mpc were given priority to take full advantage of the field of view (FOV) and spatial resolution of the instrument used. Figure 2-4 shows how the observational properties of the objects in our representative sample compare to those of a sample of 320 LCBGs closer than 100 Mpc found the same way as our 1,632 LCBGs closer than 200 Mpc sample (notice that 18 out of the 22 LCBGs in our sample are closer than 100 Mpc). Furthermore, among the 12 LCBGs from the SDSS in our representative sample 25% are "SBN-like" (i.e., UCM 1431, SDSS 1134, and SDSS 1652) and 75% are "HII-like." Guzmán et al. (1997) found a similar percentage of both categories at $z \sim 0.4$ (54% "HII-like" and 46% "SBN-like"), and over a factor of two more "HII-like" galaxies at $z > 0.7$ (68% "HII-like" and 32% "SBN-like"). These percentages do not allow us to conclude anything about the evolution of each category. A thorough look at the statistical properties of our sample, whose properties are listed in Table 2-1, is the purpose of Chapter 3.

Table 2-1. Sample Properties[a]

Name	z[b]	d_a[c] (Mpc)	$M(B)$[c] (mag)	$m(b)$[c] (mag)	SB_e[c] (B-mag arcsec^{-2})	$B-V$[c] (mag)	R_e[c] (arcsec)	R_e[c] (kpc)
NGC 7673[e]	0.011368	48.0	-20.36	13.28	19.95	0.41	8.9	2.1
NGC 7714	0.009333	39.7	-20.10	13.00	20.00	0.40	14.3	2.7
NGC 6052[d]	0.015808	67.6	-20.69	13.37	19.71	0.41	7.6	2.4
NGC 469 [d]	0.013673	58.4	-19.13	14.74	20.05	0.42	4.7	1.3
UCM 0000	0.021960	91.6	-20.50	14.61	20.87	0.30	7.5	3.7
UCM 0156	0.013030	54.9	-18.84	15.33	20.77	0.49	5.3	1.6
UCM 1428[d]	0.014890	62.6	-19.08	14.78	20.36	0.24	5.2	1.7
UCM 1431[d]	0.031000	127.9	-19.99	15.76	20.70	0.52	4.4	2.7
UCM 1648[d]	0.032969	134.6	-20.32	15.69	20.32	0.26	3.9	2.4
UCM 2250	0.042149	171.6	-21.59	15.40	20.23	0.40	3.8	3.1
UCM 2258	0.021592	90.1	-19.36	15.79	20.84	0.21	4.4	2.0
UCM 2317	0.031962	131.7	-21.91	14.16	20.90	0.53	10.2	6.4
UCM 2327n	0.020600	86.0	-19.23	15.79	19.63	0.24	2.3	1.0
UCM 2327s	0.019130	80.0	-19.06	15.80	20.30	0.43	3.2	1.3
SDSS 1134	0.017335	71.7	-19.91	14.47	20.71	0.50	7.3	2.5
SDSS 1507	0.011231	46.8	-19.23	14.19	20.38	0.45	7.1	1.6
SDSS 1605	0.006640	27.8	-18.65	13.63	19.00	0.30	4.8	0.7
SDSS 1652	0.010376	43.3	-18.48	14.78	20.11	0.47	6.2	1.3
SDSS 1703a	0.019690	81.2	-19.62	14.74	19.68	0.36	4.0	1.6
SDSS 1703b	0.019760	81.5	-18.40	16.20	21.13	0.40	4.0	1.5
SDSS 1710	0.014757	61.2	-18.80	15.21	20.69	0.53	5.1	1.5
SDSS 2327	0.016044	66.5	-20.20	14.01	20.25	0.58	7.3	2.4
Mean[f]	0.0189	78	-19.70	14.76	20.30	0.40	6.0	2.16
Standard deviation[f]	±0.0019	±8	±0.20	±0.20	±0.11	±0.02	±0.6	±0.25

[a] Typical uncertainties for the properties listed are, according to the SDSS and UCM catalogs, ±0.000025 for z, ±0.1 Mpc for d_a, ±0.10 mag for $M(B)$, ±0.05 mag for $m(b)$, ±0.10 B-mag arcsec^{-2} for SB_e, ±0.07 dex for $B-V$, and ±0.3 arcsec and ±0.2 kpc for R_e.

[b] Nasa Extragalactic Database; [c] SDSS galaxies, NGC 6052, and NGC 469 properties from the SDSS catalog; UCM galaxies, and NGC 7673 properties from the UCM catalog; NGC 7714 from Garland et al. (2005)

[d] Also in the SDSS catalog; [e] Also in the UCM catalog; [f] Mean and standard deviation of the sample

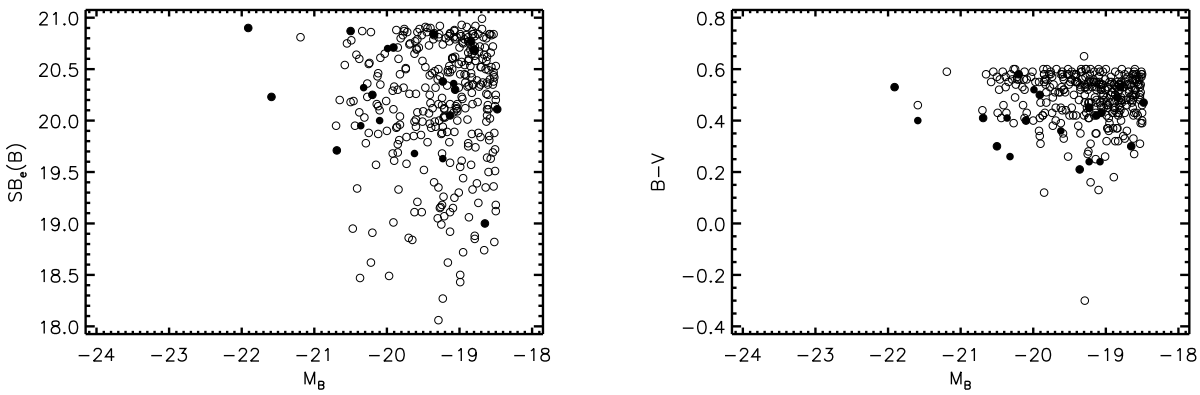

Figure 2-4. *Left:* M_B vs. $SB_e(B)$ for our sample of 21 LCBGs (filled circles; all but SDSS 1703b) and the sample of 320 LCBGs closer than 100 Mpc (open circles). *Right:* M_B vs. $B-V$ for our sample of 21 LCBGs (filled circles; all but SDSS 1703b) and the sample of 320 LCBGs closer than 100 Mpc (open circles)

2.2 Observations

Objects from our sample were observed with PPAK (Kelz et al., 2006) at the 3.5-m telescope in the Centro Astronómico Hispano Alemán[1] (CAHA). PPAK is an integral field unit (IFU) consisting of 331 science fibers with a diameter of 2.7 arcsec each, covering an hexagonal FOV of 74×65 arcsec^2. Furthermore, there are 15 calibration fibers, which are always illuminated by a ThAr lamp and used to align images on the ChargeCoupled Device (CCD) camera; and 36 sky fibers located 80 arcsec away from the center of the hexagonal FOV (Figure 2-5). The PPAK bundle has gaps between each fiber and its next neighbors. However, it is possible to fill these gaps by repeated observations of the same source with small pointing offsets. This is known as dithering.

PPAK observations of the 22 targets in our sample were made during three observing runs between 2005 and 2006 (Table 2-2). The first observing run (Run 47) took place

[1] Based on observations collected at the German-Spanish Astronomical Center, Calar Alto, jointly operated by the Max-Planck-Institut für Astronomie Heidelberg and the Instituto de Astrofísica de Andalucía (CSIC).

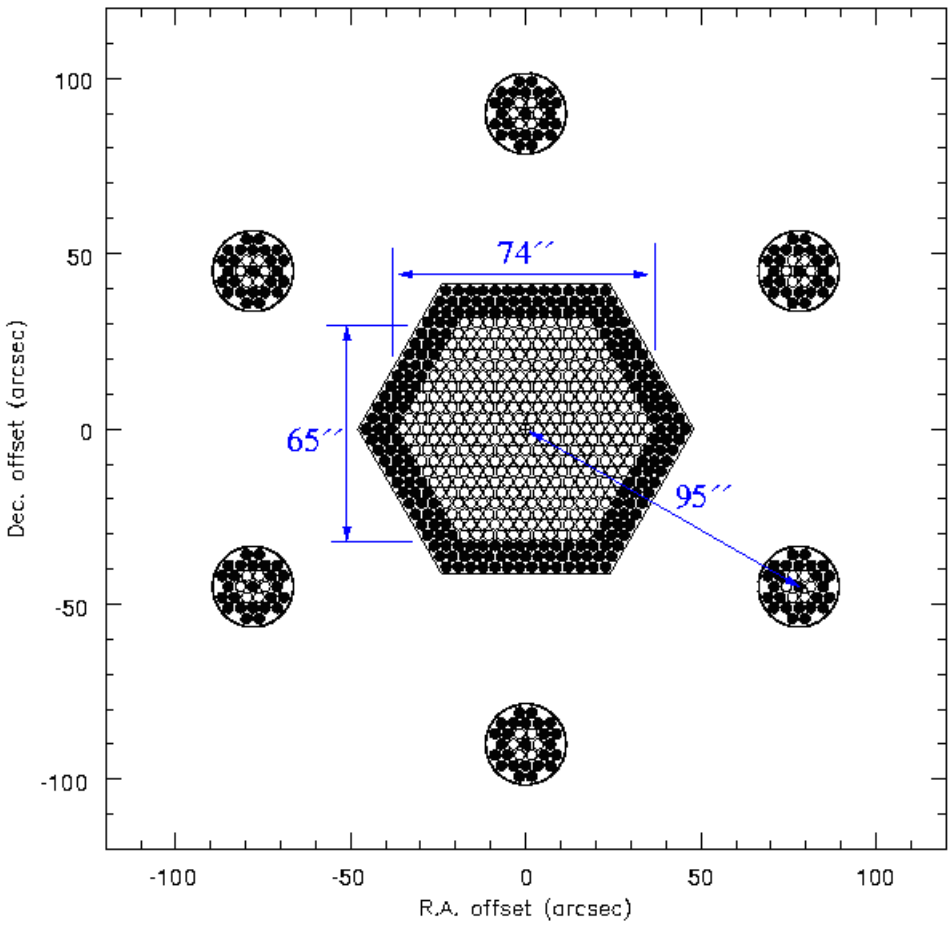

Figure 2-5. Geometrical layout and size of the central hexagonal IFU (331 fibers) and six surrounding sky fiber bundles (each consisting of 6 fibers). Only open plot symbols are optically active fibers, filled circles are indicating auxiliary fibers which were employed in the manufacturing process for mechanical reasons. Note that the PPAK fiber-bundle has gaps between each fiber and its next neighbors.

during the nights of August 8 to 14, 2005. The second observing run (Run 56) took place during the nights of April 17 to 23, 2006. Finally, the third observing run (Run 64) took place during the nights of July 28 to August 3, 2006.

Two different configurations were used (Table 2-3). First, a 300 lines mm^{-1} grating (V300) centered at 5316 Å was used. This low resolution configuration provided a spectral resolution of 10.7 Å FWHM ($\sigma \sim 255$ km s^{-1} at 5316 Å) covering the spectral range from

3600 to 7000 Å, including Hβ and Hα. Three different dithering positions (i.e., d1, d2, and d3) were observed to fill the gaps between each fiber and its next neighbors. Three exposures 330 s long were taken for a total exposure time of 990 s per dithering position. The offsets applied between the three different dithering positions allowed us to fully cover the FOV of the galaxy and overcome the presence of holes between fibers in the detector.

Second, a 1200 lines mm^{-1} grating (V1200) centered at 5040 Å was used. This high resolution configuration provided a nominal spectral resolution of 2.78 Å FWHM ($\sigma \sim 70$ km s^{-1} at 5040 Å), covering the spectral range from 4669 to 5400 Å, including Hβ and [OIII]λ5007. Three different dithering positions were observed during the first two runs. During the last run offsets were not applied between dithering positions. Three exposures, each one 900 s long, were taken for a total exposure time of 2700 s per dithering position during the first run. During the last two runs each exposure was 1200 s long for a total exposure time of 3600 s per dithering position. These changes were implemented in order to improve the signal to noise ratio (S/N) in the continuum of the LCBGs in our sample in order to study their underlying older stellar populations. Nevertheless, such a study is out of the scope of this dissertation.

2.3 Data Reduction

The raw data of fiber-fed spectrographs consist of a collection of spectra distributed along a certain axis of a two dimensional frame of a CCD. Figure 2-6 shows an example of integral field spectroscopy (IFS) corresponding to PPAK, illustrating this distribution. Each of the 382 spectra is dispersed along the x-axis. For each wavelength, each of the 382 spectra (i.e., science, sky, and calibration spectra) is also spread along the y-axis following a characteristic profile of finite width (Figure 2-6).

Table 2-2. Observing Log

Name	RA	DEC	V300[a]	V1200[a]	Notes
NGC 7673	23h27m41.0s	+23d35m20s	08.10.05	08.11.05	...
NGC 7714	23h36m14.1s	+02d09m19s	08.10&14.05	08.11&12.05	V1200: d1 in different nights
NGC 6052	16h05m12.9s	+20d32m32s	08.09&14.05	08.11&12.05	V1200: d12 two exposures
NGC 469	01h19m32.9s	+14d52m19s	08.14.05	08.12&13.05	V1200: d3 in different nights
UCM 0000	00h03m09.6s	+21d57m37s	07.28.06	07.30.06 & 08.02.06	V1200: no offsets, no d3
UCM 0156	01h59m15.7s	+24d25m00s	08.14.05	08.13.05	V300: only d1; V1200: only d1
UCM 1428	14h31m08.9s	+27d14m12s	...	04.18.06	...
UCM 1431	14h33m20.7s	+28d41m36s	08.14.05	08.12&13.05	V1200: no d3
UCM 1648	16h50m47.9s	+28d50m45s	07.28.06	04.20.06	V1200: no d3
UCM 2250	22h52m34.7s	+24d43m50s	07.28.06	08.01.06 & 08.02.06	V1200: no d3
UCM 2258	23h01m07.1s	+19d36m33s	07.29.06	...	...
UCM 2317	23h20m05.7s	+24d13m16s	08.10.05	08.13.05	...
UCM 2327n	23h30m09.9s	+25d31m58s	08.14.05	07.31.06	...
UCM 2327s	23h30m09.9s	+25d31m58s	08.14.05	07.31.06	...
SDSS 1134	11h34m21.2s	+15d39m37s	...	04.20.06	...
SDSS 1507	15h07m48.4s	+55d11m08s	...	04.19.06	V1200: no d3
SDSS 1605	16h05m45.9s	+41d20m41s	08.14.05	08.03.06	V1200: no offsets
SDSS 1652	16h52m03.6s	+63d06m57s	...	08.02.06	V1200: no offsets
SDSS 1703a	17h03m14.9s	+61d27m04s	07.28.06	07.30.06	V1200: no offsets
SDSS 1703b	17h03m12.2s	+61d27m21s	07.29.06	07.31.06	V1200: no offsets
SDSS 1710	17h10m11.1s	+21d38m58s	07.29.06	08.12&13.05	...
SDSS 2327	23h27m14.8s	-09d23m13s	07.29.06	08.03.06	V1200: no offsets; d123 two exposures

[a] Run 47: 08.08.05 to 08.14.05; Run 56: 04.18.06 to 04.23.06; Run 64: 07.28.06 to 08.03.06

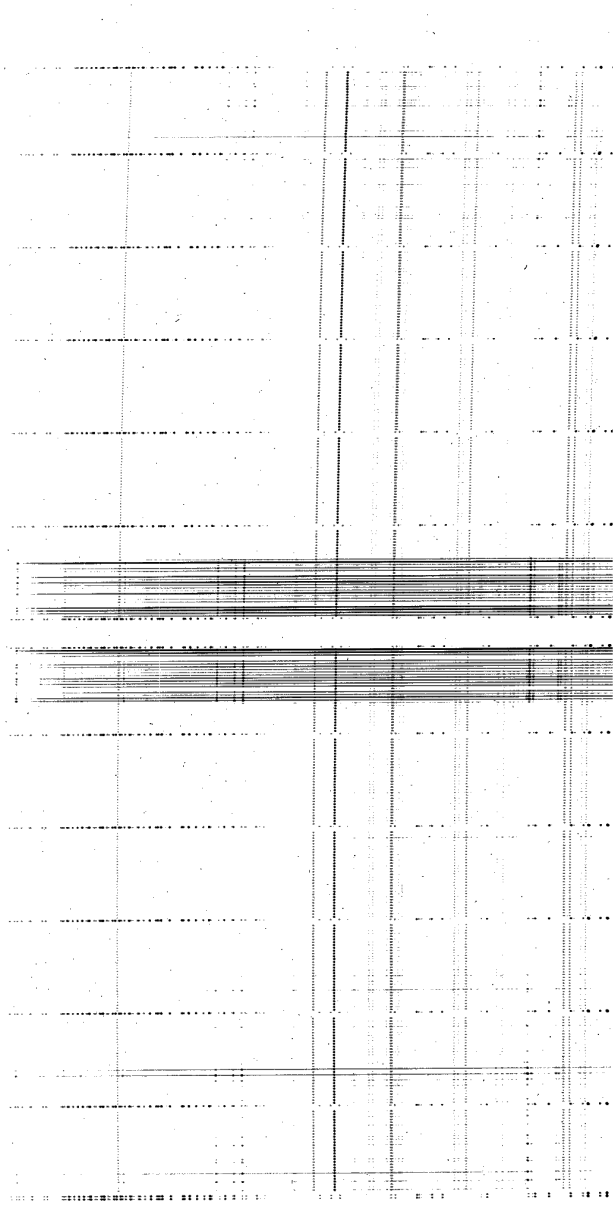

Figure 2-6. NGC 7673 IFS raw data covering the spectral range from 3600 to 7000 Å. This image includes 331 science spectra, 36 sky spectra, and 15 calibration spectra. The x-axis corresponds to the dispersion axis, while the y-axis corresponds to the spatial axis.

Table 2-3. Observational Strategy

Configuration	Run	Time per Dithering (s)	Offsets[a] (arcsec)
V300	Run 47	3 × 330	d2: (+1.56, +0.78); d3: (+1.56, -0.78)
V300	Run 56	3 × 330	d2: (+1.56, +0.78); d3: (+1.56, -0.78)
V300	Run 64	3 × 330	d2: (+1.56, +0.78); d3: (+1.56, -0.78)
V1200	Run 47	3 × 900	d2: (+1.56, +0.78); d3: (+1.56, -0.78)
V1200	Run 56	3 × 1200	d2: (+1.56, +0.78); d3: (+1.56, -0.78)
V1200	Run 64	3 × 1200	d2: (0.00, 0.00); d3: (0.00, 0.00)

[a] Offsets are with respect to d1: (0.00, 0.00)

The data were reduced using R3D and E3D (Sánchez, 2006), IRAF[2] , and our own custom software. All the images were bias-subtracted, flat-fielded, and cosmic-ray cleaned. The 331 science spectra per dithering position were then properly extracted, distortion-corrected, wavelength-calibrated, sky-subtracted, and flux-calibrated (Figure 2-7).

Bias-subtraction. Bias images were taken, averaged, and subtracted to correct images from a bias value which CCD cameras typically add to each image they record.

Flat-fielding. Flat-field images were taken to correct for the variation in sensitivity across the chip. They were obtained by illuminating the dome with a continuum lamp and therefore ensuring an homogeneous light source. Due to the instability of the chip, flat-field images were taken before every object, and calibration lamp exposure.

Cosmic-ray cleaning. By combining three different exposures per dithering we were able to remove cosmic rays from our images. This was done using a sigma clipping algorithm.

Extraction. The location of each spectrum was found on the detector for each pixel along the dispersion axis by considering a Gaussian profile in order to proceed to its extraction. Homogeneously illuminated flat-field images were used to find and trace the

[2] IRAF is distributed by the National Optical Astronomy Observatory, which is operated by the Association of Universities for Research in Astronomy (AURA) under cooperative agreement with the National Science Foundation.

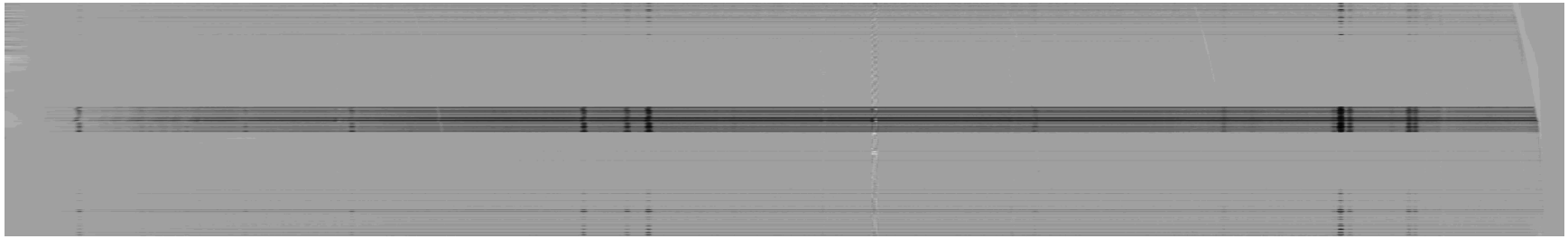

Figure 2-7. NGC 7673 IFS 331 reduced science spectra covering the spectral range from 3600 to 7000 Å. From left to right (i.e., dispersion axis), it is easy to identify the brightest lines as [OII]λ3727; Hβ and [OIII]$\lambda\lambda$4959,5007; [HeI]λ5876; Hα and [NII]$\lambda\lambda$6548,6584; and [SII]$\lambda\lambda$6717,6731. This is for one particular dithering position.

position of the spectra in the raw data. Cross-talk between fibers makes this step crucial. Nevertheless, we used an algorithm that minimizes the contamination due to this effect (Sánchez, 2006).

Distortion-correction. For grating spectrographs, the entrance slit is distorted and imaged as a curve onto the CCD. In order to correct our data from this effect, the intensity peak of a set of selected emission lines from our calibration lamp exposures is traced, and a distortion correction is determined to re-center all the lines to a common reference. These distortion corrections are subsequently applied to the science exposures. Nevertheless, we need first to align our calibration arc and science exposures by matching the intensity peaks of a set of selected ThAr emission lines from the 15 calibration fibers.

Wavelength-calibration. The wavelength coordinate system is determined by identifying the wavelengths of the arc emission lines.

The V300 wavelength calibration was performed using a He lamp with up to 17 lines within the considered spectral range. The rms of the best fit polynomial ($n = 3$) was 0.12 Å. A different arc was obtained every single night, nevertheless, these values were consistent up to the second significant figure. A further analysis to evaluate the accuracy of our calibration including sky lines reveals a final uncertainty in our calibration of 0.2 Å (10 km s^{-1} at 6000 Å). For this analysis, five high signal-to-noise (S/N) sky lines from the wavelength-calibrated spectra covering the entire V300 spectral range were fit by single Gaussian profiles for each fiber. The centroids of these lines were then compared to those of the CAHA sky atlas (Sánchez et al., 2007). The uncertainty of our measurements was given by the standard deviation of the resulting residuals, which was consistent within the entire V300 spectral range (i.e., for each sky line independently).

On the other hand, the V1200 wavelength calibration was performed using both He and Cs lamps because the He lamp lacked emission lines bluer than 5015 Å. During the first run, the Cs lamp was observed separately and both lamps were added to increase the spectral coverage. Furthermore, weak contamination lines from the ThAr lamp used

to illuminate the calibration fibers were also used for this purpose. Nevertheless, the *rms* of the best fit polynomial ($n = 3$) translated into an uncertainty of at least 0.25 Å (15 km s^{-1} at 5000 Å). The lack of sky lines in the V1200 spectral range did not allow us to carry on an analysis similar to the one carried out for the V300. While this is critical in the case we are interested in measuring the position of the centroid of the emission lines, it is not if we are only interested in measuring the velocity widths. Thus, our data can be wavelength-calibrated using the rest-frame positions of Hβ, [OIII]λ4959, and [OIII]λ5007, to measure velocity widths with the spectral resolution of the detector. For that, we wavelength-calibrated each of the fibers independently. When this is done, the *rms* for this particular spectral range is 0.13 Å (8 km s^{-1} at 5000 Å).

Nevertheless, a proper wavelength calibration was possible during the last two runs. It was performed using both He and Cs lamps simultaneously with up to 12 lines within the considered spectral range. Although observing both lines simultaneously improved our wavelength calibration, this was still far from what we would have expected due to the inappropriate set of arcs available. The *rms* of the best fit polynomial ($n = 3$) was 0.06 Å (4 km s^{-1} at 5000 Å). A different arc was obtained every single night, nevertheless these values were consistent up to the second significant figure. Again, a further analysis was not possible due to the lack of sky lines in the V1200 spectral range. Taking all this into account we decided to use the V1200 just for velocity widths measurements, even though velocity measurements were also made to check their consistency with the V300 ones.

Sky-subtraction. The 36 sky spectra provided by the 36 sky fibers located 80 arcsec away from the center of the hexagonal FOV were averaged and subtracted from the object spectra.

Flux-calibration. PPAK fiber-bundle does not cover the entire FOV because it has gaps between each fiber and its next neighbors. Nevertheless, our dithering technique allows us to cover the entire FOV with three offset telescope pointings. Therefore, it is possible to determine a relative calibration for each dithering using a standard star

observed with PPAK, and re-calibrate the calibrated spectra using broad-band photometry (Castillo-Morales, Gallego, Pérez-Gallego, et al., 2009a).

The data reduction process provided 331 fully reduced science spectra per dithering position and per galaxy. This is 2,979 spectra per galaxy, and 65,583 spectra in total. An example of these, with different values of the S/N is shown in Figure 2-8.

2.4 Basic Measurements

Emission lines were fit by single Gaussian profiles both in the V300 (Hα) and V1200 ([OIII]λ5007) configurations. A minimum S/N of 13 in the flux detection was required for the measurements to be considered. According to simulations we carried out, below this threshold, the uncertainty associated with a poor S/N dominates over the wavelength calibration uncertainty as the main source of error. These simulations were done by artificially added noise to an emission line with high S/N. By the time the S/N ratio dropped to 13 it was the poor S/N which dominated the uncertainty associated to the position of the centroid when the emission line was fit by a Gaussian profile. This cut-off corresponds to the uncertainty associated to the fit being twice as big as the uncertainty associated with the wavelength calibration.

As for the V1200 configuration, the presence of double emission line components was addressed by means of the calculation of the χ^2 of single and double Gaussian profile fits as given by

$$\chi^2 = \frac{1}{(N-M)} \sum_{i=1}^{N} \frac{(O_i - E_i)^2}{E_i} \ , \tag{2–1}$$

where O_i is the flux observed for a particular wavelength; E_i is the flux expected for a particular wavelength according to our fit; N is the number of data points used for the fit; and M is the number of variables we fit. These were four for single Gaussian profile fits (i.e., center, amplitude, width, and continuum), and six for double Gaussian profile fits since the width and the continuum of each line were forced to be the same. Nevertheless, this was not the case for UCM 0000, where the presence of a broader component, which is discussed in Chapter 3, was obvious. After carefully investigating our data we decided

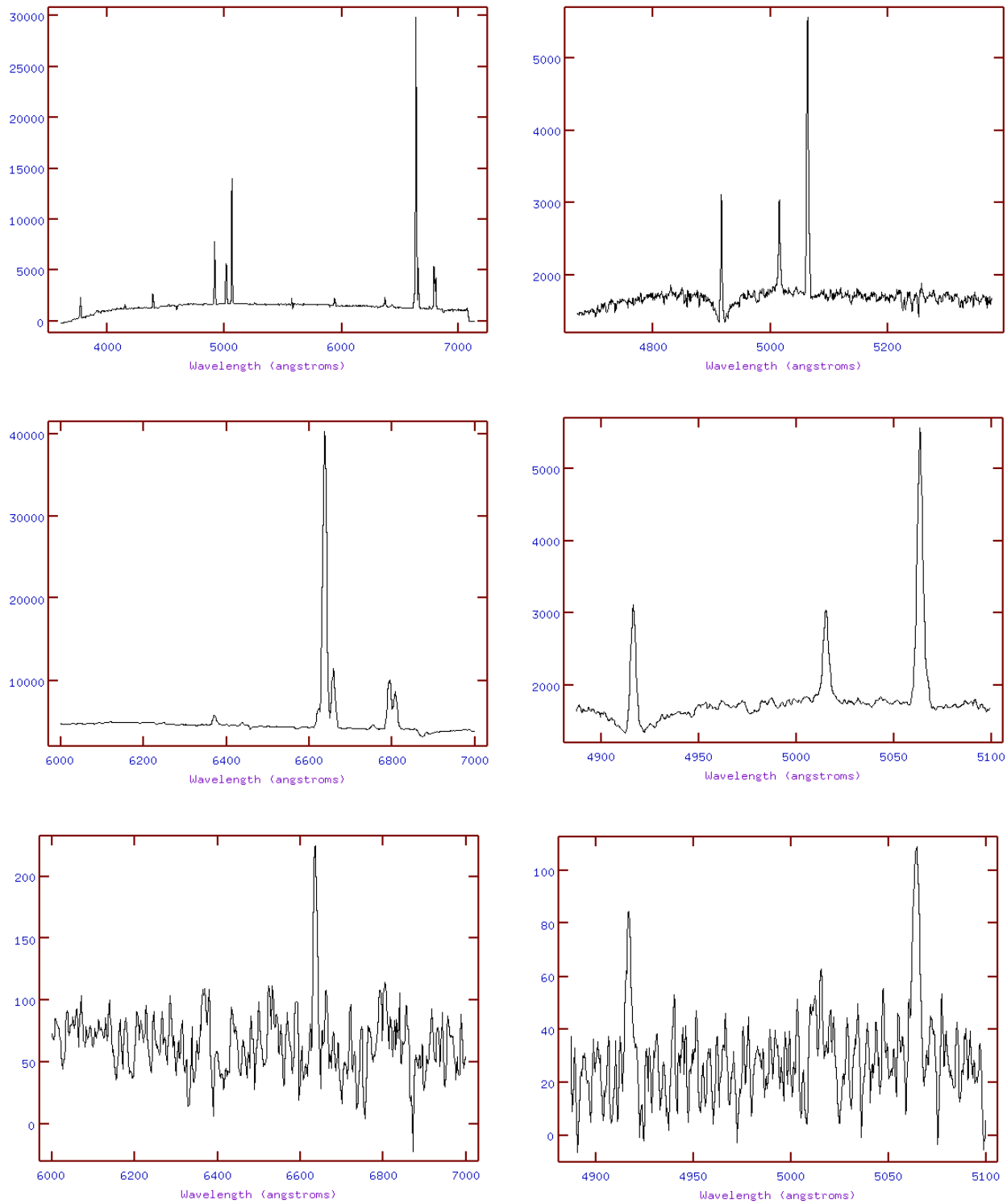

Figure 2-8. *Left:* From top to bottom, a V300 spectrum covering the the spectral range from 3600 to 7000 Å, a high S/N spectrum around Hα, and a low S/N spectrum around Hα. *Right:* From top to bottom, a V1200 spectrum covering the spectral range from 4900 to 5400 Å, a high S/N spectrum around Hβ, and a low S/N spectrum around Hβ. The y-axis scale is arbitrary.

to attempt a double Gaussian profile fit whenever the reduced χ^2 of our single Gaussian profile fit was $\gg$1 (Figure 2-9). In order to guarantee the reliability of the reduced χ^2 as an indicator of non-gaussianity and to avoid contamination, we demanded a minimum S/N of 30 for double Gaussian profile fits to be considered.

In the outer areas of the galaxy, we spatially binned the data by co-adding fibers to achieve a minimum S/N of 13. This way, we were able to obtain new measurements per dithering position. Furthermore, fibers from different dithering positions were also co-added to obtain new measurements. Each of these measurements were linked to the average position of the fibers co-added. These measurements made the final maps extend towards the lower surface brightness outskirts of the galaxy samplings. We recover an area about 10% larger per galaxy than before co-adding these fibers.

The velocity maps of the galaxies were derived from the Hα emission lines for each dithering position with the low resolution spectra. The data were interpolated down to a spatial resolution of 1 arcsec pixel^{-1} yielding a 60 $\times$ 60 pixel^2 square grid. Each of the original fibers (i.e., original spatial resolution element) was therefore sampled by approximately 3 $\times$ 3 pixel^2 (i.e., $\sim$ 2.7 $\times$ 2.7 arcsec^2). This kept us from oversampling the data, which may result in the appearance of artifacts (Sánchez, 2006). The three maps were then registered and averaged pixel by pixel. Thus, both the spatial resolution and the error associated with each measurement improved by a factor of $\sqrt{3}$ (6 km s^{-1} for the V300, and 2 and 5 km s^{-1} for the V1200 depending on the wavelength calibration carried out).

The velocity width maps of the galaxies were derived from the [OIII]λ5007 emission lines for each dithering position with the high resolution spectra. This line was selected as the one with highest S/N within the V1200 spectral range. The instrumental broadening ($\sigma_{instrument}$), as measured in sky lines for each fiber, was properly subtracted from the measured broadening ($\sigma_{measured}$) to find the intrinsic broadening of each measurement ($\sigma_{intrinsic}$) by means of $\sigma_{intrinsic} = \sqrt{\sigma^2_{measured} - \sigma^2_{instrument}}$. It is important to notice that

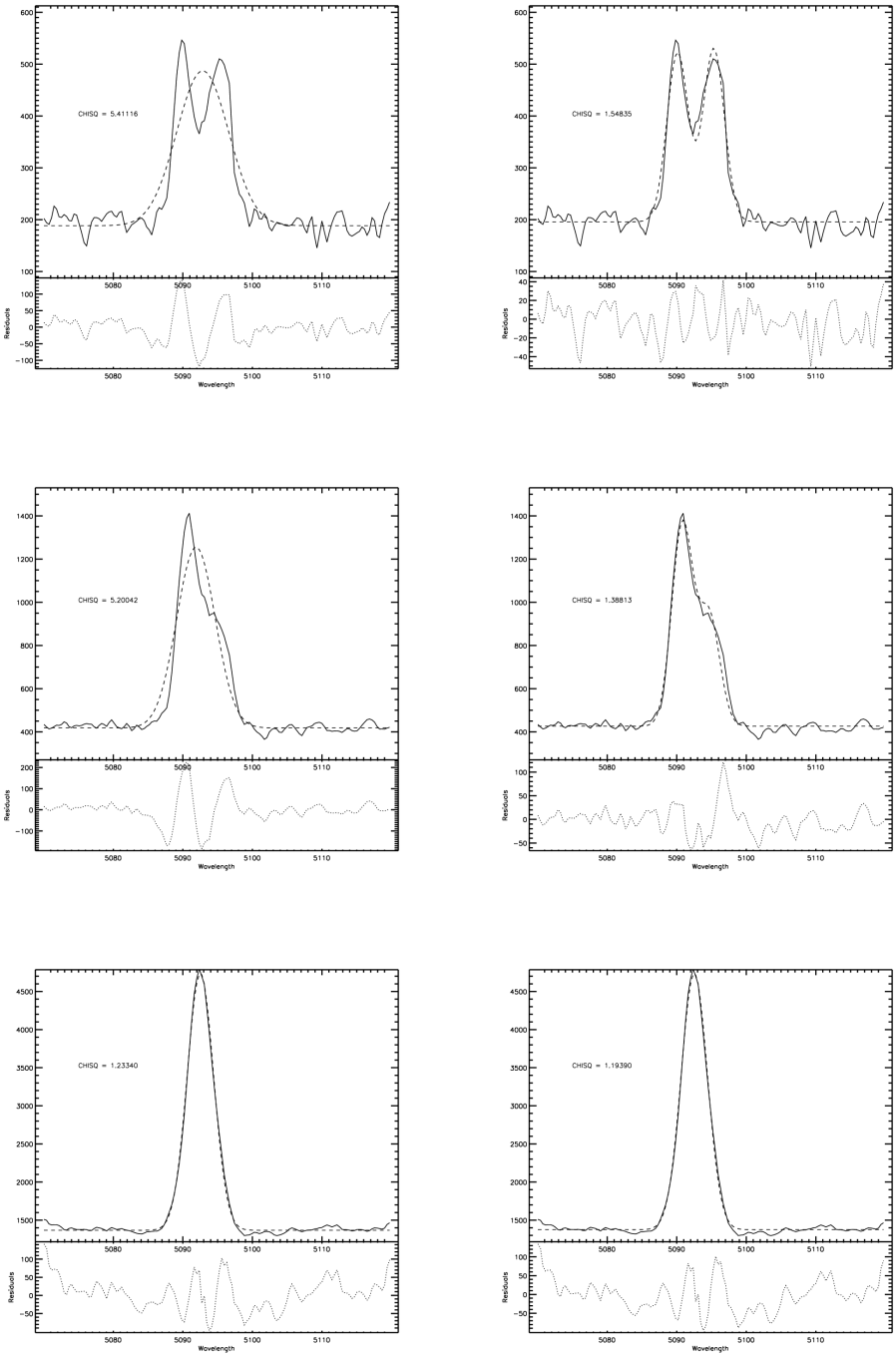

Figure 2-9. *Top row:* Example of two blended emission lines easy to identify. Single and double Gaussian profile fits are shown (dashed line). *Middle row:* Example of two blended emission lines. Single and double Gaussian profile fits are shown (dashed line). *Bottom row:* Two examples of single Gaussian profile fits (dashed line). The residuals and χ^2 are shown for all the fits. The flux scale is arbitrary.

the average measured instrumental broadening (2.3 Å FWHM) was considerably smaller than the nominal value listed on the instrument manual (2.78 Å FWHM). The final map was produced as explained above with the difference that no binning was pursued in this case since it would artificially broaden the emission lines. This translates, in general, into a smaller FOV. Nevertheless, the observational strategy for this particular configuration is different for different galaxies, which explains why this is not always the case (e.g., for UCM 2327 the FOV of the V1200 is bigger than for the V300, while for NGC 469 that is not the case). As for the velocity width uncertainties, a similar analysis as the one described for the S/N threshold show typical uncertainties of 10% for individual spectrum with low S/N (i.e., $\sim$13), and down to $\sim$2% for high S/N spectra, as, for example, those used for the measurements of the integrated velocity width of our galaxies, as shown in Chapter 3.

CHAPTER 3
ATLAS OF LOCAL LUMINOUS COMPACT BLUE GALAXIES

3.1 Statistical Properties

It is well established that Luminous Compact Blue Galaxies (LCBGs) at all redshifts are starburst galaxies that are undergoing a vigorous episode of star formation involving up to ∼10% of the total galaxy mass (Koo et al., 1994; Guzmán et al., 1996, 1997, 1998; Phillips et al., 1997; Gil de Paz et al., 2000; Hammer et al., 2001; Noeske et al., 2006; Puech et al., 2006; Rawat et al., 2007). Since LCBGs are a major contributor to the cosmic SFR at z 1 and scarce nearby, they may hold the key to understanding what caused the increase in the star formation activity of the universe observed ∼9 Gyrs ago.

While it is clear that major mergers between equal mass galaxies can trigger intense star formation in the remnants, such mergers also tend to produce spheroidal remnants (Mihos & Hernquist, 1994, 1996). Although some LCBGs have spheroidal-like, compact morphologies (Im et al., 2001; Ilbert et al., 2006; Zamojski et al., 2007), most exhibit disk morphologies ranging from small spiral galaxies ("SBN-like") to irregular galaxies ("HII-like"; Guzmán et al., 1997, 1998). This argues in favour of minor mergers over major mergers as a plausible cause for triggering the starbust. Such mergers would be evident in LCBGs through the resolved maps of their internal kinematics and from morphological features such as tidal tails.

Examples of why measuring the kinematics of distant galaxies precisely and robustly is mandatory for studying galaxy evolution are the rapid time decrease of cosmic SFR, the role of merging in the early evolution of galaxies, and the possible evolution of relations such as the Tully-Fisher relation (TFR). To identify the dynamical state of a galaxy requires the detailed knowledge of its kinematics on kiloparsec scales. Integral Field Spectroscopy (IFS) allows us to compute accurate total dynamical masses from both rotation curves and integrated velocity widths, and to trace the spatial distribution of stars and gas, as well as their kinematic contributions. Such spatially resolved kinematics

may help understanding the competing processes of cooling angular momentum exchange and loss, feedback from star formation, and Active Galactic Nuclei (AGN), which drive galaxy evolution.

Recent surveys aim to characterize the spatially resolved kinematics of distant (i.e., from $z \sim 0.4$ to $z \sim 2$) LCBGs by means of IFS using instruments such as GIRAFFE and SINFONI at the Very Large Telescope of the European Southern Observatory (e.g., Epinat et al., 2009; Puech et al., 2006; Förster Schreiber et al., 2006). These surveys may hold the key to understanding the processes that rule the formation and evolution of these galaxies.

In order to classify the kinematics of distant LCBGs Yang et al. (2008) distinguished between three different classes.

- **Rotating disks (RD).** The velocity map shows an ordered gradient, and the dynamical major axis is aligned with the morphological major axis. The velocity width map indicates a single peak close to the dynamic center.
- **Perturbed rotation (PR).** The kinematics show all the features of a RD, but the peak in the velocity width map is either absent or clearly shifted away from the dynamical center.
- **Complex kinematics (CK).** Neither the velocity map nor the velocity width map are compatible with regular disk rotation, including the velocity maps that are misaligned with the morphological major axis.

Yang et al. (2008) found for a sample of 63 galaxies 32% RDs, 25% PRs, and 43% CKs, which are limited by an error of 12%, confirming that at $0.4 < z < 0.75$, few massive emission line galaxies are kinematically relaxed. By means of a similar classification criteria, Förster Schreiber et al. (2009) found roughly one-third of a sample of 63 galaxies at $1.3 < z < 2.6$ to be rotation-dominated, one-third to be dispersion-dominated, and the remaining to be merger/interacting systems. Nevertheless, the apparent size of these objects make it difficult to fit their velocity and velocity width maps with models univocally, and it makes the study of the kinematic properties of local LCBGs necessary in order to properly interpret the kinematic properties of distant LCBGs.

Optical images from the SDSS or the Digitized Sky Survey (DSS), velocity maps, and velocity width maps for our sample are shown in Section 3.2. The main statistical properties of this sample are discussed below and listed in Tables 3-1 and 3-2.

For the sake of this analysis the galaxies UCM 2327n and UCM 2327s were considered as one galaxy (i.e., UCM 2327ns). This pair is about 0.2 Mpc away from each other and separated by less than about 10 arcsec, as seen in the field of view (FOV) of PPAK. Velocity width measurements for UCM 2258 were not possible since high spectral resolution data for this galaxy was not available. As stated in Chapter 2 we consider SDSS 1703b as an LCBG.

Table 3-1 lists an estimation of v_{rot} for galaxies in which this estimation was possible, and a measurement of the integrated velocity width as a result of adding up all the available spectra for each galaxy. We estimated for the latter an average uncertainty of $\pm 2\%$ as stated in Chapter 2 for high S/N Gaussian profile fits. Furthermore, the galaxy morphological type, and whether or not a known companion is present, are also listed. When the morphological type was not available in the literature a classification was performed by eye using the rest as a reference. We only consider companionship when previously published in the literature or when found in our 74×65 arcsec^2 FOV (i.e., 28×25 kpc^2 at the average redshift of our sample) with a redshift within the maximum and minimum velocities of the main target. Thus, different methods by means of which a companion can be found are considered.

An estimation of v_{rot} was performed only for those galaxies with a gradient in the velocity map, and a central peak in the velocity width map that could be interpreted as a kinematic center. This accounts for a total of ten galaxies. For those, galaxy rotation curves were drawn along their major axis as derived from the position of their kinematic centers, the geometry of their velocity contours, and their position angles (PAs). No modeling was attempted, and v_{rot} was estimated as half the distance between the red and blue velocity plateaus (Figures 3-2 and 3-3), which were fit by constant values. The

Table 3-1. Kinematics and Morphology

Name	$v_{rot}/\sin i$[a] (km s^{-1})	M_{dyn}[b] $10^9 M_\odot$	σ[c] (km s^{-1})	Type[d]	Companion[e]	Class
NGC 7673	43	0.90 ± 0.26	44	Sa	Yes	RD
NGC 7714	98	6.03 ± 0.75	75	Sb	Yes	RD
NGC 6052	212	25.1 ± 2.3	98	Sc	Yes	RD
NGC 469	...		42	S0	...	PR
UCM 0000	136	15.9 ± 1.4	192	Sa	...	RD
UCM 0156	...		57	Sb	...	PR
UCM 1428	...		64	Irr	...	CK
UCM 1431	132	10.9 ± 1.2	95	Sb	...	RD
UCM 1648	...		47	Sa	...	PR
UCM 2250	...		88	Sa	...	CK
UCM 2258	...		...	Sc	Yes	RD/PR
UCM 2317	144	30.9 ± 2.3	86	Sa	...	RD
UCM 2327ns	...		47	Sb & S0	Yes	CK
SDSS 1134	224	29.2 ± 2.6	193	Sa	Yes	RD
SDSS 1507	117	5.09 ± 0.77	38	Sd	...	RD
SDSS 1605	...		30	Irr	Yes	CK
SDSS 1652	...		50	Sc	...	PR
SDSS 1703a	...		67	Irr	Yes	CK
SDSS 1703b	...		31	Sd	Yes	PR
SDSS 1710	52	0.94 ± 0.22	58	Sd	...	RD
SDSS 2327	79	3.48 ± 0.53	46	Sc	...	RD
Averages[f]	124 ± 60	13 ± 11	72 ± 46	...	...	

[a] From our simple analysis, without considering inclination uncertainties, we estimated an average uncertainty of ± 7 km s^{-1} in v_{rot}

[b] $M_{dyn} = \frac{v_{rot}^2 R_e}{G}$

[c] As stated in Chapter 2, for high S/N Gaussian profile fits, the uncertainty is $\pm 2\%$ in σ

[c] Nasa Extragalactic Database: NGC Galaxies, SDSS 1134, and SDSS 1507; UCM Catalog: UCM Galaxies; the rest were classified by eye

[e] Nasa Extragalactic Database

[f] Mean and standard deviation of the sample

dynamical masses of the galaxies, $M_{dyn} = \frac{v_{rot}^2 R_e}{G}$, were estimated for the RDs in our sample from the value found for v_{rot} and the effective radii shown in Table 2-1. The masses of these objects vary between $\sim 1 \times 10^9$ and $\sim 3 \times 10^{10} M_\odot$, which coincides with the upper limit on the stellar mass of galaxies from the "blue cloud."

Furthermore, v_{rot} can be also estimated from the measurement of the velocity width by means of W_{20} ($W_{20} = 3.58\sigma$; $v_{rot} = 0.5 W_{20}/\sin i$), or, better, by means of W_R (Tully & Fouque, 1985), which accounts for random motions. This correction for random motions decreases the line width of the local LCBG by 26–38 km s^{-1}, depending on the rotational velocity (Garland et al., 2007). For spiral galaxies W_R is equal to twice v_{rot} (i.e., $\overline{(v_{rot} - 0.5W_R)/v_{rot}} \sim 0$ with $\sigma = 0.09$; Tully & Fouque, 1985). For our sub-sample of rotating LCBGs we find that while also in agreement, this is because the dispersion of the correlation is rather large (i.e. $\sigma = 0.55$). Such a dispersion may account for a factor up to $\sim$2 when estimating v_{rot} from velocity widths (with respect to the actual measurement), which translates into a factor up to $\sim$4 when estimating dynamical masses. This implies that the velocity widths of LCBGs, rather than accounting for the overall rotation of these galaxies, may significantly account as well for other kinematic components and, therefore, may not be as good of a dynamical mass estimator.

Figure 3-1 shows the TFR for these galaxies compared to a recent callibration by Tully & Pierce (2000). Our sample of local LCBGs tend to show larger M_B than the sample of spiral galaxies used for their calibration for a particular W_R. This suggests that, overall, for a particular rotation velocity, they are brighter. Therefore, their mass-to-light ratios are not in agreement with those found for spiral galaxies, they tend to be lower. Actually, by combining the dynamical masses shown in Table 3-1 and the absolute magnitudes shown in Table 2-1, we find an average value for M/L_B equal to 0.6. Such a lower value is in agreement with those found for late-type galaxies (Dickel & Rood, 1978).

Our observational strategy allowed us to sample the low surface brightness outskirts of these galaxies, and a careful look at the opposite extremes of our rotation curves shows

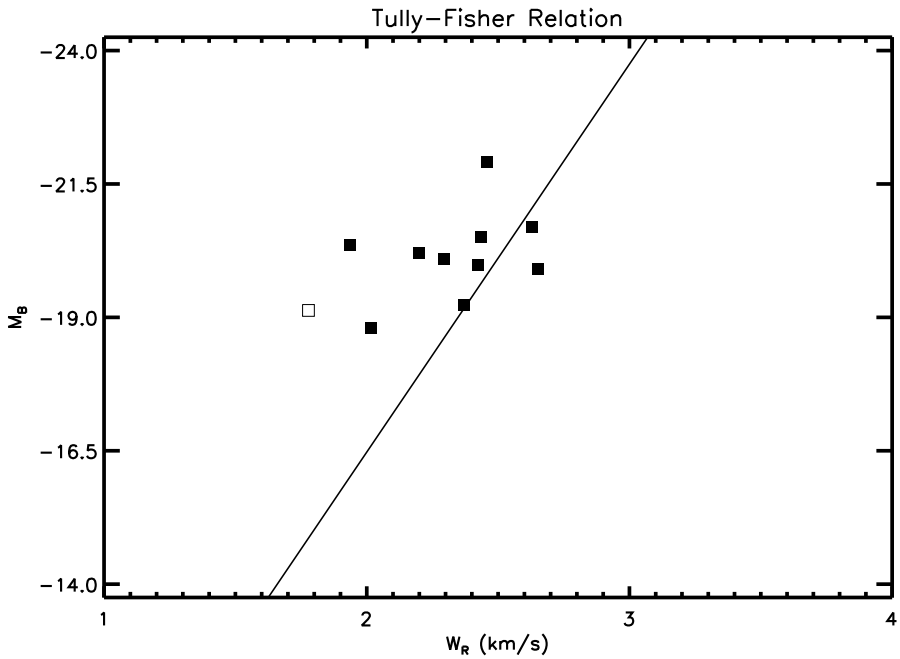

Figure 3-1. Tully-Fisher Relation for a subsample of 10 rotators among our sample of LCBGs (filled squares). NGC 469, which is not an RD, is also shown (open square) for a latter discussion (Chapter 4)

this. We investigated further the effect of this in our determination of v_{rot} by considering ± 1 data points for the fits of the plateaus and found it is only important for the red plateau of UCM 0000 as it can be seen in Figure 3-2. The average variance of these fits is ± 1 km s^{-1}. The uncertainty associated to a single velocity data point is ± 6 km s^{-1}. By considering a $\pm 10°$ variation in the estimated PAs we did not find important (less than 1%) effects in our determination of v_{rot}. From our simple analysis and plateau fits we estimated an average uncertainty of ± 7 km s^{-1} in our estimation of v_{rot} for each galaxy that does not take into consideration the effects of the uncertainties associated to the inclination of these galaxies.

To correct v_{rot} for the effects of inclination (i), we approximated each SDSS galaxy's inclination by

$$i = \arccos \frac{b}{a} \ , \tag{3–1}$$

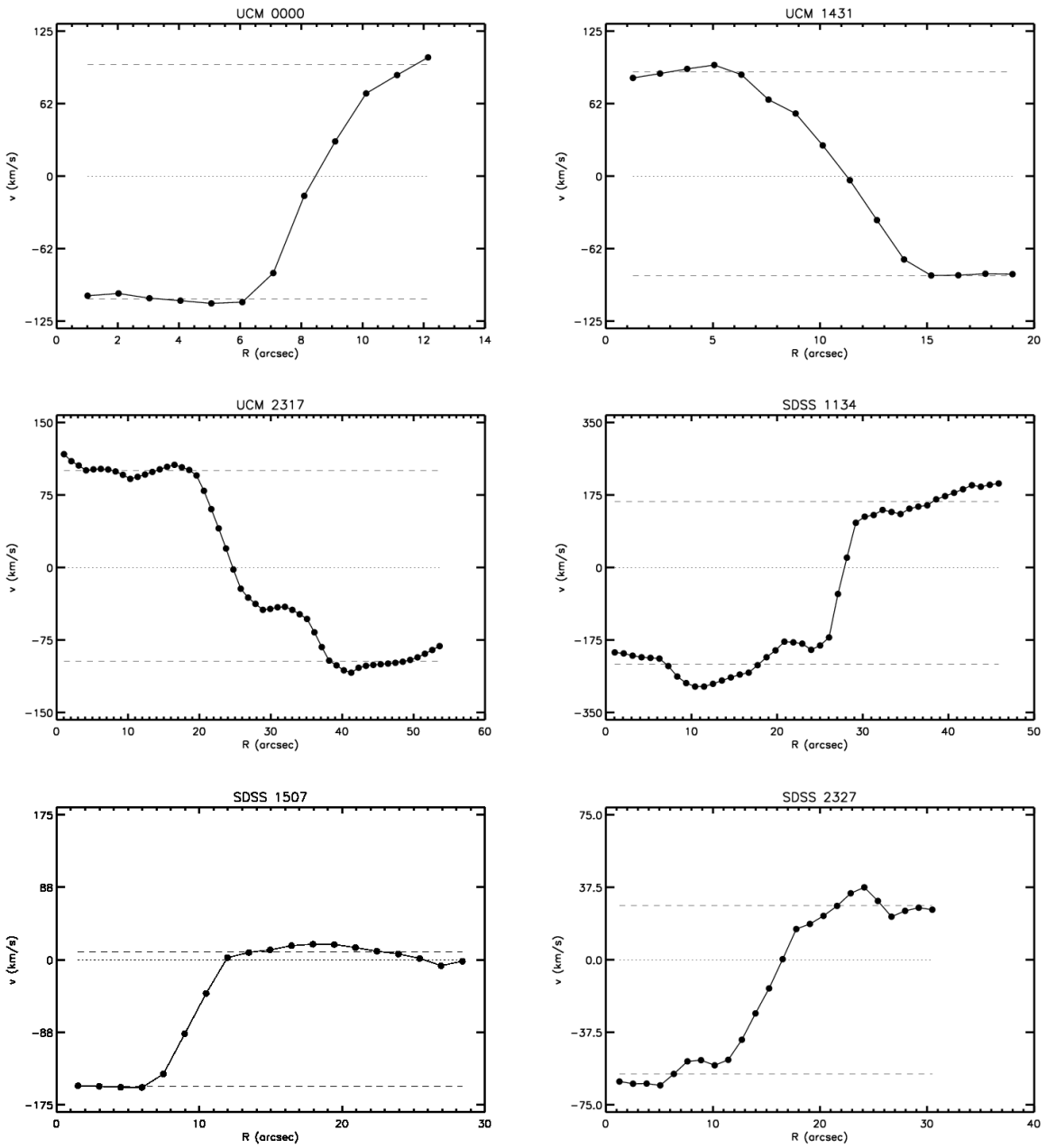

Figure 3-2. Rotation curves of UCM 0000, UCM 1431, UCM 2317, SDSS 1134, SDSS 1507, and SDSS 2327. For each LCBG, the dashed lines indicate the plateaus, while the dotted line indicates the velocity of the central velocity width peak, which is taken as a reference. The x-axis indicates the distance in arcsec from one extreme to the other of the major axis of the galaxy. The position of the central velocity width peak corresponds to the intersection of the rotation curve with the dotted line. The spatially resolved kinematic components of UCM 2317 were removed for this analysis.

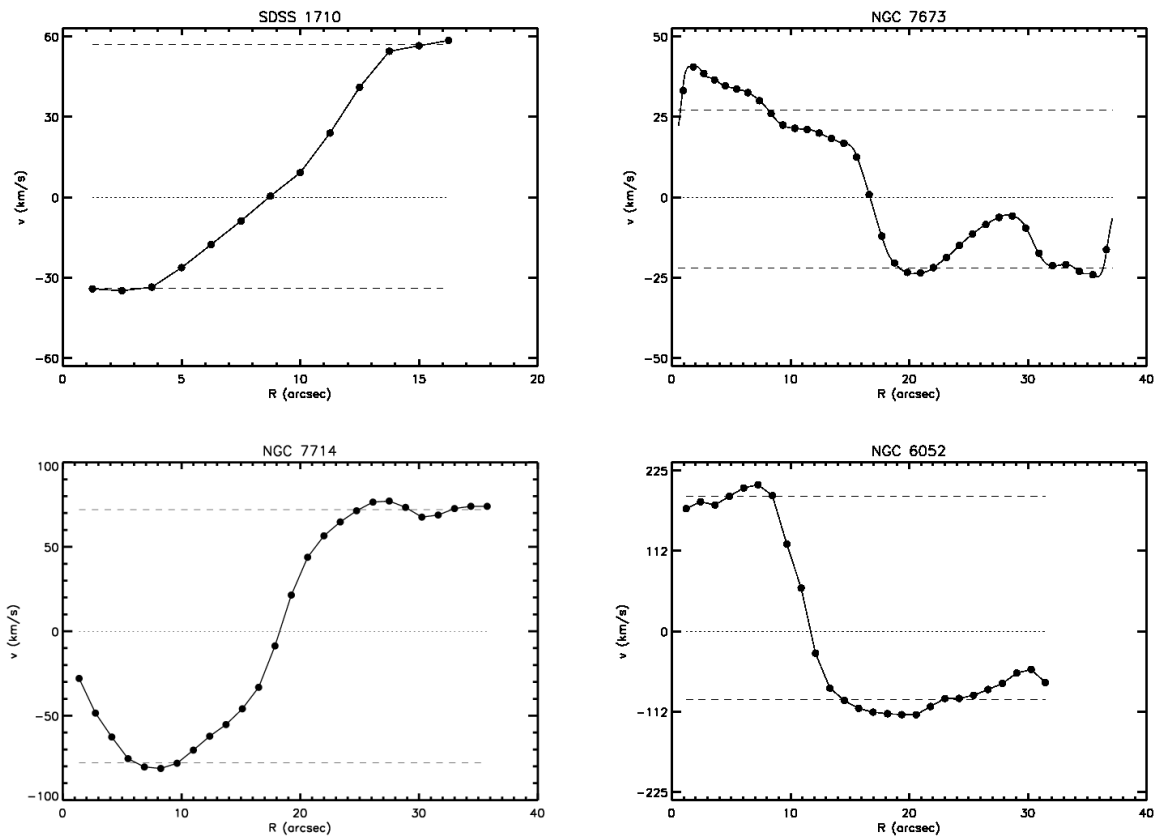

Figure 3-3. Rotation curves of SDSS 1710, NGC 7673, NGC 7714, and NGC 6052. For each LCBG, the dashed lines indicate the plateaus, while the dotted line indicates the velocity of the central velocity width peak, which is taken as a reference. The x-axis indicates the distance in arcsec from one extreme to the other of the major axis of the galaxy. The position of the central velocity width peak corresponds to the intersection of the rotation curve with the dotted line. The spatially resolved kinematic components of NGC 7673 (clump on the negative velocity side) and NGC 7714 (arc on the negative velocity side) can be easily seen although they were not taken into account in the analysis.

where a and b are the major and minor axis respectively. The SDSS isophotal major and minor axes in the r band (6230 Å) were used. Inclinations from Garland et al. (2004) were used for NGC 7714 and NGC 6052. The inclinations for NGC 7673 and NGC 469 were taken from Pisano et al. (2001) and HyperLeda[1] respectively. Inclinations for the UCM

[1] http://www-obs.univ-lyon1.fr/hypercat

galaxies were calculated from data available in the UCM catalog by

$$i = \arccos \sqrt{\frac{(b/a)^2 - 0.2^2}{1 - 0.2^2}} + 3 \ , \tag{3–2}$$

where a and b are the major and minor axis respectively (Tully & Fisher, 1988), as suggested by the UCM collaboration. If an uncertainty of $\pm 10\%$ in the inclination is assumed, v_{rot} would range, on average, from $\pm 10\%$ in v_{rot}.

On the other hand, Table 3-2 lists the presence and properties of both spectral and spatially resolved components. Spatially resolved components were identified by studying the velocity map of each galaxy, while spectral independent components were identified by studying the non-gaussianity of the spectra of each galaxy as explained in Chapter 2. The number (N), extension (A; area in comparison with the area of the galaxy), and average velocity with respect to their surroundings ($\overline{\Delta v}$) are listed for the latter. The extension (A; area in comparison with the area of the galaxy), the average intensity between components ($\overline{\Delta I_{max}}$), and the average distance between components ($\overline{\Delta \lambda_c}$) are listed for the former.

Three of the galaxies in our sample show spatially resolved kinematic components decoupled from the rest of the galaxy. The detection of such components were possible in rotating systems since they were identified as a kinematically decoupled region within a rotating background. These kind of detections would have been also possible, for example, within an homogeneous velocity map in a face-on galaxy. NGC 7673 shows two spatial kinematic components moving at an average speed of 35 ± 4 km s^{-1}, while the arc of NGC 7714 is moving at an average speed of 63 ± 5 km s^{-1}. Furthermore UCM 2327 shows two extra components located at its core moving at an average speed of 193 ± 34 km s^{-1}. All five components in the three galaxies are moving away from the observer and falling towards the galaxy, if we assume the galaxy is opaque. This opacity may also explain why we do not see components moving towards the observer and falling towards the galaxy, since they would be behind the galaxy. The detection of these components is limited

Table 3-2. Kinematic Components

Name	Spectral Components				Spatial Components		
	A (%)	$\overline{\Delta I_{max}}$ (%)	$\overline{\Delta\lambda_c}$ (Å)	(km s^{-1})	N	$\overline{\Delta v}$ (km s^{-1})	A (%)
NGC 7673	...	...	...		2	35 ± 7	3.0 ± 0.7
NGC 7714	6.8 ± 0.7	45 ± 9	2.3 ± 0.4	136 ± 3	1	63 ± 14	5.8 ± 0.6
NGC 6052	20 ± 1	43 ± 6	3.0 ± 0.2	177 ± 2	...	...	...
NGC 469	...	...	...		...	...	...
UCM 0000	22 ± 4	41 ± 12	5.3 ± 1.3	311 ± 10	...	...	...
UCM 0156	13 ± 6	48 ± 35	3.3 ± 0.6	195 ± 5	...	...	...
UCM 1428	3 ± 3	71 ± 10	1.9 ± 0.1	112 ± 1	...	...	...
UCM 1431	...	...	...	...	...	...	...
UCM 1648	...	...	...	...	...	...	...
UCM 2250	...	...	...	...	...	...	...
UCM 2258	...	...	...	...	...	...	...
UCM 2317	...	...	...	...	2	193 ± 90	4.0 ± 0.6
UCM 2327ns	...	...	...	...	...	...	...
SDSS 1134	...	...	...	...	...	...	...
SDSS 1507	...	...	...	...	...	...	...
SDSS 1605	...	...	...	...	...	...	...
SDSS 1652	...	...	...	...	...	...	...
SDSS 1703a	...	...	...	...	...	...	...
SDSS 1703b	...	...	...	...	...	...	...
SDSS 1710	9 ± 4	73 ± 24	1.8 ± 0.5	106 ± 4	...	...	...
SDSS 2327	...	...	...	...	...	...	...
Averages[a]	12 ± 7	54 ± 15	2.9 ± 1.3	170 ± 76	1.7 ± 0.5	97 ± 84	4.3 ± 1.4

[a] Mean and standard deviation of the sample

by our ability to find compact kinematic structures with velocities three sigma larger or smaller than their surroundings. Such components are therefore difficult to find in those galaxies with the smallest apparent effective radii. The area of these components was calculated by comparing the number of fibers per dithering in which they were detected with the number of fibers per dithering in which the galaxy was detected. It is important to notice that because of the nature of our analysis the number and extension of these components are indeed lower limits, and galaxies where they were not detected might or might not host them. The minimum size we can measure corresponds to one fiber, which is 2.7 arcsec across (i.e., $\sim$1 kpc at the average redshift of our sample). The area of these components was calculated by comparing the number of fibers per dithering in which they were detected with the number of fibers per dithering in which the galaxy was detected.

Six of the galaxies in our sample are found to show spectrally resolved kinematic components in about a tenth of their area after investigating their spectra. The typical distance between these is 2.9 Å, which at the average redshift of the galaxies in our sample implies an offset of about 170 km s^{-1}. Furthermore, on average, one of the components is twice as intense as the other. The detection of these components is limited by the spectral resolution and the S/N of our data. The spectral resolution of our data is, as discussed in Chapter 2, $\sim$2.3 Å FWHM ($\sigma \sim$ 60 km s^{-1} at 5040 Å) and we should be able to measure broadening effects down to $\sim$40 km s^{-1}. However, after investigating our analysis of the residuals of our Gaussian profile fit procedure we found we were able to identify broadening effects down to $\sim$60 km s^{-1}, and offsets between components of $\sim$1 Å ($\sim$60 km s^{-1} at 5040 Å). Nevertheless, the offsets we measure for the different components identified in several galaxies of our sample are twice as large as this lower limit. Again, the area of these components was calculated by comparing the number of fibers per dithering in which they were detected with the number of fibers per dithering in which the galaxy was detected.

The average offset we measure is in good agreement with those measured by Marlowe et al. (1995) in a local sample of star-forming dwarf galaxies using Echelle spectra and Fabry-Perot images. While the comparison is obvious for the three of our galaxies that do not rotate, where we assume, as Marlowe et al. (1995), a bubble is responsible for the double profile, it is not for those that do rotate. For the latter, we consider that one of the components accounts for the overall rotating behavior while the other one accounts for a decoupled component. These filaments and/or "superbubbles" have the potential of being responsible for starburst-driven mass loss and their inability to retain newly synthesized metals, and therefore low metallicities. For a correlation between these I refer the reader to Castillo-Morales, Gallego, Pérez-Gallego, et al. (2010).

Only NGC 7714 shows both spectral and spatial kinematic components. Furthermore, NGC 7714 and UCM 2317 are the only galaxies for which an estimation for v_{rot} was possible while also having either a spectral or spatially resolved kinematic component. The rotating nature of UCM 2317 was actually found after removing these components (Figure 3-17).

UCM 0000 shows, not double, but triple spectral kinematic components in 4% of its area, and a broad component (8.0 Å FWHM, which translates into σ ~200 km s^{-1} at the redshift of the galaxy) in 12% of its area (Figure 3-4). This is the only galaxy in our sample showing an obvious broad emission line component. An attempt to investigate the nature of this component was made by calculating the [OIII]λ5007/Hβ, [NII]λ6584/Hα, and [SII]$\lambda\lambda$6717,6731/Hα ratios for the particular region of the galaxy (i.e., 0.95, -0.18, and -0.55 dex, respectively), to study the possible presence of AGN activity. Figure 3-5 shows the BPT diagram (Baldwin et al., 1981) for emission-line galaxies in the SDSS as in Figure 2 of Obrić et al. (2006). Emission-line galaxies can be separated into two groups according to their position in the BPT diagram: AGNs, and star-forming, using the separation boundaries outlined by the dashed line. These ratios for UCM 0000 are in good agreement with those of an AGN (Osterbrock, 1989). Furthermore, the pressure

derived from the [SII]$\lambda\lambda$6717,6731/Hα ($\sim$ 0.4) and [NII]$\lambda\lambda$6548,6584/Hα ($\sim$ 0.2) ratios are in agreement with that of a Seyfert galaxy (Rickes et al., 2008). Therefore, UCM 0000, is the only galaxy among our sample of 22 LCBGs to show clear evidence for AGN activity. Notice that while the broad component was detected in the V1200 configuration, the V300 configuration, where all components are blended, was used to estimate these ratios. Therefore, these ratios may be lower limits.

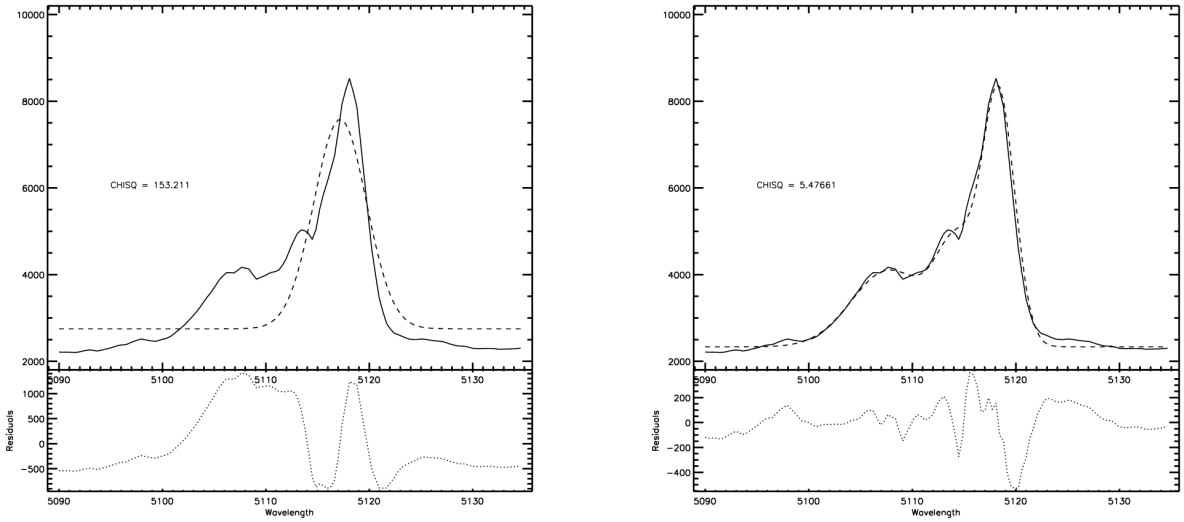

Figure 3-4. Single and triple Gaussian profile fits are shown (dashed line) for this particular spectrum of UCM 0000.

Ten of the galaxies in our sample are known to have a companion. Two of those are found within the FOV of two of our galaxies (SDSS 1134 and SDSS1605). One of those was found after comparing its properties as listed in the SDSS catalog (SDSS 1703a and SDSS 1703b). The rest were found in the literature through the NASA Extragalactic Database.

We find that almost half of our sample rotates, being the average ratio $v_{rot}/\sigma \sim 2$, which indicates the rotation-dominated nature of these particular objects. Local LCBGs show velocity widths typically ranging from $\sim$30–100 km s^{-1}, which are in agreement with the range found at intermediate redshift (e.g., Guzmán et al., 1997). Nevertheless,

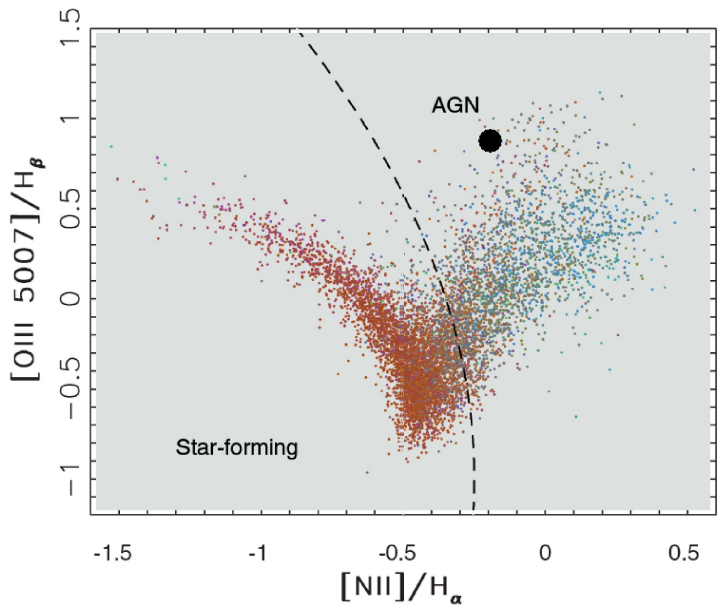

Figure 3-5. BPT diagram for SDSS emission-line galaxies (note that the line flux ratios are expressed on a logarithmic scale). UCM 0000 AGN candidate is shown as a big black dot. Emission-line galaxies can be separated into two groups according to their position in the BPT diagram: AGNs, and star-forming, using the separation boundaries outlined by the dashed line.

two objects, UCM 0000 and SDSS 1134, show velocity widths as high as ∼200 km s^{-1}. While UCM 0000 owes its high velocity width to the presence of an underlaying broad component that is likely caused by an AGN, SDSS 1134's high velocity width is due to its rotating nature, which translates into the only double-horned velocity profile we identify among the integrated spectra of our sample. It is important to notice here that in order for the rotating nature of objects such as NGC 7673, NGC 7714, and UCM 2327 to be found, it is necessary first to identify their spatially resolved kinematic components, subtract them, and only then, measure v_{rot}.

Almost half of our typically mid- to late-spiral sample are known to have a companion. Half of these galaxies with a companion show a rotating nature and v_{rot} was derived for them. It is important to realize that objects such as NGC 6052, which is a merger of two galaxies, may owe their rotating nature to a projection effect according to the analysis of Garland et al. (2007). We study this scenario in Chapter 4.

On the other hand, local LCBGs do not typically show either spatially resolved kinematic components, or spectrally resolved kinematic components. Nevertheless, it is important to notice the limitations discussed throughout our analysis regarding the identification of both. Spatially resolved kinematic components are only easy to identify in objects with a smooth rotating nature underneath. On the other hand, an even higher spectral resolution would help approaching the search of spectrally resolved kinematic components. With this in mind, we find that when present, these show kinematic offsets of $\sim$120 km s^{-1}.

Two out of the three galaxies with spatially resolved kinematic components are found to have a companion, while two out of the six galaxies with spectrally resolved kinematic components are found to have a companion. Furthermore, only one of the galaxies found to have a companion, SDSS 1134, shows an unambiguous rotating nature (i.e., smooth velocity gradient, central velocity width peak, and no spatially resolved kinematic components). If we exclude also NGC 7714, whose spatially resolved kinematic component is a spiral arm, and ignore UCM 2258, which V1200 configuration was not available, we are left with five out of five galaxies with both a distorted kinematic behavior and a companion. Out of the 12 galaxies without a companion, six show also a distorted kinematic behavior. In fact, all the galaxies with a companion are either classified as PRs or CKs, or show spatially resolved kinematic components, which denotes the effects companions have on the kinematics of their pairs.

The difficulties found when trying to classify the objects in our sample into the different classes defined by Yang et al. (2008), leads us to be cautious about any interpretation that may follow the classification of such objects at intermediate redshift. As for our sample of local LCBGs we find 48% RDs, 28% PRs, and 24% CKs. Note that we were unable to properly classify UCM 2258, for which we do not have velocity width measurements. These numbers seem in disagreement with those of Yang et al. (2008). Nevertheless, if we do not consider NGC 7376, NGC 7714, and UCM 2317, for which

their rotating nature was found only after carefully investigating our data and removing asymmetries introduced by spatially resolved independent kinematic components, we would find 33% RDs, 28% PRs, and 39% CKs, which is in agreement with what Yang et al. (2008) found (i.e., 32% RDs, 25% PRs, and 43% CKs).

This shows how the technical limitation of distant observations may play a role in the kinematic classification of this galaxies. Thus, for example, the detection of a spiral arc, such as the one shown by NGC 7714 (Chapter 4), in the velocity map of a distant RD, for which the photometric determination of the spiral arc might not be possible, would turn it into a CK. Furthermore, minor mergers, such as the one shown by NGC 7673 (Chapter 4), would not be seen because of the actual size of the spatial resolution element on the sky. Also, projection effects in merger systems, such as NGC 6052 (Chapter 4), where the geometry of the galaxy pair makes it seem as if it was just one RD, affect the distinction between classes. All this is telling us that we have to be very careful with the percentages of RDs, PRs, and CKs derived for distant LCBGs.

This ambiguity may be particularly important when trying to estimate dynamical masses of distant LCBGs. Mass, not luminosity, is the fundamental quantity that remains constant throughout the evolution of these objects. It is unlikely for LCBGs to have experienced in the last ∼9 Gyr a large number of major mergers that would considerably have increased their masses; they are more likely, instead, to have evolved passively (Wolf et al., 2005; Bell et al., 2005). The presence of different asymmetries in the velocity maps might be important contributors to the velocity widths, together with the overall rotation of the system. This is an important thing to take into account when trying to estimate dynamical masses of distant LCBGs from their velocity widths. If we do not consider this, wrong dynamical mass estimates might lead to the wrong evolutionary scenario.

3.2 Atlas

Optical images, velocity (v) maps, and velocity width (σ) maps for our sample of 22 local LCBGs are shown next (Figures 3-6 to 3-26). When possible, an optical image from

the Sloan Digital Sky Survey is shown, otherwise an optical image form the Digital Sky Survey is shown. The physical scale of the optical image is that of the kinematic maps. Velocity maps and velocity width maps are shown with contours. The UCM 2258 velocity width map is not shown due to unavailability of the necessary data. Two velocity maps are shown for UCM 2317, one with the spatially resolved kinematic components found in Section 3.1, and a second one without those.

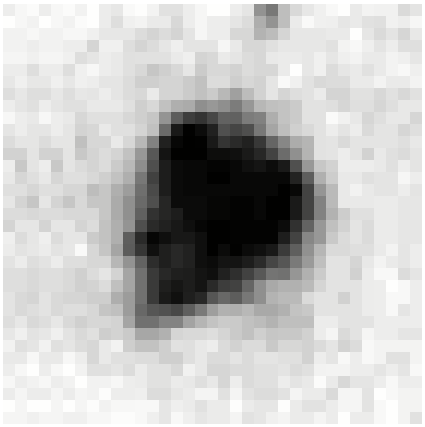

A

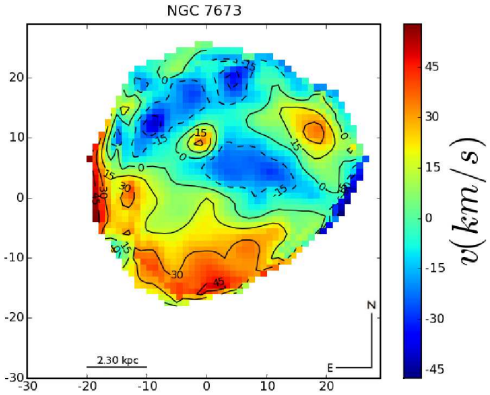

B

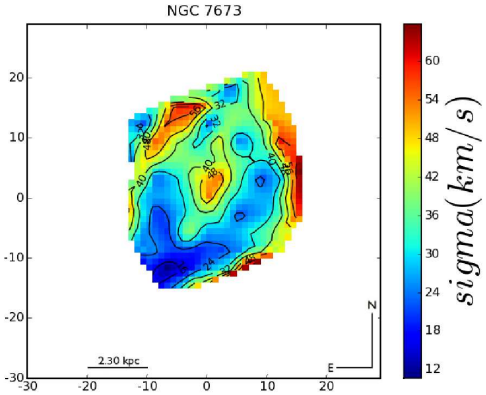

C

Figure 3-6. NGC 7673. A) DSS image. B) Velocity map. C) Velocity width map.

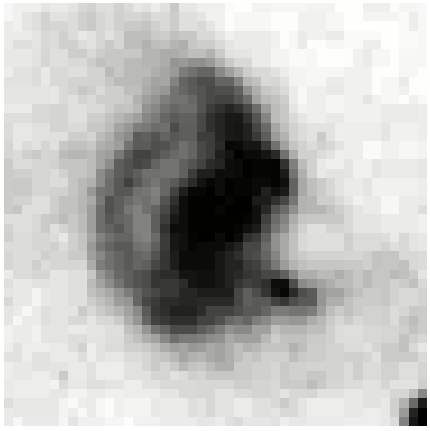

A

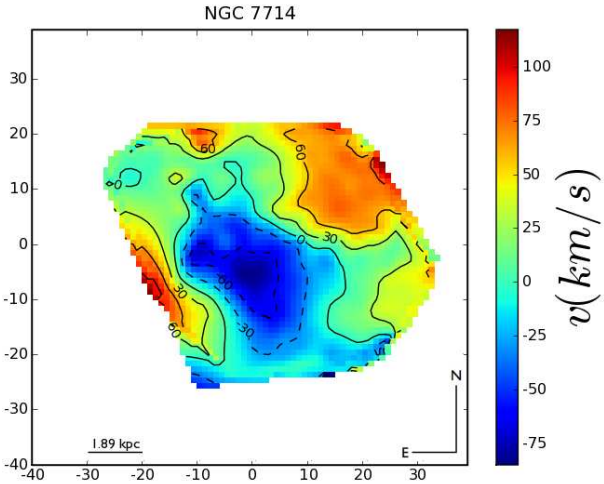

B

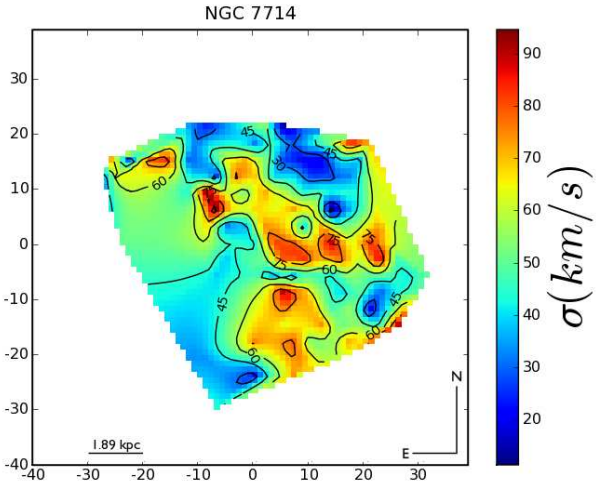

C

Figure 3-7. NGC 7714. A) DSS image. B) Velocity map. C) Velocity width map.

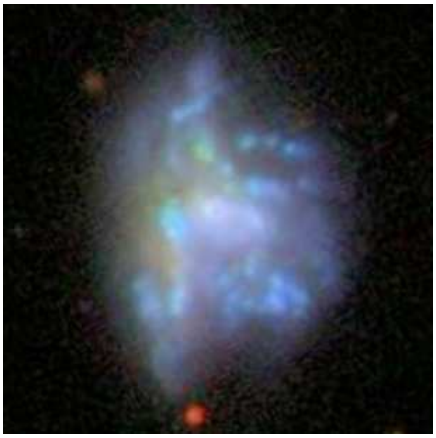

A

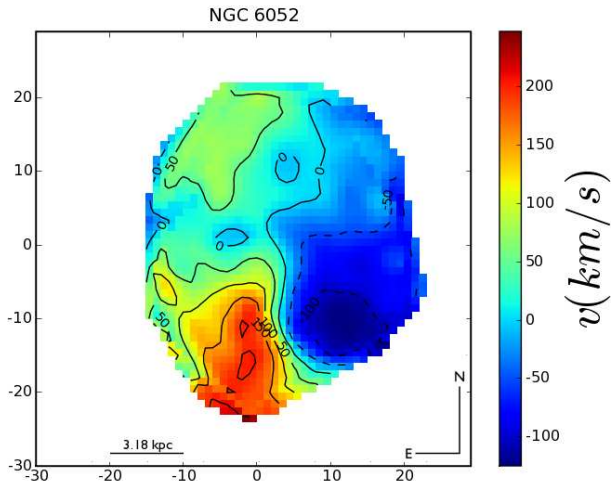

B

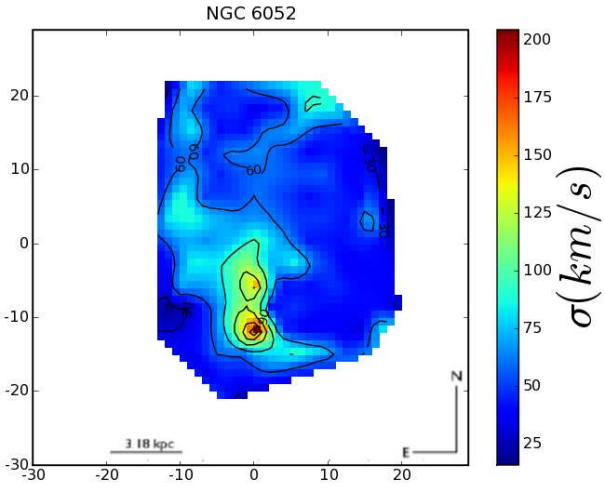

C

Figure 3-8. NGC 6052. A) SDSS image. B) Velocity map. C) Velocity width map.

A

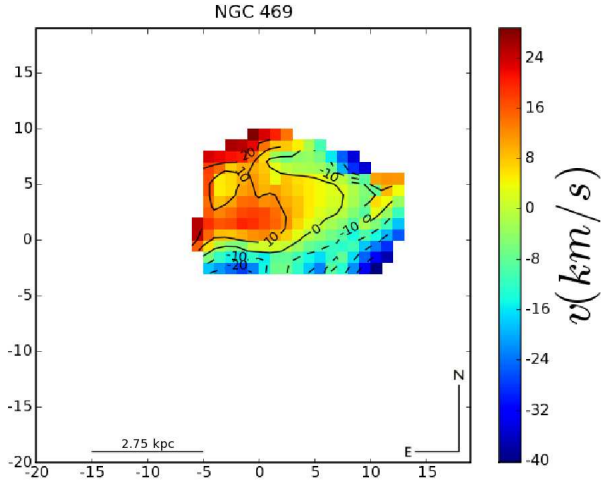

B

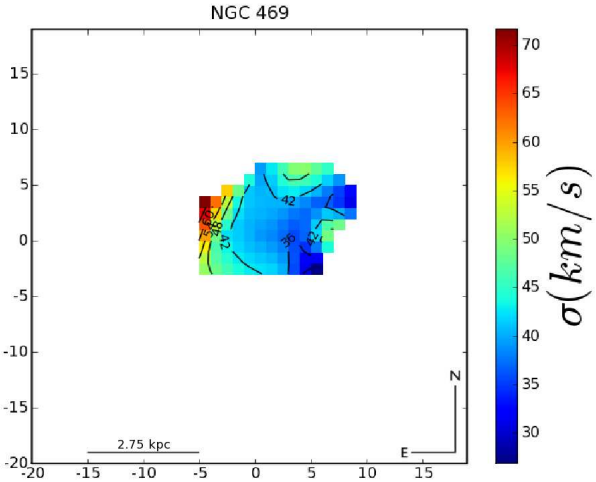

C

Figure 3-9. NGC 469. A) SDSS image. B) Velocity map. C) Velocity width map.

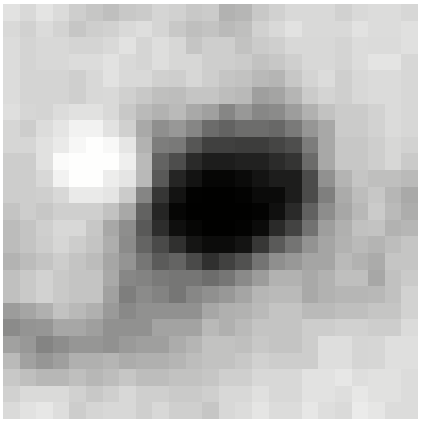

A

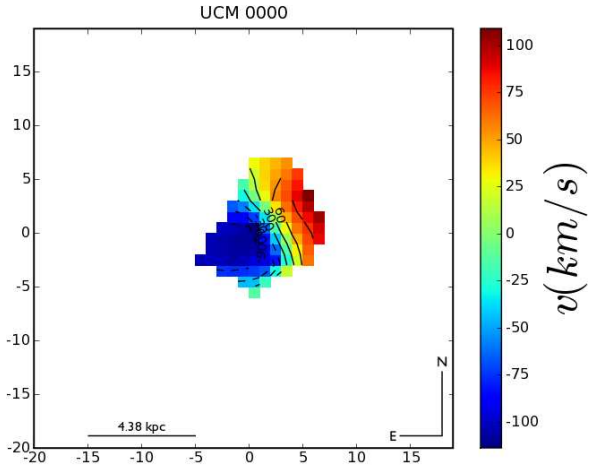

B

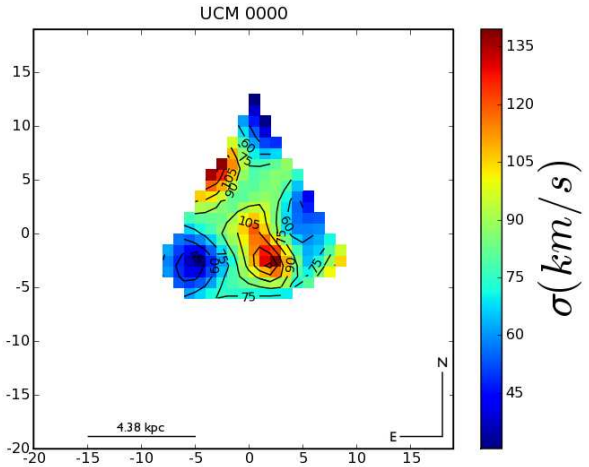

C

Figure 3-10. UCM0000. A) DSS image. B) Velocity map. C) Velocity width map.

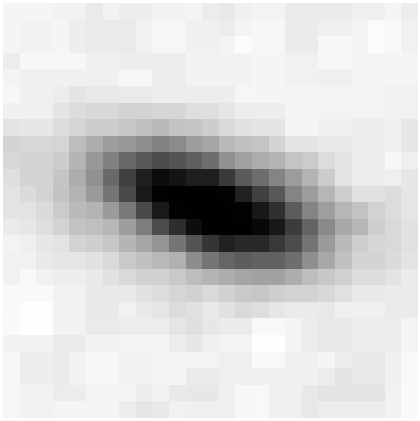

A

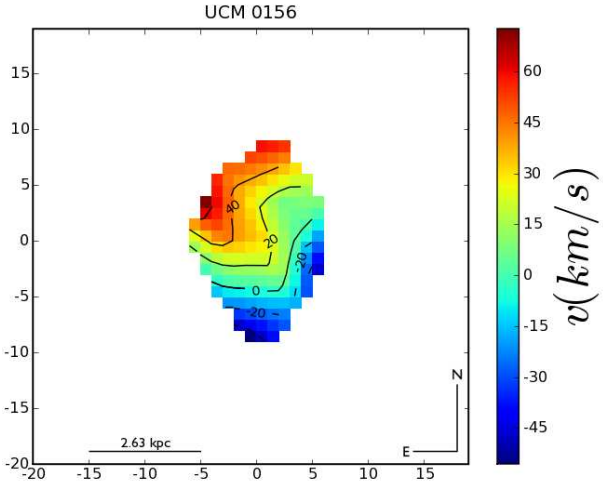

B

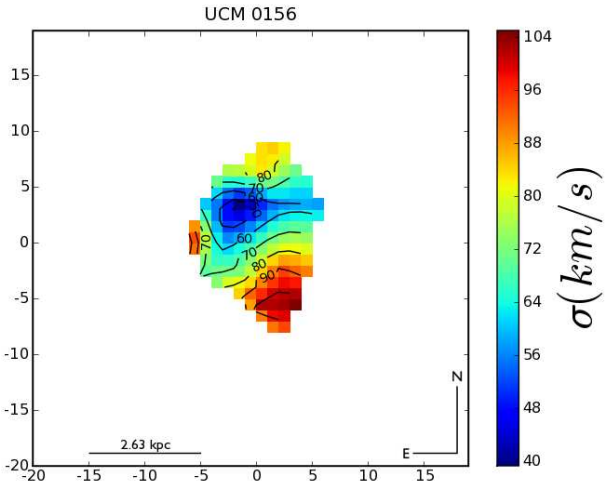

C

Figure 3-11. UCM0156. A) DSS image. B) Velocity map. C) Velocity width map.

A

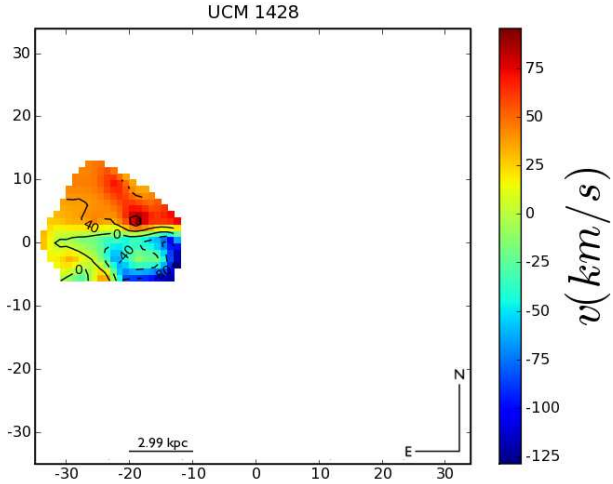

B

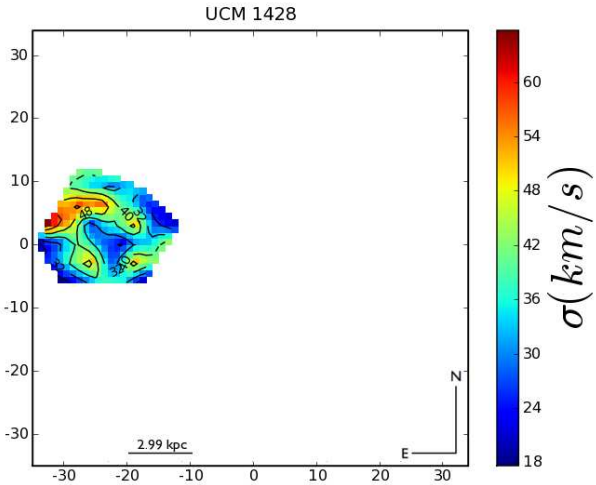

C

Figure 3-12. UCM1428. A) SDSS image. B) Velocity map. C) Velocity width map.

A

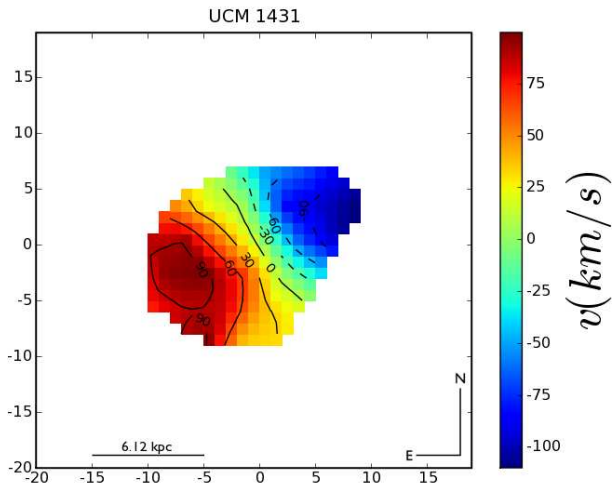

B

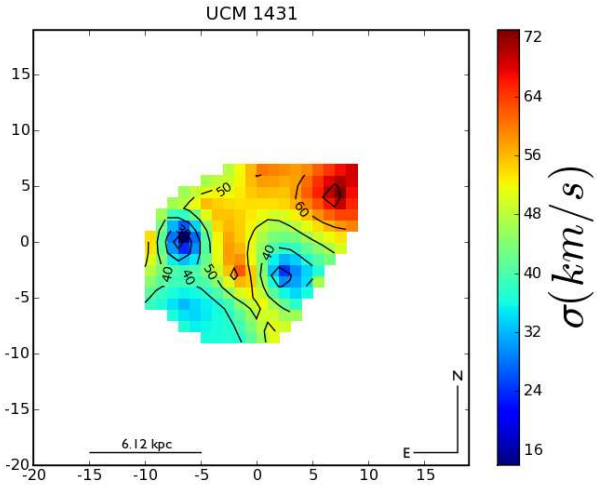

C

Figure 3-13. UCM1431. A) SDSS image. B) Velocity map. C) Velocity width map.

A

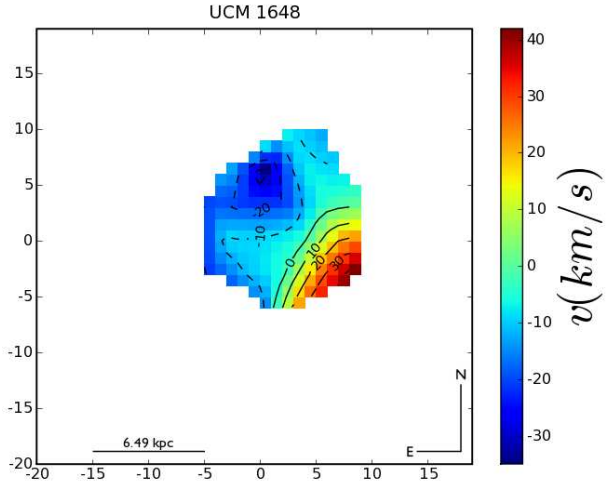

B

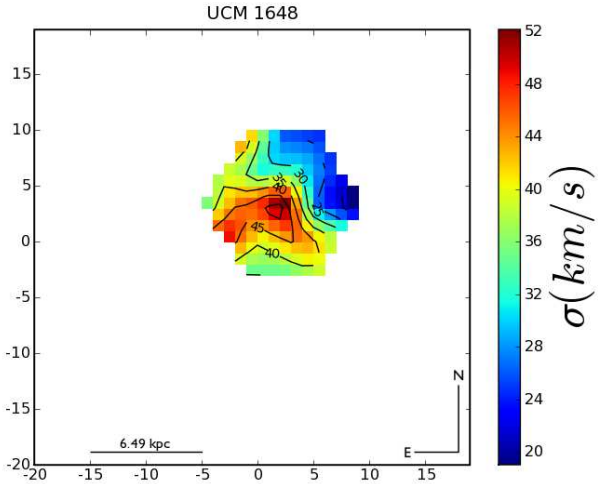

C

Figure 3-14. UCM1648. A) SDSS image. B) Velocity map. C) Velocity width map.

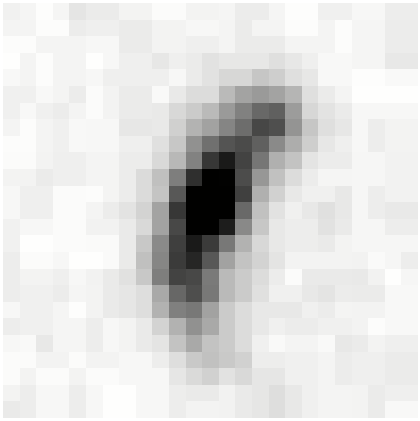

A

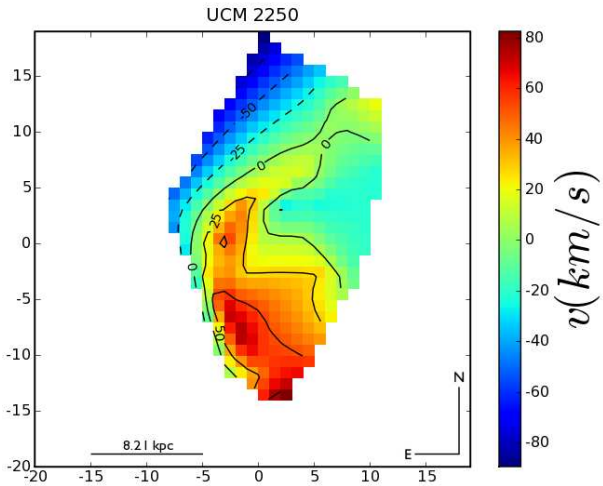

B

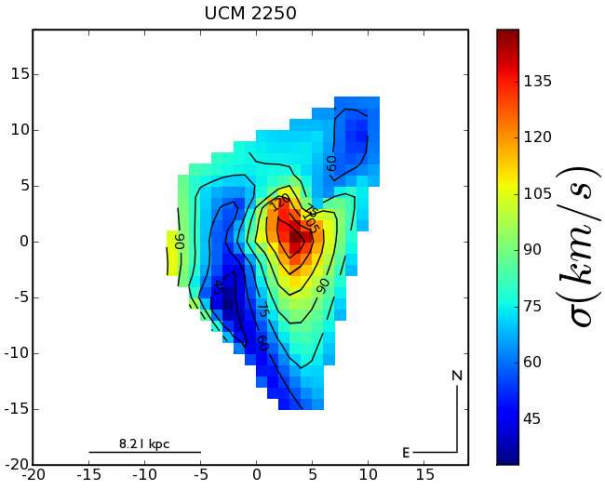

C

Figure 3-15. UCM2250. A) DSS image. B) Velocity map. C) Velocity width map.

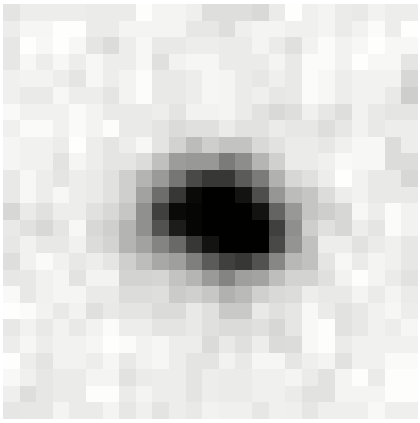

A

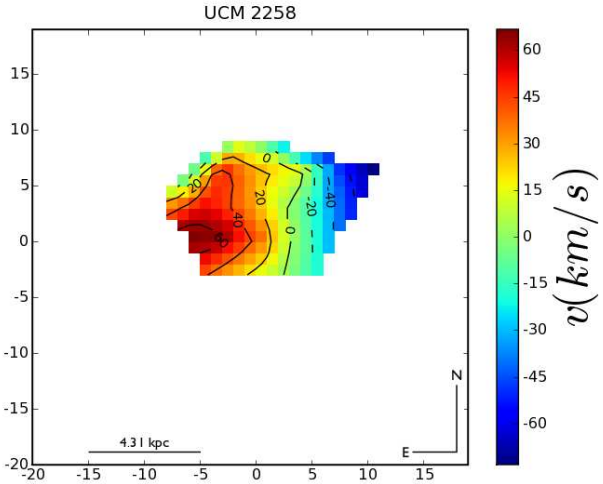

B

Figure 3-16. UCM2258. A) DSS image. B) Velocity map.

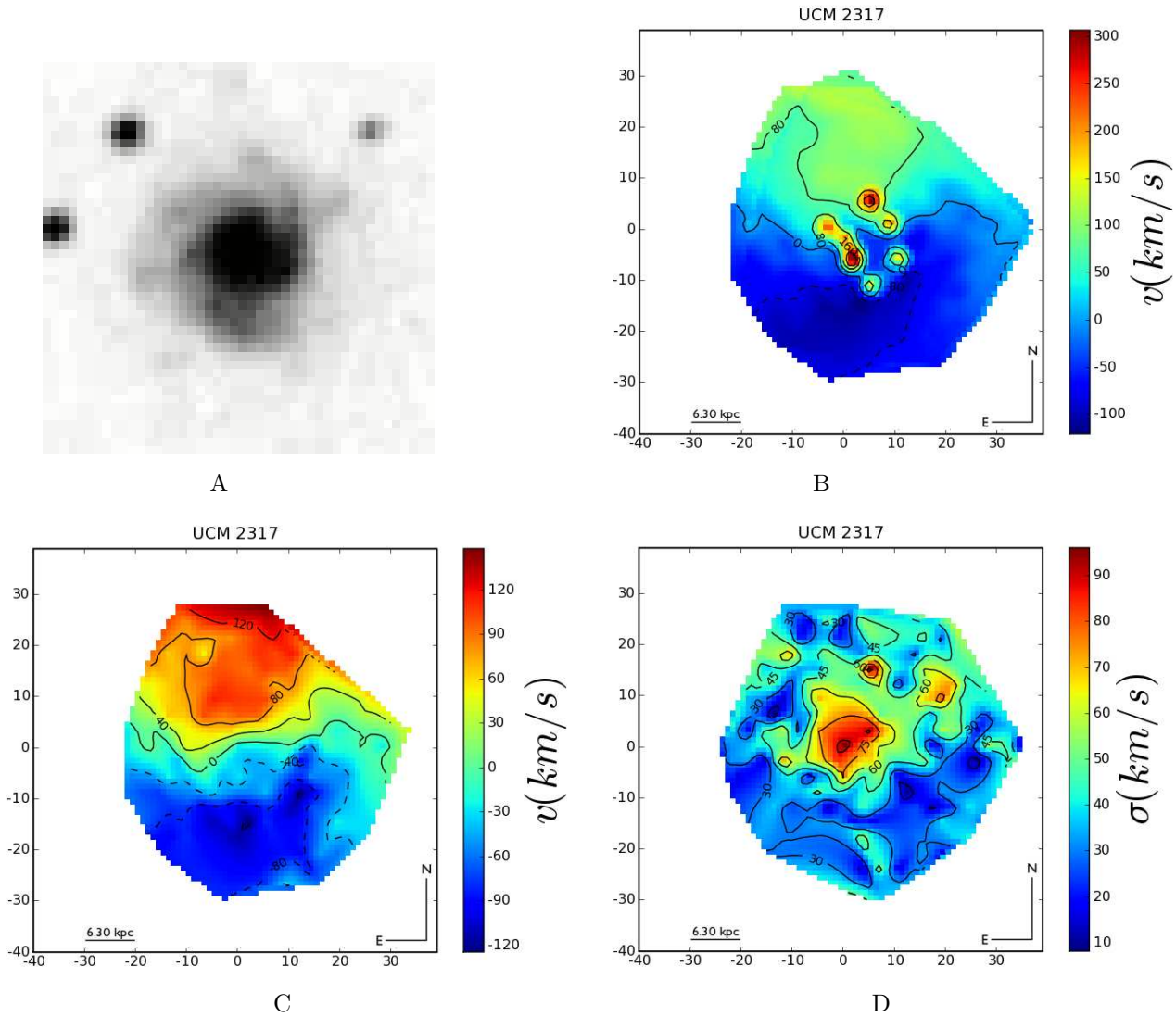

Figure 3-17. UCM2317. A) DSS image. B) Velocity map. C) Velocity map after subtracting spatially resolved kinematic components. D) Velocity width map.

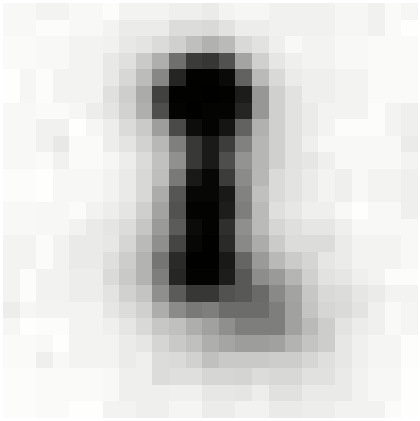

A

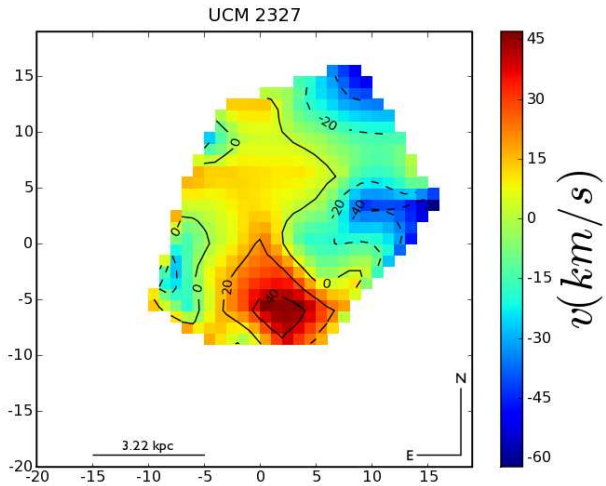

B

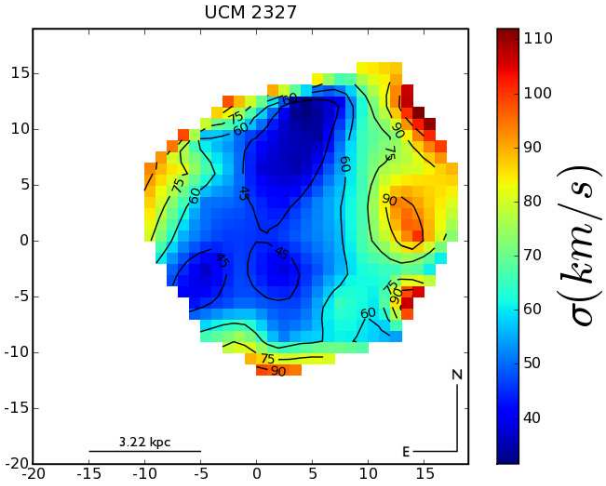

C

Figure 3-18. UCM2327. A) DSS image. B) Velocity map. C) Velocity width map.

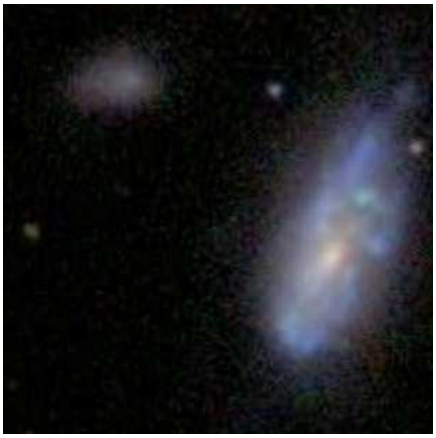

A

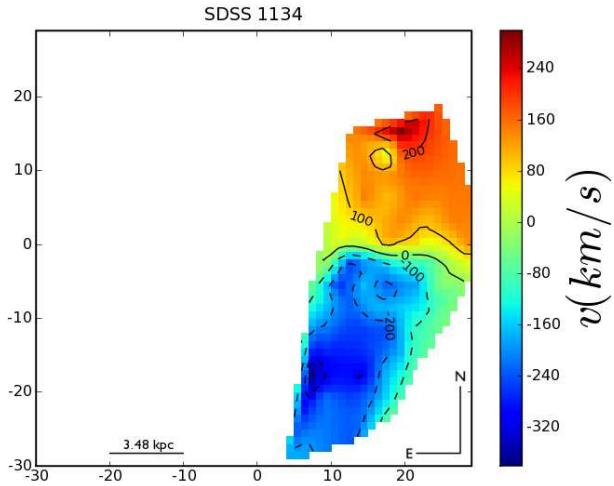

B

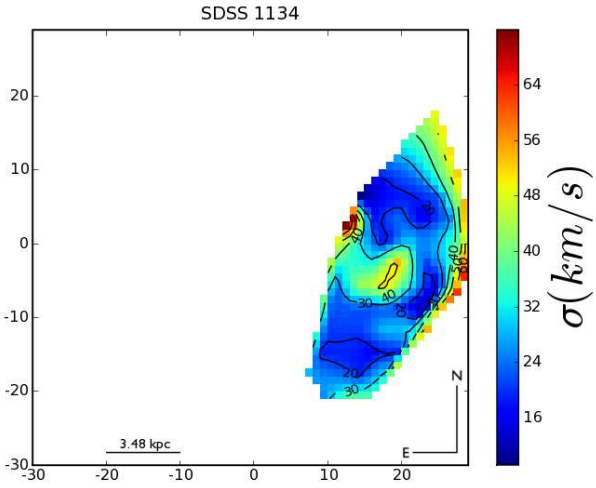

C

Figure 3-19. SDSS 1134. A) SDSS image. B) Velocity map. C) Velocity width map.

A

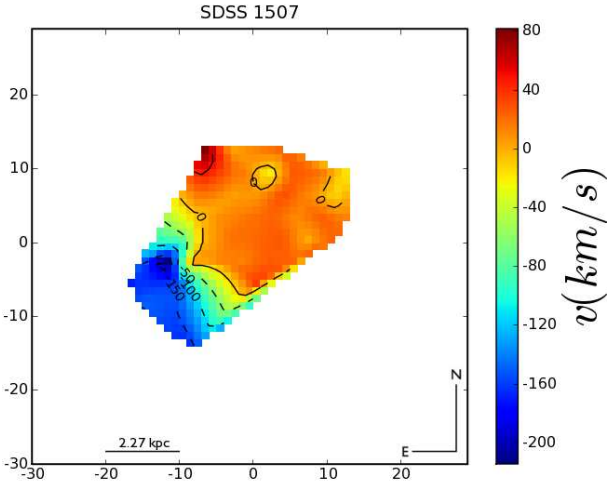

B

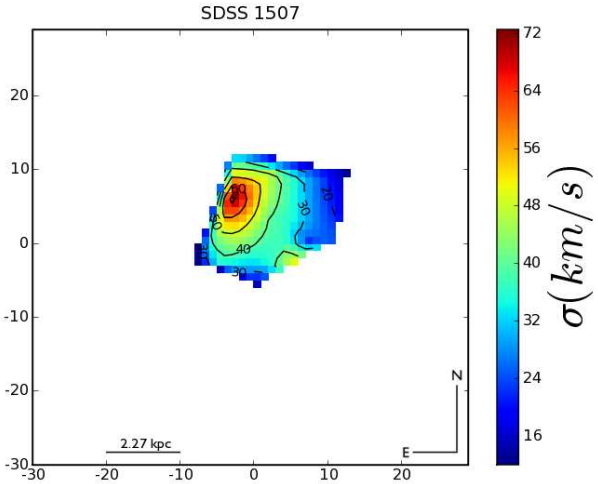

C

Figure 3-20. SDSS 1507. A) SDSS image. B) Velocity map. C) Velocity width map.

A

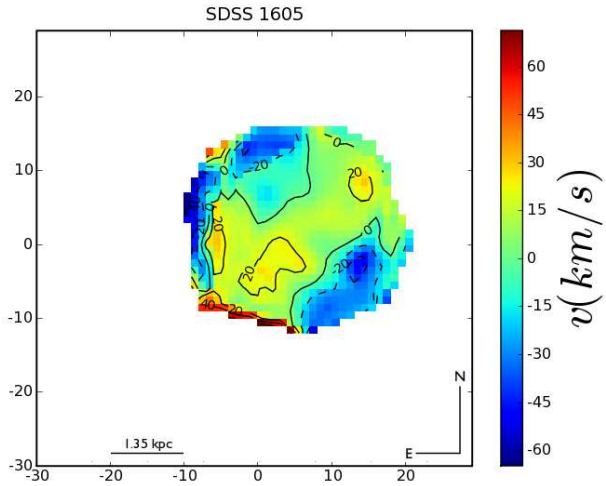

B

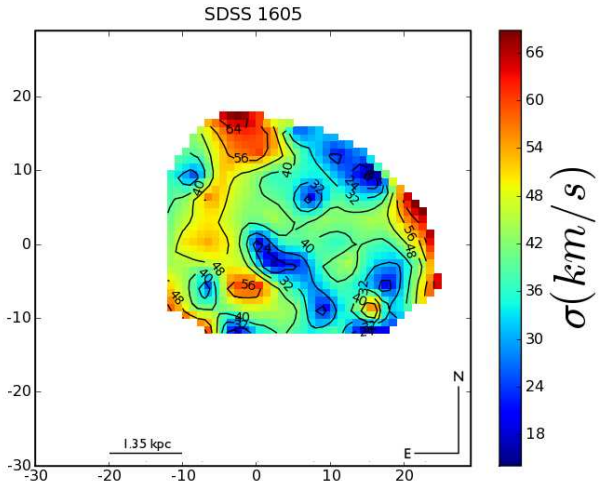

C

Figure 3-21. SDSS 1605. A) SDSS image. B) Velocity map. C) Velocity width map.

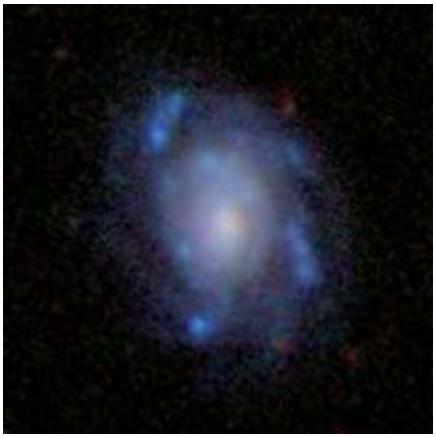

A

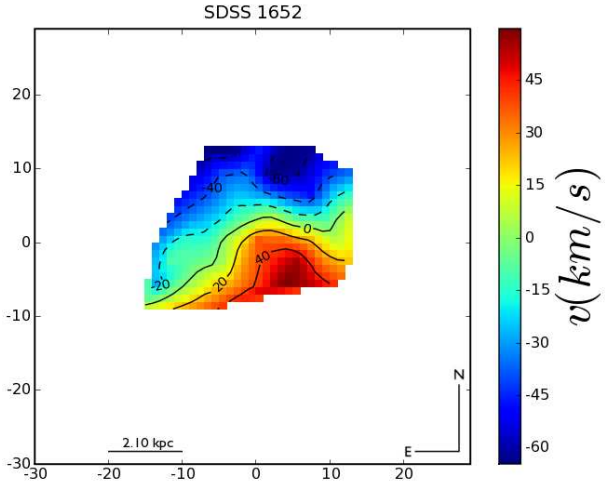

B

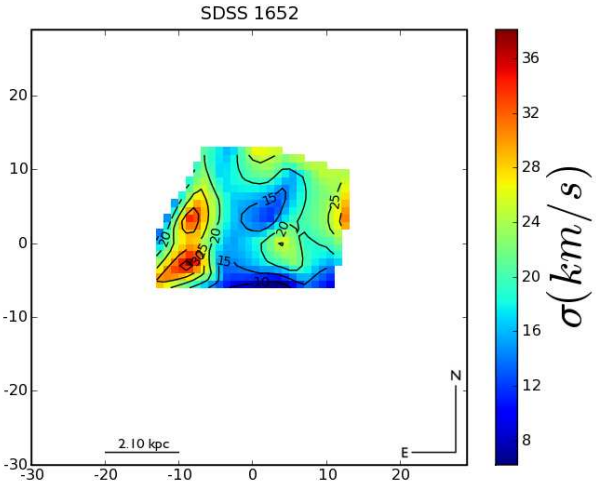

C

Figure 3-22. SDSS 1652. A) SDSS image. B) Velocity map. C) Velocity width map.

A

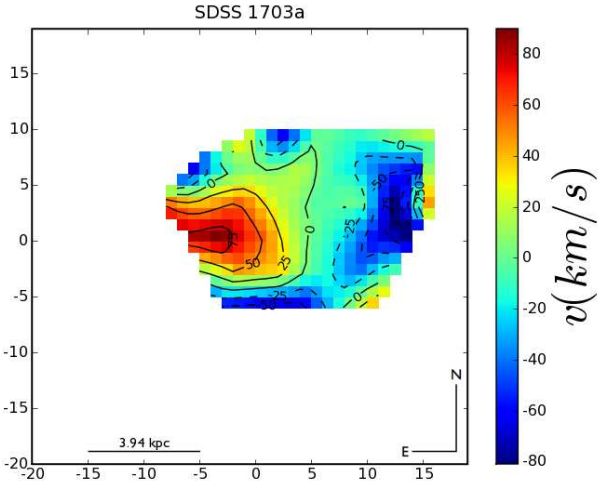

B

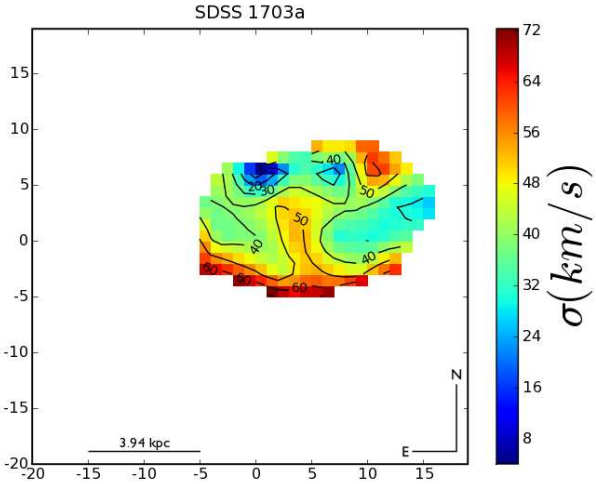

C

Figure 3-23. SDSS1703a. A) SDSS image. B) Velocity map. C) Velocity width map.

A

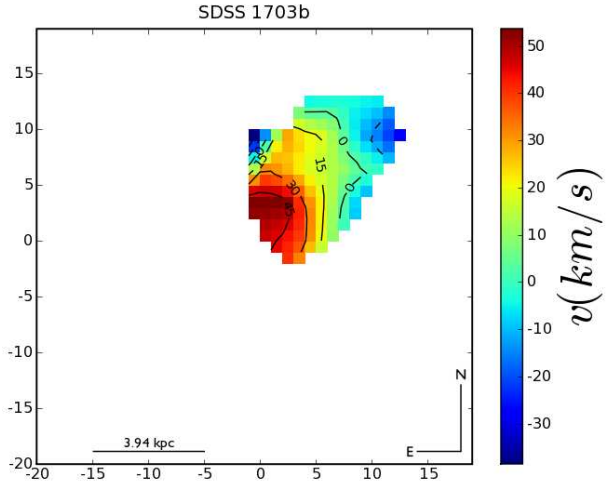

B

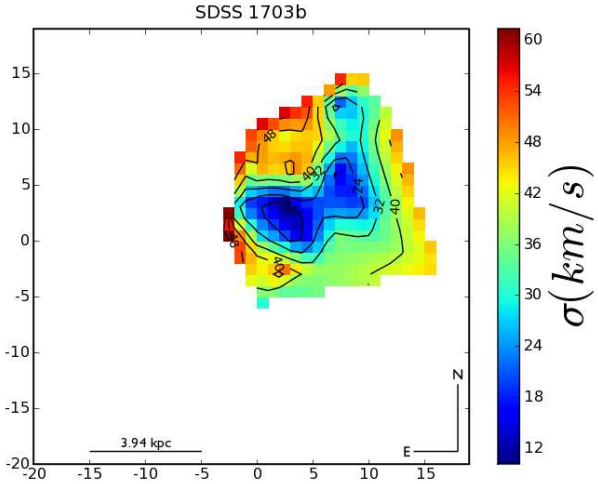

C

Figure 3-24. SDSS1703b. A) SDSS image. B) Velocity map. C) Velocity width map.

A

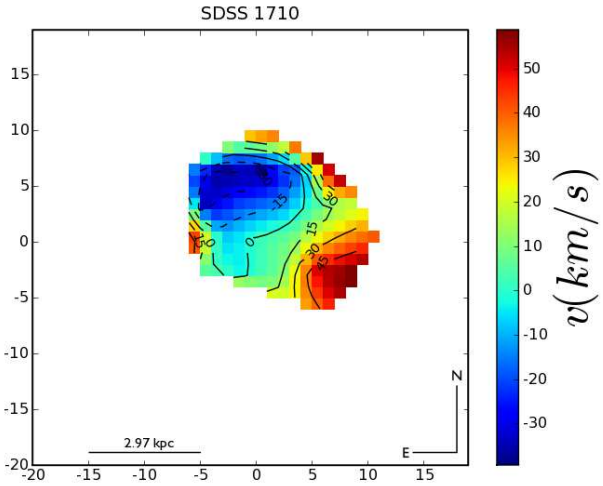

B

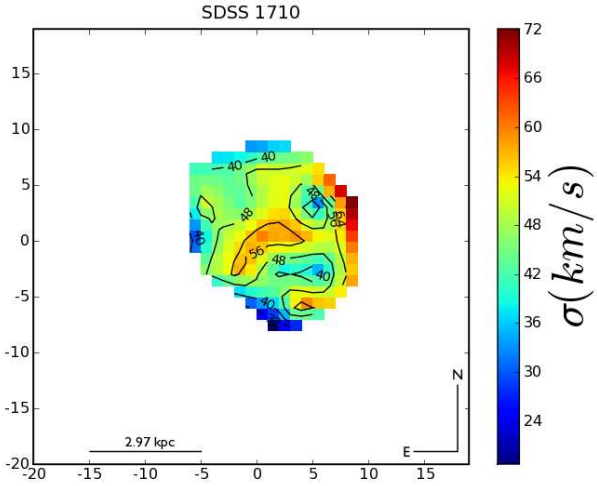

C

Figure 3-25. SDSS1710. A) SDSS image. B) Velocity map. C) Velocity width map.

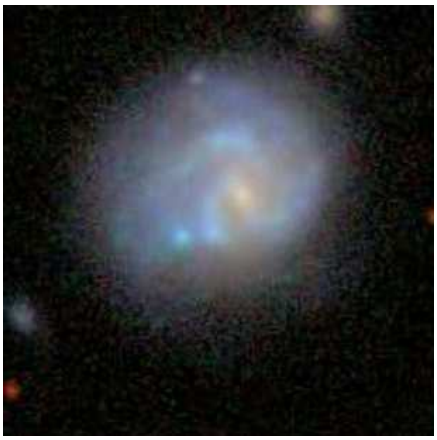

A

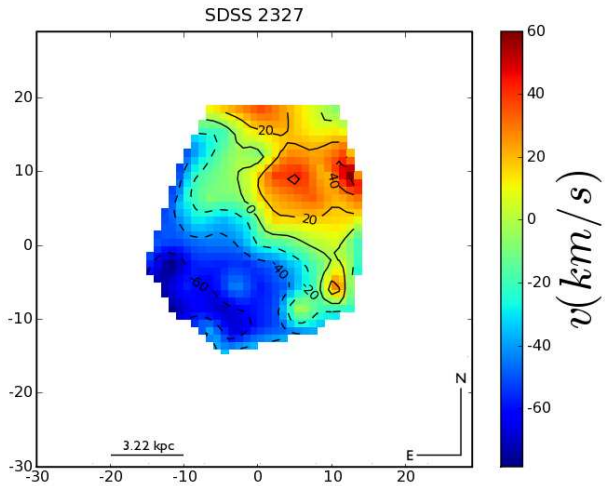

B

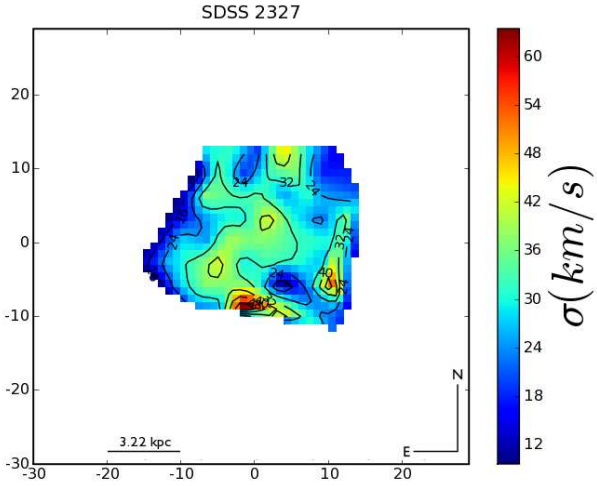

C

Figure 3-26. SDSS2327. A) SDSS image. B) Velocity map. C) Velocity width map.

CHAPTER 4
PROTOTYPICAL LUMINOUS COMPACT BLUE GALAXIES

4.1 Sample Selection

Among our sample of 22 local Luminous Compact Blue Galaxies (LCBGs) we selected four objects to carry out a further deeper analysis. These are NGC 7673, NGC 7714, NGC 6052, and NGC 469. These galaxies were selected both because of their intrinsic properties and because of the available data at different wavelengths (e.g., Garland et al., 2007; Pisano, Garland, Pérez-Gallego, et al., 2009b). In particular, NGC 469 is a compact field LCBG, NGC 6052 is a major merger (e.g., Alloin & Duflot, 1979), and NGC 7714 is the member of a galaxy pair (e.g., Smith et al., 1997). As for NGC 7673, it is a minor merger candidate as suggested in the past (e.g., Homeier & Gallagher, 1999) and investigated here.

4.2 NGC 7673

NGC 7673 (also known as MRK 325 and UCM 2325+2318) is a nearby (z = 0.011368) starburst galaxy that has been widely studied in the past (e.g., Duflot-Augarde & Alloin, 1982; Homeier et al., 2002; Pasquali & Castangia, 2008; Homeier & Gallagher, 1999, hereafter HG99). This irregular starburst galaxy (Figure 4-1) shows a clumpy structure with bright knots of star formation embedded in a diffuse halo that can be seen in the optical spectral range (HG99, Pérez-González et al., 2003). Duflot-Augarde & Alloin (1982) found 6 different star-forming clumps (Figure 4-1), some of which are referred to in this paper. From PPAK Hα fluxes Castillo-Morales, Gallego, Pérez-Gallego, et al. (2009a, hereafter CM09a) derived a star formation rate of at least 6.4 $M_{\odot}$ yr^{-1}. Furthermore, its small size, high surface brightness, strong emission lines and blue colors make NGC 7673 a prototypical LCBG (Table 4-1). NGC 7673 belongs to the UCM catalog.

HI 21 cm line mapping of NGC 7673 and its environment (Nordgren et al., 1997), which includes neighboring galaxy NGC 7677, roughly 7 arcmin to the southeast (3554

Table 4-1. NGC 7673 Observational Properties

Name	z^{a}	$M(B)^{a}$ (mag)	$SB_e{}^{a}$ (mag arcsec^2)	$B-V^{a}$ (mag)	$R_e{}^{a}$ (kpc)
NGC 7673	0.011368^{b}	-20.36	19.95	0.41	2.1
LCBGs^{c}	0.0189 ± 0.0019	-19.70 ± 0.20	20.30 ± 0.20	0.40 ± 0.02	2.16 ± 0.25

[a] UCM Catalog
[b] This gives a scale of 0.230 kpc arcsec^{-1}
[c] Mean and standard deviation of our sample

vs. 3405 km s^{-1}; HG99) shows a small outer irregularity that points to the latter. Nevertheless, a present major merger scenario has been rejected because of a remarkably constant velocity across the galaxy (Duflot-Augarde & Alloin, 1982). HG99 used data taken with DENSEPAK to study the kinematics of a portion of the galaxy. They were limited by the pointing of the telescope and both the field of view (FOV; 30 $\times$ 45 arcsec^2) and the spatial resolution of the instrument. Their spatial resolution sampling of two thirds of the galaxy, as seen in optical images, is highly improved by our sampling. Nevertheless, their spectral resolution (FWHM = 32 km s^{-1}) allowed them to find that a two component model, one narrow (FWHM $\sim$ 55 km s^{-1}) and one broad (FWHM $\sim$ 150 km s^{-1}) fit the observed spectra. According to their analysis three are the possible explanations for the presence of such a broad component: (i) a consequence of integrating over many ionized structures at different velocities; (ii) hot, turbulent gas confined to large cavities carved out by massive stars; and (iii) a starburst-powered galactic wind or similar break-out phenomenon. Furthermore, they exclude a present, but not past, interaction between NGC 7673 and NGC 7677, indicating a minor merger as the trigger mechanism for the major starburst.

PPAK observations of NGC 7673 were made during the nights of 2005 August 10 and 11 using two different setups as discussed in Chapter 2 (Table 4-2).

4.2.1 Velocity Map

The velocity map of NGC 7673 can be seen in Figure 4-2. Measurements of the velocity down to our S/N limit were possible for a region extending 40 arcsec in diameter.

Table 4-2. NGC 7673 Observing Log

Configuration	Dithering	Night	Exposure Time (s)	Offset (arcsec)
V300[b]	1	10 August 2005	3 × 330	(0.00, 0.00)[a]
V300	2	10 August 2005	3 × 330	(+1.56, +0.78)
V300	3	10 August 2005	3 × 330	(+1.56,−0.78)
V1200[c]	1	11 August 2005	3 × 900	(0.00, 0.00)[a]
V1200	2	11 August 2005	3 × 900	(+1.56, +0.78)
V1200	3	11 August 2005	3 × 900	(+1.56, −0.78)

[a] The original pointing of the telescope is 23:27:41.0 +23:35:20
[b] The V300 configuration was centered at 5361 Å covering the spectral range between 3591 and 6996 Å
[c] The V1200 configuration was centered at 5040 Å covering the spectral range between 4669 and 5395 Å

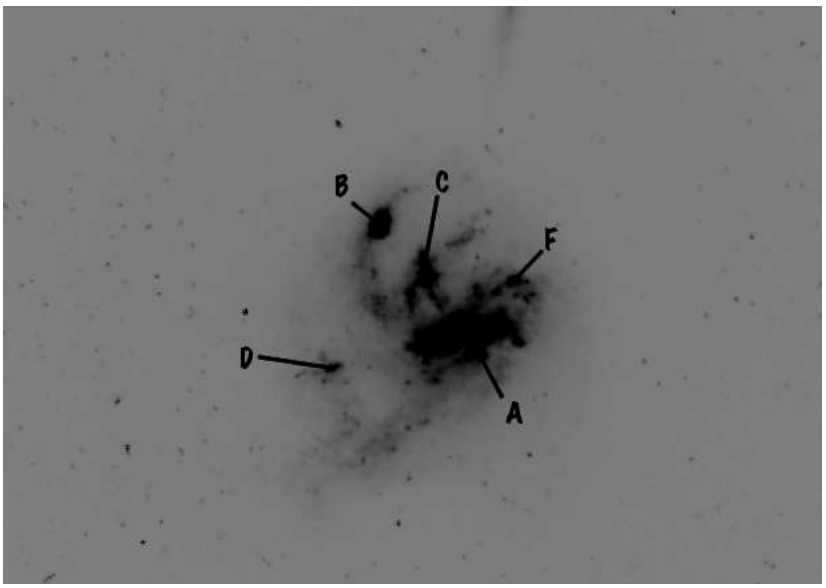

Figure 4-1. F555W WFPC2 image of NGC 7673 labeled with the star-forming clumps identified by Duflot-Augarde & Alloin (1982). North is to the top and East is to the left.

This compares well with the effective radius of the galaxy, which is 8.9 arcsec (r_e = 2.1 kpc, at the redshift of the galaxy). Further away, the S/N was not high enough to proceed to the measurement of the velocity. Border and pixelization effects due to the interpolation process were not considered in the analysis. These effects manifest as either a steep increase or steep decrease of the velocity towards the edges of the available data.

The velocity map shows an asymmetric velocity field that ranges from approximately -45 to 45 km s^{-1}. The velocities shown in the map are referenced to the redshift of the central peak velocity width of the galaxy (Section 4.2.3). No absolute calibration of the recession velocity was attempted. This redshift is 0.011293, smaller, but within two sigma of the one available in the NASA Extragalactic Database[1] .

The existence of an almost straight velocity contour that crosses the galaxy from east to west through the central velocity width peak suggests that it actually traces the position of the minor axis of the galaxy, yielding a major axis position angle (PA) equal to 168°. A PA of 122° derived from optical images taken from HyperLeda[2] was used in past studies of this galaxy. A rotation curve can be derived for both PAs by reading the measured velocities along the corresponding major axis (Figure 4-3). A PA equal to 168° provides a smoother rotation curve from which an uncorrected by inclination rotation velocity of about 30 km s^{-1} can be inferred.

While the southern half of the galaxy (darker) is consistently moving away from the observer, the northern half (lighter) is not uniformly moving towards. Two discrete regions located in the northern half of the galaxy are moving away from the observer in opposite direction to their surroundings.

First, we measure a smaller circular region, about 1 kpc wide, about 10 arcsec north of the center of the FOV. This region is moving away from the observer at about 35 km s^{-1} with respect to its surroundings. Furthermore, this region, although confined to only the area of one fiber, was detected on the three independent dithering exposures. Second, we identify a bigger elongated region, about 3.5 kpc long, which is located towards the northwest, about 2 kpc away from clump F. This is too far from the edge of the available data for us to consider it as a border effect. This region, considerably

[1] http://nedwww.ipac.caltech.edu/

[2] http://leda.univ-lyon1.fr/

more extended than the previous one, shows a smoother velocity gradient. Nevertheless, it also peaks at around 35 km s^{-1} with respect to its surroundings. We discuss below, in Section 4.2.4.1, whether these kinematically decoupled components show physical properties that differ from the rest of the galaxy.

When compared to the F555W WFPC2 image of NGC 7673 (Figure 4-2) two characteristics stand out: (i) the velocity field is considerably more extended than the region where the more luminous star forming regions are confined; and (ii) while the smaller decoupled region appears to be linked to clump B, no optical counterpart can be linked to the bigger one.

We compare our results to those of HG99 (Figure 4-4). Using the PPAK Hα image of the galaxy and Figure 3 from HG99, our and their FOV were registered by finding the position of two fibers mapping the same region of the galaxy. The DENSEPAK fiber array was drawn within the rectangular FOV on their figure for that purpose. This was needed because HG99 did not state the pointing position for their observations. A velocity map using their measurements was then produced down to a resolution of 1 arcsec using our interpolation method and reference system. This allowed us to directly compare both maps. The residual image reveals an offset of 20 km s^{-1} and a standard deviation of 12 km s^{-1}. While their better spectral resolution, as stated above, allowed them to look for multiple kinematic components, both our FOV and spatial sampling are better, which allows us to extend the study of the galaxy. The only notable difference between both maps is the presence of the small circular region in our data at the position of clump B. This could be explained by both the sampling and the dithering technique we used, since this region is not large enough for them to detect with their setup.

4.2.2 Neutral Hydrogen Gas

As discussed in Section 4.2.1, the velocity field of the galaxy derived from the centroids of the Hα emission line profiles shows asymmetries. The neutral hydrogen velocity field resembles the ionized one (Figure 4-5) in extent down to the detection limits,

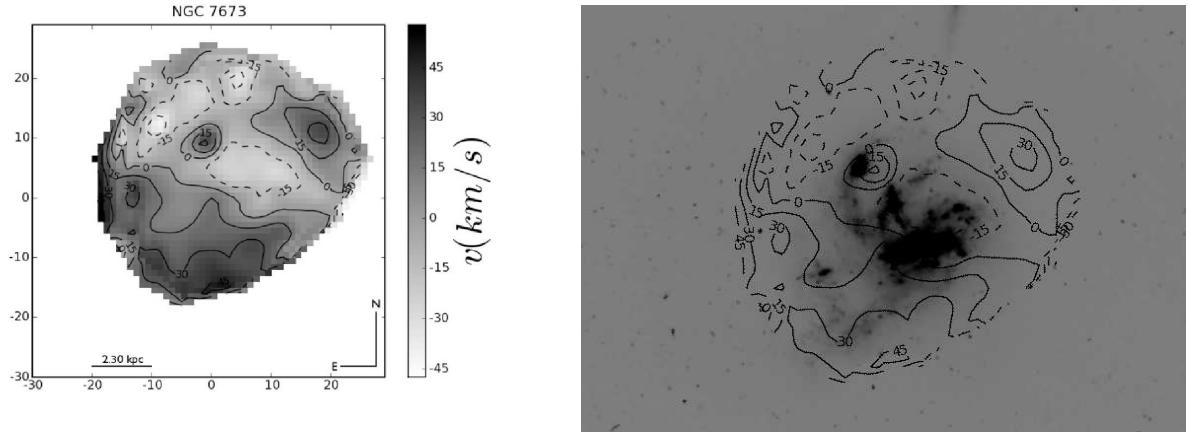

A B

Figure 4-2. A) PPAK Hα velocity map of NGC 7673 using the low resolution V300 configuration. The velocity map shows an asymmetric velocity field with at least two independent kinematic components in the northern side of the galaxy. B) PPAK Hα velocity map contours overlaid on the F555W WFPC2 image of NGC 7673. Clump B from Duflot-Augarde & Alloin (1982) can be identified with one of the independent kinematic component. There is no optical counterpart of the second one.

overall appearance, and velocity range ($\sim$90 km s^{-1}; Pisano, Garland, Pérez-Gallego, et al., 2009b).

Both maps were registered using the header coordinates. For the registration process several images were used: F555 HST, Hα PPAK, 6cm VLA, 20 cm VLA, and DSS. The uncertainty in the registration was established to be no higher than half an arcsecond. When the distributions of HI and HII are compared there is an obvious slight offset between them. The HII distribution extends slightly more towards the northeast while the HI one extends considerably more towards the west. This difference might be explained by two plane-parallel disks. The HII disk might be thicker than the HI and only the nearest side might be visible to us. If an inclination of 45° is assumed for both disks, a separation of about 1.7 kpc can be derived between the nearest side of the thicker HII disk and the HI disk. This is in agreement with the typical scale height of a thick disk (Howk & Savage, 2000). Nevertheless, the uncertainties associated with these estimations are quite large.

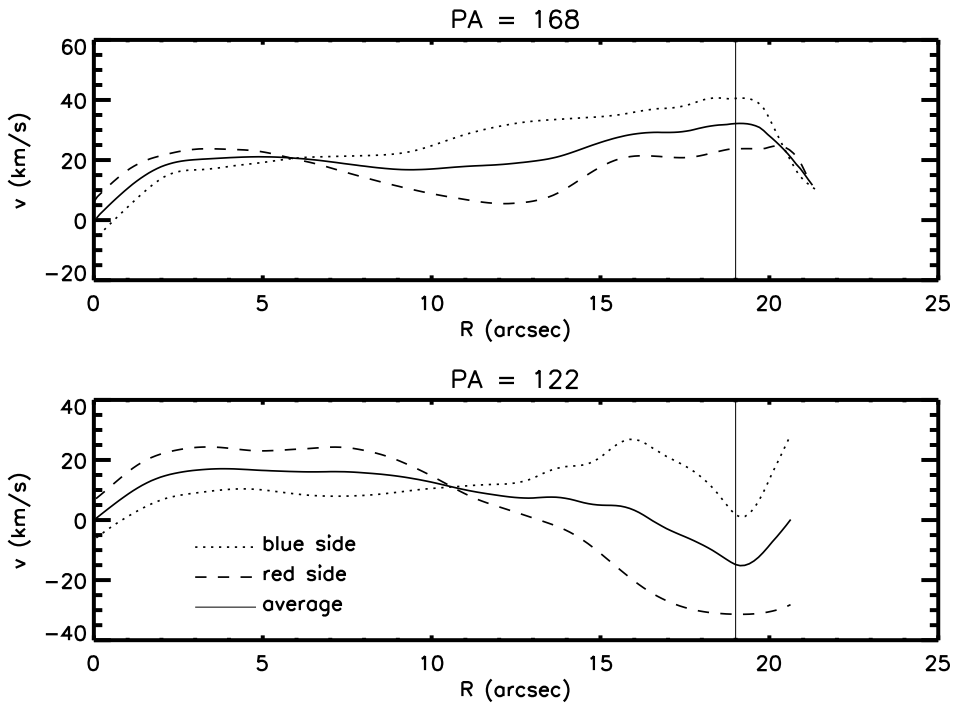

Figure 4-3. Rotation curves along the major axis of NGC 7673 for two different PAs. From our data we derive a PA equal to 168°, versus 122° from the Hyperleda catalog. The blue side (dashed line), red side (dotted line), and an average of both sides (solid line) of the galaxy are plotted.

On top of that, a residual image was generated by subtracting the optical velocity map from the radio one for the shared area. The resulting mean and standard deviation are 0 and 15 km s^{-1}, which make them consistent with each other. When only the receding part of the galaxy was considered these numbers were 8 and 9 km s^{-1} respectively indicating that there is not a cancellation effect between the receding and the approaching sides of the galaxy.

On the other hand, while the distribution of the HI resembles that of the ionized gas, the H_2 distribution, as traced by CO observations, is concentrated along clump A (Garland et al., 2005); no CO was detected in clump B. It is to be noted that the higher column densities of HI trace the location of CO. This lack of CO detection in clump B could be explained if the burst was quenching, opaque to CO radiation, or being injected

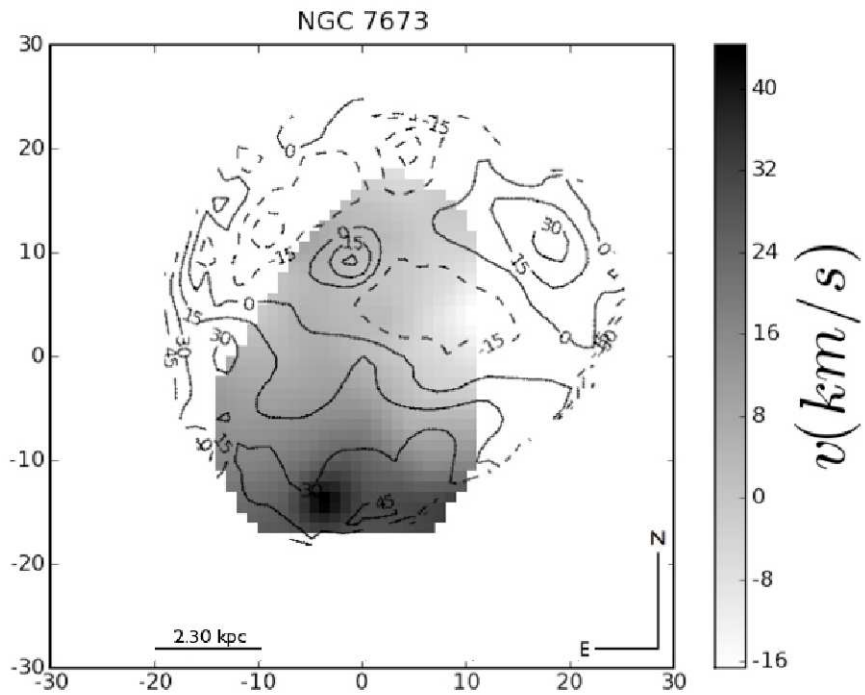

Figure 4-4. PPAK Hα velocity map contours of NGC 7673 overlaid on the DENSEPAK Hα velocity map of NGC 7673 from HG99. Both velocity maps are consistent within their respective uncertainties.

with HI through galactic winds. At the current SFR (CM09a) the HI still present in NGC 7673 ($M_{\rm HI} = 4.09 \times 10^9$ M$_\odot$; Pisano et al., 2001) would be exhausted in about 1 Gyr.

4.2.3 Velocity Width Map

The velocity width map of the galaxy (Figures 4-6 and 4-7) can be used in combination with the velocity map to better understand the kinematic properties of the galaxy. In virialized systems the velocity width peak tends to coincide with the centroid of the velocity map, assuming it is organized rotation which dominates the galaxy motions.

The velocity width map of NGC 7673 peaks ($\sigma = 54 \pm 5$ km s^{-1}) around the center of the FOV, between clumps A and C (Figure 4-6). This position roughly coincides with the luminosity-weighted center (photometric) and the center of the outer-isophotes (geometric) of the galaxy. These are located respectively about 3 and 4 arcsec (920 and 690 pc

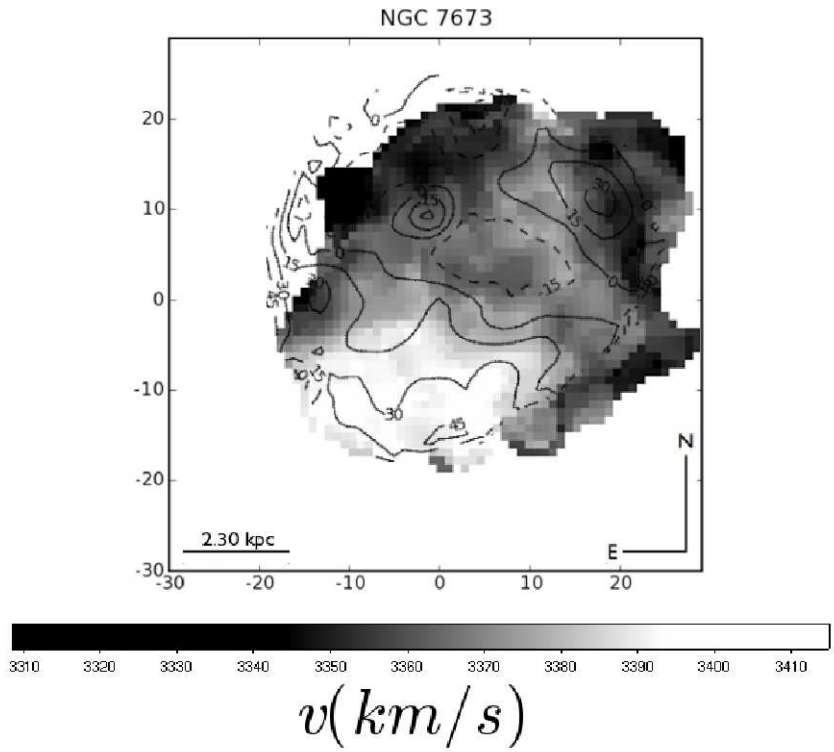

Figure 4-5. PPAK Hα velocity map contours overlaid on VLA neutral atomic hydrogen velocity map of NGC 7673. The combined B+C+D arrays were used for the VLA map. The size of the beam is 6". Both velocity maps are consistent within their respective uncertainties. The offset between both might be explained by the two plane-parallel disks as discussed in the text.

respectively) towards the west of the center of the FOV; these offsets are comparable to the size of one fiber. The geometric center was found as the average of the position of each fiber with signal from the galaxy; while the photometric center was found as the average position of each fiber with signal from the galaxy weighted by its integrated flux. Two additional elongated peaks in velocity width as large as the central one can be found to the northeast and northwest of the galaxy. The velocity width of the galaxy ranges from about 15 to 60 km s^{-1} within a FOV covered by fibers for which the S/N is at least 30.

As for the integrated velocity width HG99 found $W_{20} = 126$ km s^{-1} ($v_{rot} = 0.5W_{20}/\sin i$). This is slightly larger than the value found by Pisano et al. (2001), $W_{20} = 119$ km s^{-1} from Keck echelle spectroscopy. Furthermore, Pisano et al. (2001)

find the HII profile to be narrower than the HI profile (119 versus 164 km s^{-1}). We find W_{20} = 159 km s^{-1}, closer to Pisano et al. (2001). Differences with HG99 might be attributed to our larger FOV, which, on the other hand, is large enough to resemble that of the HI observations of Pisano et al. (2001).

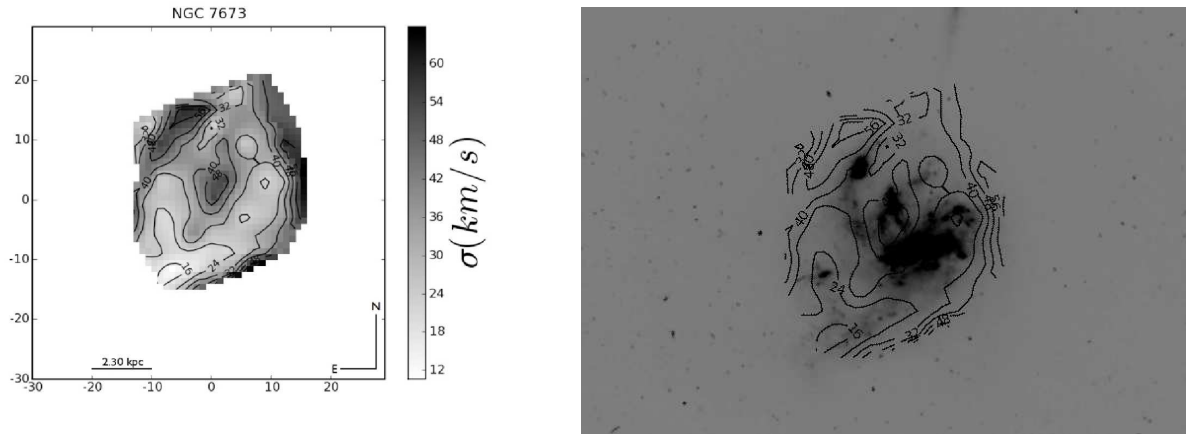

Figure 4-6. A) PPAK [OIII]λ5007 velocity width map of NGC 7673 using the V1200 configuration. The central peak roughly coincides with the luminosity-weighted center (photometric) and the center of the outer-isophotes (geometric) of the galaxy, and is assumed to be the dynamical center of the galaxy. Furthermore, the minor axis of the galaxy as derived from the velocity contours goes through this peak. B) PPAK Hα velocity width map contours overlaid on the F555W WFPC2 image of NGC 7673. North is to the top and East is to the left.

4.2.4 Discussion

4.2.4.1 Minor Merger Scenario

As stated above, two independent kinematic components are found in NGC 7673: a compact one with an optical counterpart (clump B); and an elongated one without one. The independent kinematic component found at the location of clump B is interesting not only because of its optical counterpart but because of further evidence for decoupling that we discuss below.

A first attempt to investigate the nature of clump B was made by calculating the [OIII]λ5007/Hβ and [NII]/Hα ratios for the entire galaxy, and this component in

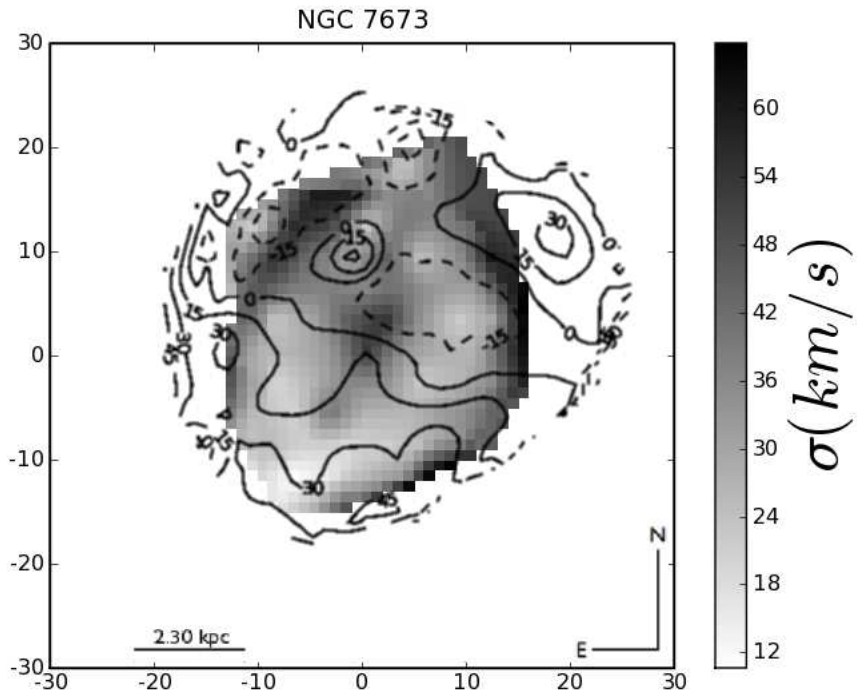

Figure 4-7. PPAK Hα velocity map contours overlaid on PPAK Velocity Width Map of NGC 7673.

particular, to study the possible presence of AGN activity. Nevertheless, these ratios, around 0.3 and -0.7 dex, respectively, are in agreement with those of an HII region (Osterbrock, 1989). Furthermore, the pressure derived for clump B from the [SII]/Hα ($\sim$0.4) and [NII]/Hα ($\sim$0.2) ratios is also in agreement with that of a starburst (Rickes et al., 2008). For clump B and the entire galaxy those ratios are considerably smaller than those found in LINERs, in agreement with those found in starburst galaxies, and only close to those found in Seyfert galaxies as shown in Figure 12 from Rickes et al. (2008).

As mentioned above, HG99 were able to fit the Hα emission lines of their integral field spectroscopy data with two Gaussian profiles throughout most of the galaxy. In particular, before HG99, Taniguchi & Tamura (1987) found two (one narrow, one broad) kinematic components at the location of clump B. Nevertheless, after simulating those by using their measurements in combination with our [OIII]λ5007 emission lines, spectral resolution, and

noise, only a marginal detection would have been possible. Thus, the possibility of finding a second broad component at the position of clump B by means of the analysis of the profiles of our emission lines was rejected.

Another possibility is that clump B peculiar kinematics are due to galactic winds and even though, as mentioned above, the quality of our data keeps us from establishing any final word about the nature of this region, a further qualitative analysis is possible based on the Hβ luminosity ($L_{\mathrm{H}\beta}$) measured by CM09a using

$Q = \frac{L_{\mathrm{H}\beta}}{h\nu_{\mathrm{H}\beta}} \frac{\alpha^{eff}_{\mathrm{H}\beta}}{\alpha_B}$

(Osterbrock, 1989), where Q is the number of photons harder than Lyα emitted by a star forming region, h is the Planck constant, $\nu_{\mathrm{H}\beta}$ is the frequency of Hβ, $\alpha^{eff}_{\mathrm{H}\beta}$ is the case B HI recombination coefficient for Hβ, and α_B is the recombination coefficient for H-like ions. Assuming then that all the stars in the star-forming region are O7 with a mass of 60 $M_\odot$ and a Salpeter Initial Mass Function (Salpeter, 1955) we find that 18,500 stars are responsible for the ionization of the gas. While this is an approximation the presence of Wolf-Rayet features in our spectra (CM09a) is consistent with massive stars. If all those stars were to explode as supernovae with an energy of 10^{51} erg, the total thermal energy released ($E = 1.85 \times 10^{55}$ erg), would be unequivocally smaller than the binding energy ($\Omega_G = 5.23 \times 10^{57}$ erg) as defined by (Yoshii & Arimoto, 1987). Galactic winds cannot be then responsible for the kinematic properties of the component associated with clump B. If we assume the total thermal energy released is transformed into kinematic energy, velocities up to 20 km s^{-1} are accounted for. Such a low value is in disagreement with the broad component of Taniguchi & Tamura (1987) and could not be detected with our spectral resolution.

On the other hand, as stated by HG99, both photometric and spectroscopic similarities between NGC 7673 and NGC 3310 (a well known system largely classified as a minor merger) in both HII and HI data leads to consider NGC 7673 as a candidate for a major starburst triggered by a minor merger. This minor merger with a dwarf

companion would account for the different bursts in the inner parts of the galaxy and the different morphological features, such as arcs, in its outer parts.

Metallicity and continuum (5600 – 5800 Å) measurements of CM09a show marginally higher metallicity values, and a secondary peak (second in intensity after the central one) at the location of clump B respectively. The metallicity values found by CM09a for clump B and its surroundings from [OIII]λ4363 are respectively 8.07 ± 0.06 dex and 7.76 ± 0.06 dex. These could be explained by the presence of an extremely giant HII region at the location of clump B within a lower metallicity environment. When we compare the metallicity and M_B of clump B with a sample of intermediate-redshift LCBGs from Hoyos et al. (2005, Figure 4-8) clump B, less luminous and slightly less metallic, falls closer to dwarf irregulars while NGC 7673 falls within the region occupied by intermediate-redshift LCBGs,

The Hβ luminosity and the velocity width of clump B follow the correlation found by Melnick et al. (1987) for nearby giant HII regions (Figure 4-9). Nevertheless, clump B is brighter and considerably more massive than any of the nearby giant HII regions within their sample. Knowing that this correlation holds from nearby HII regions and galaxies to the HII-like galaxies found at intermediate-, and high-redshift (Siegel, Guzmán, Pérez-Gallego, et al., 2005), suggests that an infalling dwarf galaxy, instead of a giant HII region at the location of clump B might be responsible for its peculiar behavior. If the minor merger scenario were to be confirmed, the elongated independent kinematic component cannot be disregarded as a possible side effect within the minor merger scenario.

Furthermore, CM09a measurements of the equivalent widths of the underlying population absorption spectral features (e.g., Hβ, Hγ) show a peculiarity at the location of clump B. While the strength of these features is noticeable throughout the galaxy, it is almost nonexistent at the location of clump B. The strength of the equivalent width of these features account for the age of the underlying population. Strong lines are mainly

due to a population of A class stars and correspond to systems a few hundred thousand years old. Weaker lines are typical of either younger or older populations. Nonetheless, clump B shows signs of decoupling or differentiation, at the least marginally, with respect to its environment from the point of view of both the gas and the stars.

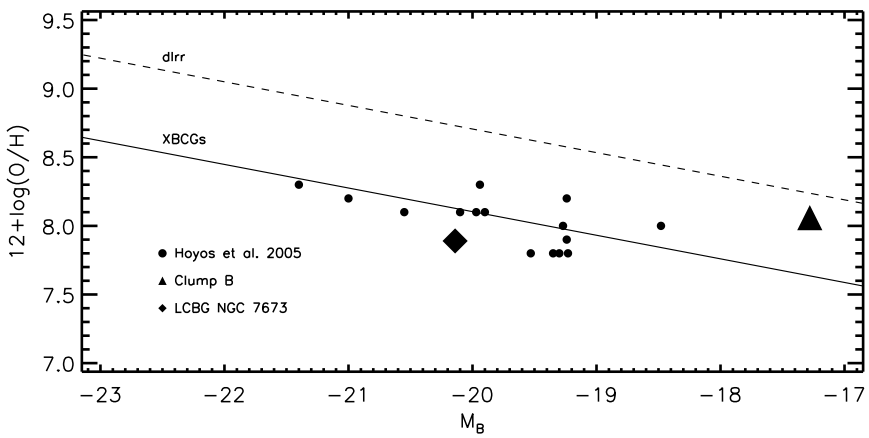

Figure 4-8. 12 + log (O/H) vs. M_B for a sample of intermediate-redshift LCBGs. Dots are from Hoyos et al. (2005). The position of NGC 7673 and clump B are also shown as measured by CM09a. The dashed line represents the luminosity-metallicity relation for local dIrr (Richer & McCall, 1995). The solid line represents this relation for extremely metal-poor BCGs (Kunth & Östlin, 2000). The uncertainties of our metallicity and luminosity measurements are smaller than our symbols.

4.2.4.2 Mass

Galactic kinematics play an important role on the measurement of masses of nearby and distant galaxies. Galaxies' masses are related to their kinematics via the Virial Theorem. Nevertheless, we need to be careful when making the assumption that an object is virialized. By studying NGC 7673, among other examples of local counterparts of the distant starburst population, we can learn whether or not most of these objects are virialized and how careful we need to be when inferring their masses from their kinematics.

If we assume for NGC 7673 a peak to peak velocity range as suggested by the rotation curve derived above (∼60 km s^{-1}), the inferred rotational velocity $v_{rot} = \sqrt{\frac{M_{dyn}G}{R_e}}$ translates into a dynamical mass within the R_e measured by Pisano et al. (2001) of

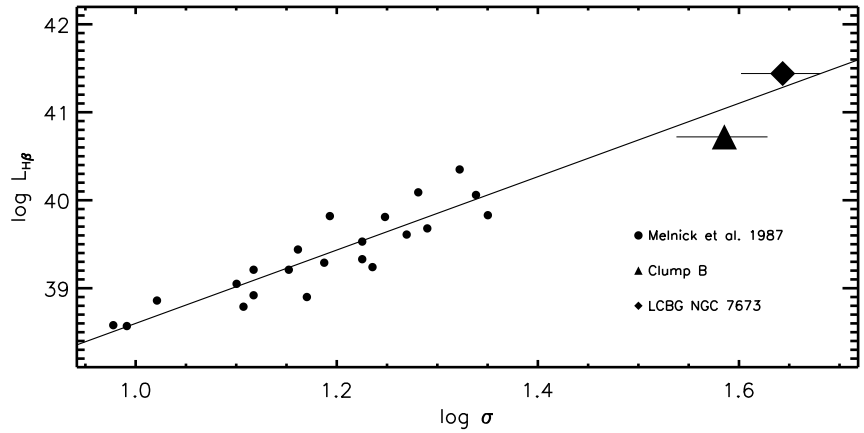

Figure 4-9. $L_{\mathrm{H}\beta}$ vs. σ for a sample of giant HII regions. Dots are from Melnick et al. (1987). The position of NGC 7673 and clump B are also shown as measured by this work (σ) and CM09a ($L_{H\beta}$). The solid line represents the correlation between these parameters. This correlation holds from giant HII regions to similar starburst galaxies observed at high redshift (Siegel, Guzmán, Pérez-Gallego, et al., 2005). The uncertainties of our luminosity measurements are smaller than our symbols.

around 8.0×10^8 $M_\odot$ ($R_e = 1.9$ kpc). Pisano et al. (2001) inferred a dynamical mass of 2.5×10^{10} $M_\odot$ within R_{HI} ($R_{\mathrm{HI}} = 8.3$ kpc $\sim 4.5 \times R_e$) from their W_{20} measurements. In both cases an inclination of 45° is assumed.

On the other hand, considering the K magnitude of NGC 7673 and the mass luminosity relation $M/L_K = 0.51$ for BCDs from Pérez-González et al. (2003) we derive a stellar mass of 1.5×10^{10} $M_\odot$. A total mass of 1.9×10^{10} $M_\odot$ is then calculated by adding the mass of the neutral hydrogen estimated by Pisano et al. (2001). If the system is to be virialized the resulting rotational velocity would be $v_{rot} = 133$ km s^{-1}. In order for the rotation curve derived for a PA equal to 168° to agree with this v_{rot} the inclination of the galaxy must be close to 15°, which on the other hand is not unreasonable when one takes a look at the optical image of the galaxy.

From our integrated PPAK data we find $W_{20} = 159 \pm 4$ km s^{-1}. If an inclination equal to 15° is also to be considered the rotational velocity would rise to $v_{rot} = 290$ km s^{-1}.

As it is, neither the peak to peak velocity range shown by the optical data nor the one shown by the radio data, accounts for such a large v_{rot} even though the entire FOV

of NCG 7673 is covered in both cases. This suggests that W_{20} and, therefore, FWHM and σ, are not good indicators of the rotational velocities and subsequent dynamical mass of starburst galaxies like NGC 7673, and mostly accounts for the presence of kinematically decoupled components and asymmetries alike, and their position within the galaxy.

4.3 NGC 7714

NGC 7714 (also known as MRK 538) is a nearby ($z = 0.009333$) Sb peculiar galaxy (de Vaucouleurs et al., 1991) labeled as a prototypical starburst galaxy by Weedman et al. (1981). It shows a bulge and a distorted disk, a bar and spiral arms and, at least, three major clumps of star formation (Figure 4-10). Fluxes at different wavelengths, from X-ray to radio, are explained as a consequence of an intense star formation activity centered on its nucleus. In particular, Weedman et al. (1981) explained the X-ray and radio luminosities with 10^4 supernova remnants. As for its optical continuum and far-IR colors, Bernloehr (1993) found that the star formation in NCG 7714 is consistent with a continuous SFR during the past 20 Myr, which had probably been triggered by the interaction with the companion galaxy NGC 7715 (Smith et al., 1997), found 2 arcmin (i.e., ∼22 kpc, at the redshift of the galaxies) away from the nucleus of NGC 7714. From PPAK Hα fluxes Castillo-Morales, Gallego, Pérez-Gallego, et al. (2009b, hereafter CM09b) derived a star formation rate of $10.6 \pm 0.8\ M_\odot\ \mathrm{yr}^{-1}$.

Very detailed studies have been carried out in the optical and near-IR part of the spectrum to characterize the gas properties in the nuclear and circumnuclear regions of NGC 7714 (González-Delgado et al., 1995; González Delgado et al., 1999). These studies concluded that the nuclear burst of star formation should have an age around 4–5 Myr, taking into account the detection of a Wolf-Rayet bump, and noticed the presence of a previous burst of star formation in view of the detection of the calcium absorption triplet at 8600 Å. Models by Garcia-Vargas et al. (1997) indicate that a young burst 3–5 Myr old would be able to explain the emission line spectrum and Wolf-Rayet bump detection in three circumnuclear HII regions of NGC 7714. Lançon et al. (2001) found, using

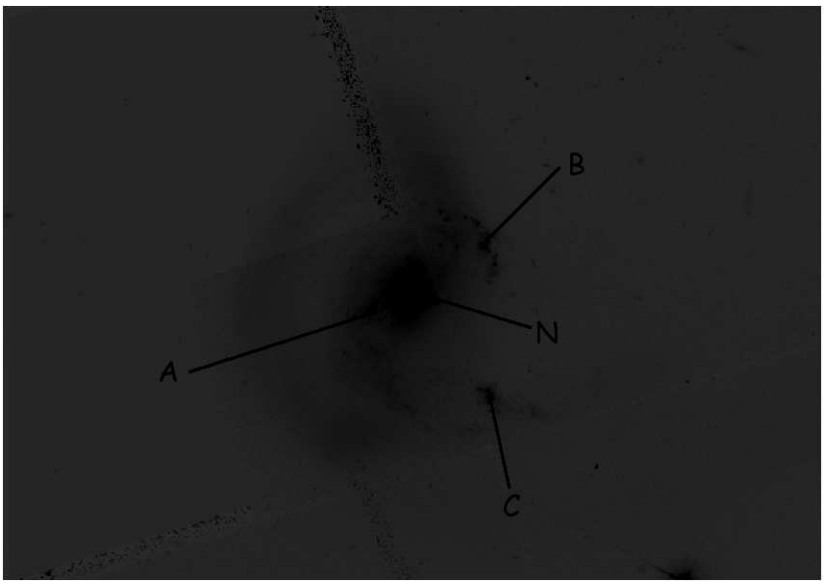

Figure 4-10. F814W WFPC2 image of NGC 7714 labeled with the nucleus and three star-forming clumps used by González-Delgado et al. (1995). North is to the top and East is to the left. North is to the top and East is to the left. We had to combine two F814W WFPC2 images of NGC 7714 in order to cover the full FOV of PPAK, since each of those covered only half of the galaxy.

population synthesis models, that the starburst is responsible for only a small portion of an extended star formation episode, triggered approximately 10^8 yr ago.

HI 21 cm line mapping by Smith et al. (1997) showed an extended HI emission around NGC 7714, forming a bridge that spreads out towards its eastern companion. Deviations from circular motion are found in the outer regions of the galaxy disk, while the inner regions show a smooth gradient for a rotating disk. In the same study, NGC 7715 was also found to exhibit signs of rotation. This pair of galaxies, known as Arp 284 (Arp, 1966), is one of the prototypical collisional starburst systems known. Numerical models and the observed stellar and gas morphologies suggest a recent collision, between 100–200 Myr ago (Struck & Smith, 2003). Multiwavelength data, summarized in Smith et al. (1997), reveal young, intermediate-age, and old stellar populations in NGC 7714. Its high surface brightness, strong emission lines and blue colors make of NGC 7714 a prototypical LCBG (Table 4-1). Furthermore, its apparent size makes it a suitable candidate for our analysis.

PPAK observations of NGC 7714 were made during the nights of 2005 August 10, 11, 12, and 14 using two different setups as discussed in Chapter 2 (Table 4-4).

Table 4-3. NGC 7714 Observational Properties

Name	z[a]	$M(B)$[b] (mag)	SB_e[b] (mag arcsec^2)	$B-V$[b] (mag)	R_e[b] (kpc)
NGC 7714	0.009333[c]	-20.10	20.00	0.40	2.70
LCBGs[c]	0.0189 ± 0.0019	-19.70 ± 0.20	20.30 ± 0.20	0.40 ± 0.02	2.16 ± 0.25

[a] Huchra et al. (1999); [b] (Garland et al., 2005)
[c] This gives a scale of 0.189 kpc arcsec^{-1}
[d] Mean and standard deviation of our sample

Table 4-4. NGC 7714 Observing Log

Configuration	Dithering	Night	Exposure Time (s)	Offset (arcsec)
V300[b]	1	10 August 2005	3×330	(0.00, 0.00)[a]
V300	2	14 August 2005	3×330	(+1.56, +0.78)
V300	3	14 August 2005	3×330	(+1.56, −0.78)
V1200[c]	1	11 August 2005	3×900	(0.00, 0.00)[a]
V1200	2	11 August 2005	3×900	(+1.56, +0.78)
V1200	3	12 August 2005	3×900	(+1.56, −0.78)

[a] The original pointing of the telescope is 23:36:14.1 +02:09:19
[b] The V300 configuration was centered at 5361 Å covering the spectral range between 3591 and 6996 Å
[c] The V1200 configuration was centered at 5040 Å covering the spectral range between 4669 and 5395 Å

4.3.1 Velocity Map

The velocity map of NGC 7714 can be seen in Figure 4-11. Being the galaxy in our sample with the largest apparent size, $r_e = 14.3$ arcsec (i.e., $r_e = 2.7$ kpc, at the redshift of the galaxy), measurements of the velocity down to our S/N limit were possible for a region extending over 40 arcsec in diameter. Further away, the S/N was not high enough to proceed to the measurement of the velocity. Neither border nor pixelization effects due to the interpolation process were considered in the analysis. These manifest as either a steep increase or steep decrease of the velocity towards the edges of the available data.

Nevertheless, it is important to notice that the steep increase towards the southeast of the FOV of the galaxy is real.

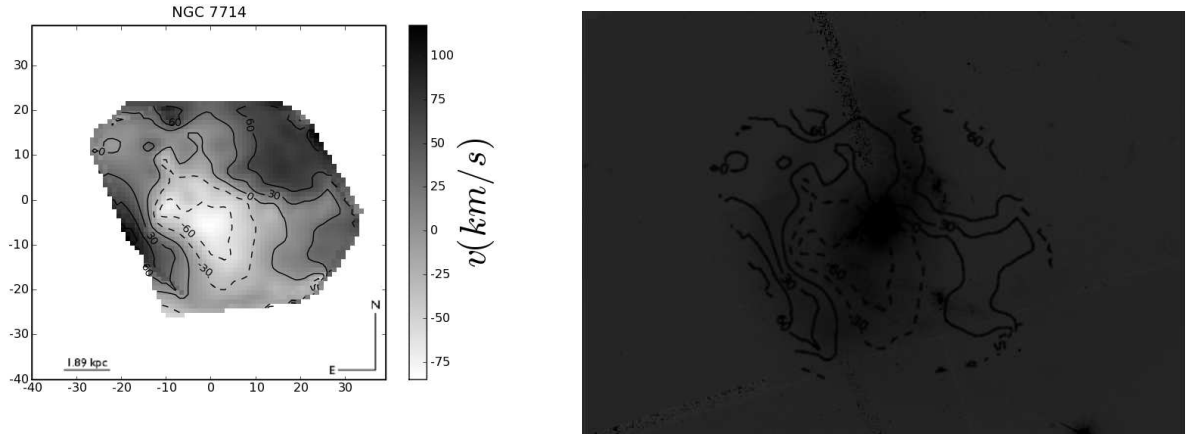

A B

Figure 4-11. A) PPAK Hα velocity map of NGC 7714 using the low resolution V300 configuration. B) PPAK Hα velocity map contours overlaid on the F814W WFPC2 image of NGC 7714.

The velocity map shows a mostly symmetric velocity gradient that ranges from approximately -80 to 80 km s^{-1}. The velocities shown in the map are referenced to the redshift of the central peak velocity width of the galaxy (Section 4.3.2), which roughly (within one sigma) coincides with the one available in the NASA Extragalactic Database ($z = 0.009333$).

The existence of a rather straight velocity contour that crosses the nucleus of the galaxy from the northeast to the southwest through a central velocity width peak suggests that it actually traces the position of the minor axis of the galaxy, yielding a major axis PA equal to 135°. A rotation curve can be derived for this PA by reading the measured velocities along the corresponding major axis (Figure 4-12). A PA equal to 135° provides a smooth rotation curve from which a rotation velocity of about 75 km s^{-1} uncorrected by inclination can be inferred. The data corresponding to measurements of the velocities of the spiral arc of the galaxy were left out of this analysis. González-Delgado et al. (1995) found a similar gradient for a PA of 110°.

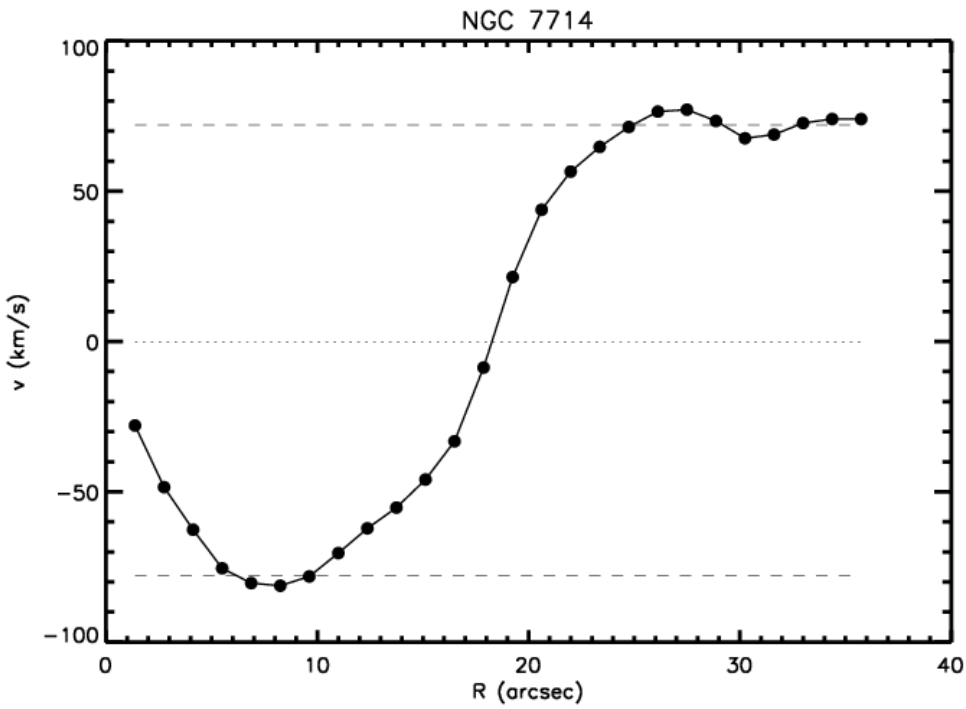

Figure 4-12. Rotation curve along the major axis of NGC 7714 for a PA equal to 135°. The dashed lines indicate the plateaus, while the dotted line indicate the velocity of the central velocity width peak, which is taken as a reference.

The northwestern half of the galaxy (darker) is consistently moving away from the observer, while the southestern half (lighter) is moving towards with the exception of an elongated region, about 4 kpc long, about 20 arcsec southeast of the center of the FOV. This region is moving away from the observer up to at about 60 km s^{-1} with respect to its surroundings, in good agreement with the overall velocity behavior of the northeastern half of the galaxy. We discuss below whether this kinematically decoupled component show physical properties that differ from the rest of the galaxy.

When compared to the F814W WFPC2 image of NGC 7714 (Figure 4-11) two characteristics stand out: (i) the velocity field follows rather well the distorted disk of the galaxy; and (ii) the decoupled region appears to be linked to the spiral arm of the galaxy.

4.3.2 Velocity Width Map

The velocity width map of the galaxy is shown in Figures 4-13 and 4-14 and can be used in combination with the velocity map to better understand the kinematic properties of NGC 7714.

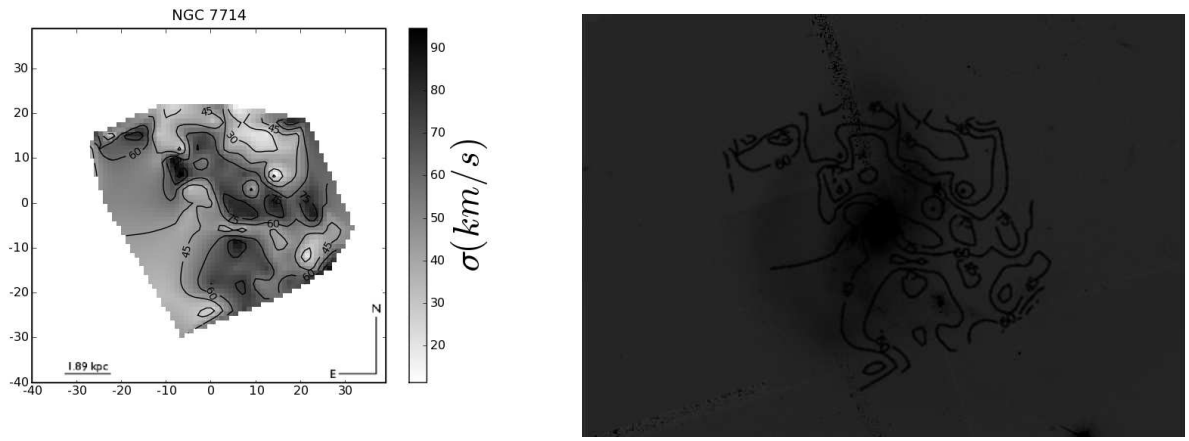

A B

Figure 4-13. A) PPAK [OIII]λ5007 velocity width map of NGC 7714 using the V1200 configuration. B) PPAK Hα velocity width map contours overlaid on the DSS image of NGC 7714. North is to the top and East is to the left.

The velocity width map of NGC 7714 shows a peak ($\sigma = 81 \pm 2$ km s^{-1}) about 6 arcsec (1.1 kpc) west off the center of the FOV, which is located about 7 arcsec (1.3 kpc) southeast from the nucleus of the galaxy (Figure 4-13). This peak is in agreement with the measured velocity gradient along the disk of the galaxy (Figure 4-14). The luminosity-weighted center (photometric) and the center of the outer-isophotes (geometric) of the galaxy are located respectively about 4 arcsec (760 pc) northwest, and 3 arcsec (570 pc) west from the center of the FOV. Several other peaks are found within the FOV. These can be explained by the presence of spectrally resolved components in up to 6% of the total area of the galaxy. The velocity width of the galaxy ranges from about 15 to 90 km s^{-1} within a FOV covered by fibers for which S/N is at least 30.

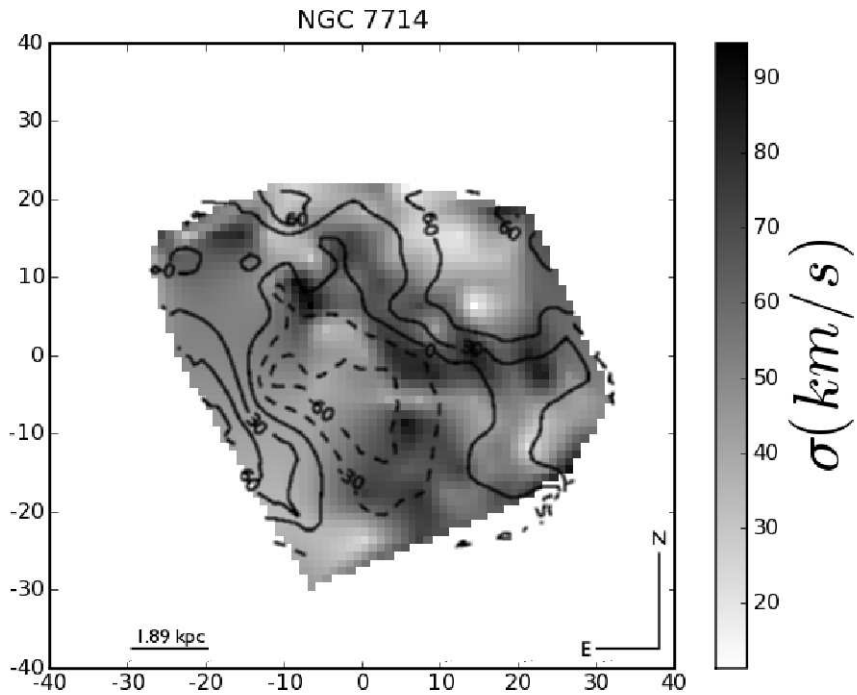

Figure 4-14. PPAK Hα velocity map contours overlaid on PPAK Velocity Width Map of NGC 7714.

4.3.3 Discussion

Spiral Arm. As stated above, an independent kinematic component is found in NGC 7714 moving at an average velocity of about 60 km s^{-1}. This elongated component is located at the position of the western spiral arm of the galaxy and moving at a positive velocity which is in good agreement with the overall velocity of the opposite side of the galaxy. On the other hand, the average metallicity along the spiral arm, $12 + \log(\mathrm{O/H}) = 8.55 \pm 0.25$ is in better agreement with the overall metallicity of the blue half of the galaxy instead, higher than the one found on the red half moving at the velocity of the spiral arm (Castillo-Morales, Gallego, Pérez-Gallego, et al., 2009b).

Mass. If we assume for NGC 7714 a peak to peak velocity range as suggested by the velocity map derived above (∼200 km s^{-1}), the inferred rotational velocity $v_{rot} = \sqrt{\frac{M_{dyn}G}{R_e}} = 98$ km s^{-1} translates into a dynamical mass within $R_e = 2.7$ kpc of around

1.0×10^{10} $M_\odot$. An inclination of 50° was assumed (Garland et al., 2004). For this galaxy Garland et al. (2004) found, from their HI study, $M_{\rm HI} = 7.6 \times 10^9$ $M_\odot$, and $M_{dyn}(R_e) = 1.1 \times 10^{10}$ $M_\odot$. Garland et al. (2004) estimate the random errors associated with the dynamical mass to be approximately 50%.

From our integrated PPAK data we find $W_{20} = 272 \pm 6$ km s^{-1}. If an inclination equal to 50° is also to be considered a rotational velocity $v_{rot} = 177$ km s^{-1} can be derived, which would translate into a mass about four times larger than the one derived from the peak to peak analysis.

4.4 NGC 6052

NGC 6052 (also known as MRK 297) is a nearby ($z = 0.015808$) archetypal clumpy irregular galaxy (Figure 4-15; e.g., Heidmann, 1987) included in the Atlas of Peculiar Galaxies (Arp, 1966). Color maps of NGC 6052 indicate star formation is occurring in numerous regions spread over nearly the entire system, and the presence of a large-scale, inhomogeneous absorption pattern (Papaderos et al., 1998). Meanwhile, the Hα emission is clumpy and suggestive of outflows, with loops, tendrils, and numerous filaments (Cairós et al., 2001; Martínez-Delgado et al., 2009). Martínez-Delgado et al. (2009) cataloged a total of 30 star formation knots. From PPAK Hα fluxes CM09b derived a star formation rate as high ast 25.2 ± 1.9 $M_\odot$ yr^{-1}. On the other hand, infrared studies (e.g., Metcalfe et al., 2005; Whelan et al., 2007) have labeled NGC 6052 as a Luminous Infrared Galaxy (LIRG) with a total IR luminosity of 1.0×10^{11} $L_\odot$. NGC 6052 belongs to the SDSS catalog.

One remarkable feature of NGC 6052 is the double tail in the east side of the galaxy, extending out in the north-south direction. This galaxy has been interpreted as the result of a collision between two late-type spiral galaxies for which Alloin & Duflot (1979) identified two peaks in the continuum frames as two compact cores embedded in a common envelope. It has also been interpreted as the result of a collision between a spiral and an irregular (Burenkov, 1988), which induced star formation throughout the

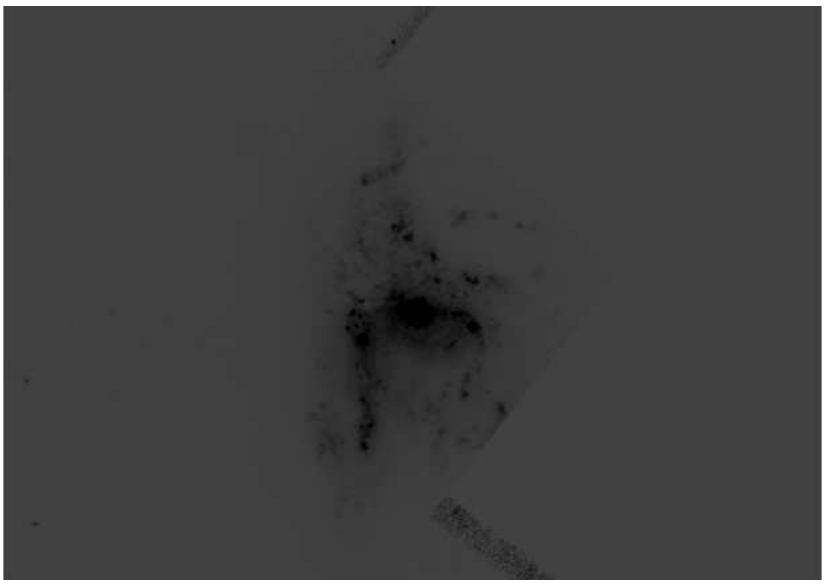

Figure 4-15. F555W WFPC2 image of NGC 6052. North is to the top and East is to the left.

galaxy. Taniguchi & Noguchi (1991) found, using numerical N-body simulations, that the optical morphological properties of NGC 6052 can be explained as the result of a coplanar radial penetration collision between two disk galaxies. They suggest that in this collision, the target galaxy was deformed into the north-south "wing" by the face-on intruder galaxy. The HI map of Garland et al. (2007) shows a tidal tail that is much more extended and lopsided than the optical wing to which Taniguchi & Noguchi (1991) matched their simulation. The HI observations of Garland et al. (2007) do not appear to support the coplanar radial penetration model. NGC 6052 may be in a later stage of merging than suggested by this model.

HI 21 cm line mapping by Garland et al. (2007) show a disturbed, asymmetric distribution of HI in NGC 6052, with a north-south elongation. A slight extension is also visible in the optical image. The HI velocity field of NGC 6052 derived by Garland et al. (2007) shows a velocity gradient across the main part of the galaxy, but the north-south extension is at a nearly constant higher velocity. The measured HI mass, $6.3 \times 10^9\ M_\odot$, is 90% of that measured with the GBT Garland et al. (2007). They did not expect any contamination, as NGC 6052 has no known companions.

Among our sample of nearby LCBGs, NGC 6052 is a prototypical major merger (Table 4-5), plus it has one of the highest infrared luminosity, dynamical mass, molecular gas mass, and ratio of molecular to atomic gas mass (Garland et al., 2004, 2005, 2007). Its suggested merger state may explain these observations. Close interactions like the one Garland et al. (2007) inferred could trigger quick conversion of atomic to molecular gas, resulting in a bright starburst, centrally concentrated CO, and a disturbed HI component, as in ultra-luminous infrared galaxies (Solomon & Sage, 1988).

PPAK observations of NGC 6052 were made during the nights of 2005 August 9, 11, 12, and 14 using two different setups as discussed in Chapter 2 (Table 4-4).

Table 4-5. NGC 6052 Observational Properties

Name	z[a]	$M(B)$[a] (mag)	SB_e[a] (mag arcsec^2)	$B-V$[a] (mag)	R_e[a] (kpc)
NGC 6052	0.015808[b]	-20.69	19.71	0.41	2.42
LCBGs[c]	0.0189 ± 0.0019	-19.70 ± 0.20	20.30 ± 0.20	0.40 ± 0.02	2.16 ± 0.25

[a] SDSS Catalog
[b] This gives a scale of 0.318 kpc arcsec^{-1}
[c] Mean and standard deviation of our sample

Table 4-6. NGC 6052 Observing Log

Configuration	Dithering	Night	Exposure Time (s)	Offset (arcsec)
V300[b]	1	9 August 2005	3×330	(0.00, 0.00)[a]
V300	2	9 August 2005	3×330	(+1.56, +0.78)
V300	3	14 August 2005	3×330	(+1.56, −0.78)
V1200[c]	1	11 August 2005	3×900	(0.00, 0.00)[a]
V1200	2	11 August 2005	3×900	(+1.56, +0.78)
V1200	3	12 August 2005	3×900	(+1.56, −0.78)

[a] The original pointing of the telescope is 16:05:12.9 +20:32:32
[b] The V300 configuration was centered at 5361 Å covering the spectral range between 3591 and 6996 Å
[c] The V1200 configuration was centered at 5040 Å covering the spectral range between 4669 and 5395 Å

4.4.1 Velocity Map

The velocity map of NGC 6052 can be seen in Figure 4-16. Measurements of the velocity down to our S/N limit were possible for a region extending over 40 arcsec in diameter. The apparent effective radius of NGC 6052 is $r_e = 7.6$ arcsec (i.e., $r_e = 2.4$ kpc, at the redshift of the galaxy). Further away, the S/N was not high enough to proceed to the measurement of the velocity.

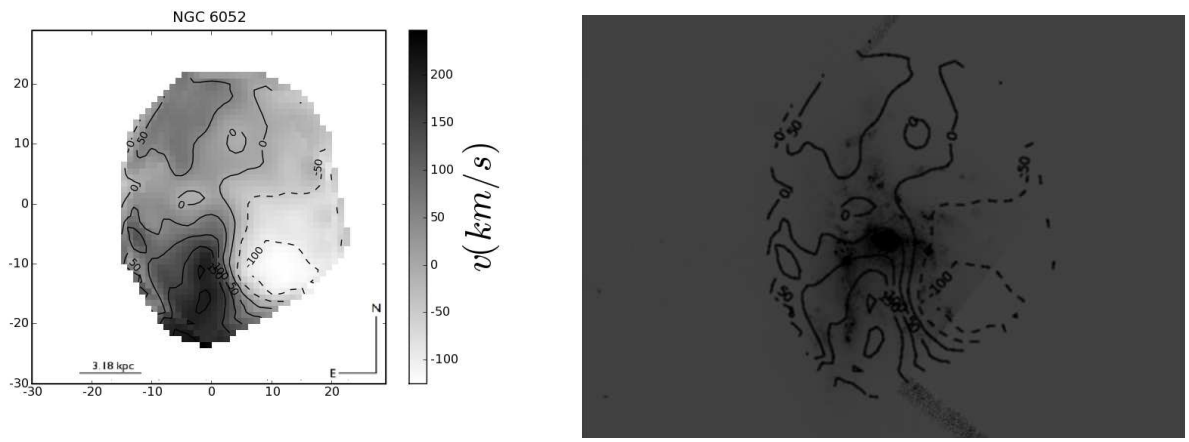

A B

Figure 4-16. A) PPAK Hα velocity map of NGC 6052 using the low resolution V300 configuration. B) PPAK Hα velocity map contours overlaid on the F555W WFPC2 image of NGC 6052.

The velocity map shows two differentiated behaviors. First, a symmetric velocity gradient that ranges over 200 km s^{-1} in velocity from east to west can be seen towards the southern half of the galaxy. Second, a rather constant field can be seen towards the northern half of the galaxy. The velocities shown in the map are referenced to the redshift of the peak velocity width of the galaxy (Section 4.4.2) which roughly coincides with the one available in the NASA Extragalactic Database ($z = 0.015808$).

The existence of a rather straight velocity contour that crosses the nucleus of the galaxy from north to south through a high central velocity width peak suggests that it actually traces the position of the minor axis of the galaxy, yielding a major axis PA equal to 120°. A rotation curve can be derived for the PA we derive by reading the measured

velocities along the corresponding major axis (Figure 4-17). A PA equal to 120° provides a smooth rotation curve from which an uncorrected by inclination rotation velocity of about 75 km s^{-1} can be inferred. The velocity gradient and overall aspect of the velocity map is in agreement which that of García-Lorenzo et al. (2008), who covered a smaller region of the galaxy using the fiber system INTEGRAL attached to the William Herschel Telescope.

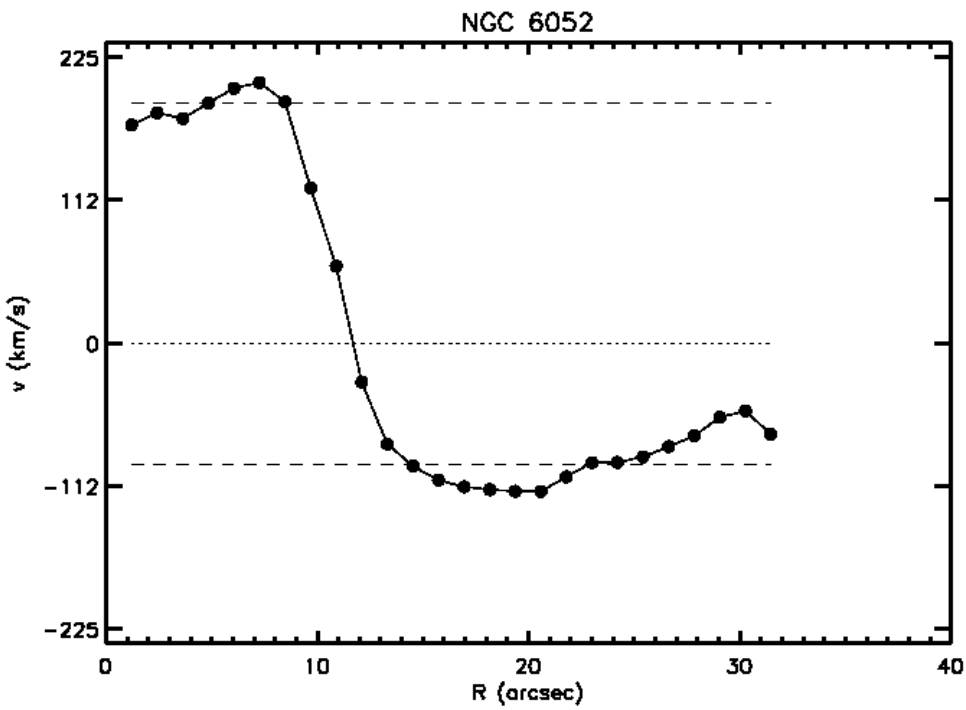

Figure 4-17. Rotation curves along the major axis of NGC 6052 for PA equal to 120°. The dashed lines indicate the plateaus, while the dotted line indicate the velocity of the central velocity width peak, which is taken as a reference.

The north half of the galaxy is consistent with a rather face-on galaxy, while the south half of the galaxy is consistent with a rotating disk with an inclination of at least 45°.

When compared to the F555W WFPC2 image of NGC 6052 (Figure 4-16) one characteristic stands out: the velocity gradient is located underneath and to the right of a morphological structure that bends together forming a right angle.

4.4.2 Velocity Width Map

Figures 4-18 and 4-19 show the velocity width map of the galaxy NGC 6052 as derived from our high resolution PPAK observations.

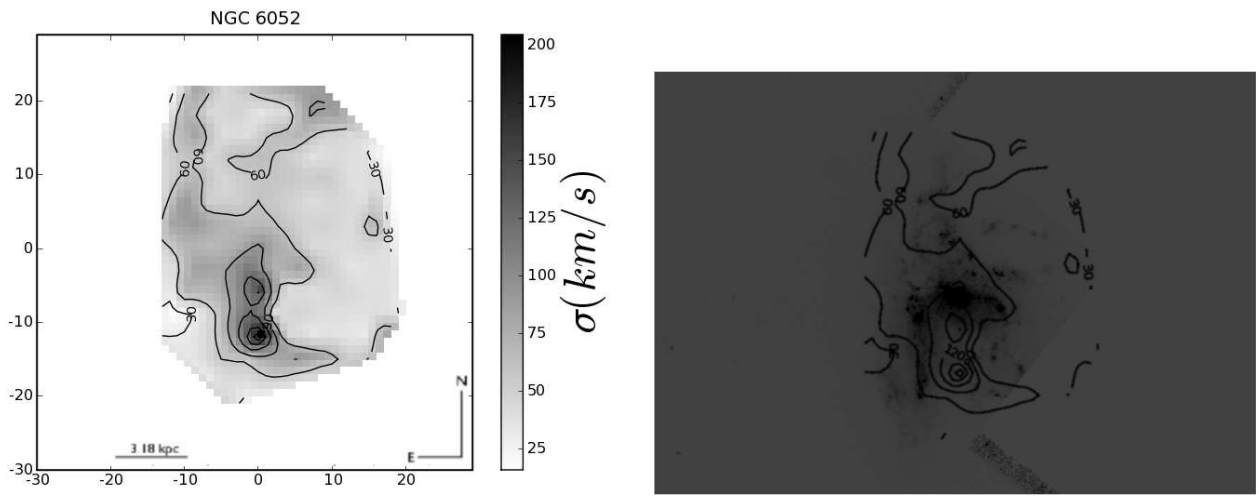

Figure 4-18. A) PPAK [OIII]λ5007 velocity width map of NGC 6052 using the V1200 configuration. B) PPAK Hα velocity width map contours overlaid on the F555W WFPC2 image of NGC 6052. North is to the top and East is to the left.

The velocity width map of NGC 6052 shows a high velocity width elongated region ($\sigma \sim 150$ km s^{-1}) south from the center of the FOV (Figure 4-18). This region is in agreement with the measured velocity gradient along the disk of the galaxy (Figure 4-19). These widths are the result of two well defined spectrally resolved components throughout the entire region. The velocity width of the galaxy ranges from about 25 to 200 km s^{-1} within a FOV covered by fibers for which S/N is at least 30.

4.4.3 Discussion

Merger Scenario. As stated above a sharp velocity gradient from east to west is visible in the southern half of the velocity map. Furthermore a high velocity width elongated region, whose width is the result of two well defined spectrally resolved components, crosses perpendicularly this gradient. The average distance between these

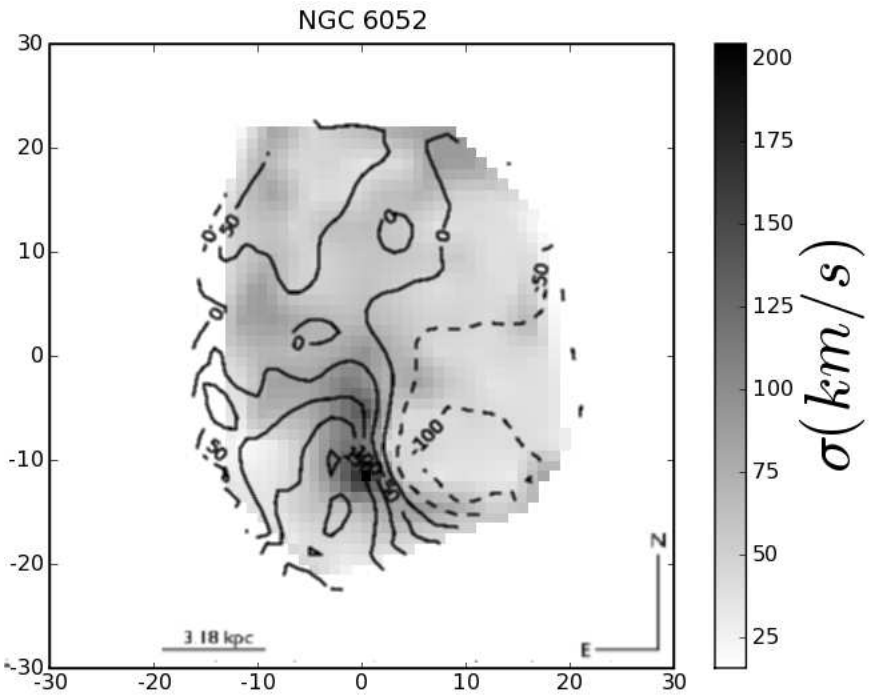

Figure 4-19. PPAK Hα velocity map contours overlaid on PPAK Velocity Width Map of NGC 6052.

components is about 3 Å (i.e., ∼175 km s^{-1}, at the redshift of the galaxy). The average intensity ratio between this components is about 2:1.

In Figure 4-20 we show the velocity map of NGC 6052 according to the following criteria. First, we show a velocity map by using, for every single spatial resolution element, the component whose velocity is similar to those measured for its surroundings. Second, we show a velocity map by using those components opposite to the ones before. The first map shows a steeper velocity gradient along the north-south direction, in agreement with the HI elongation (Figure 4-21). On the other hand, the second map shows a very distorted velocity gradient where spatially resolved kinematic components can be found. Notice that these components are not found in every single resolution element that samples the high velocity width region. Because of this, the map shows a clumpy structure. Nevertheless, the bluer (lighter) velocities measured in the red (darker) region are in agreement with the velocities measured throughout the western half of the galaxy.

This behavior, together with the HI observations, suggests that both spectrally resolved components might belong to different extended objects moving at different velocities from the observer.

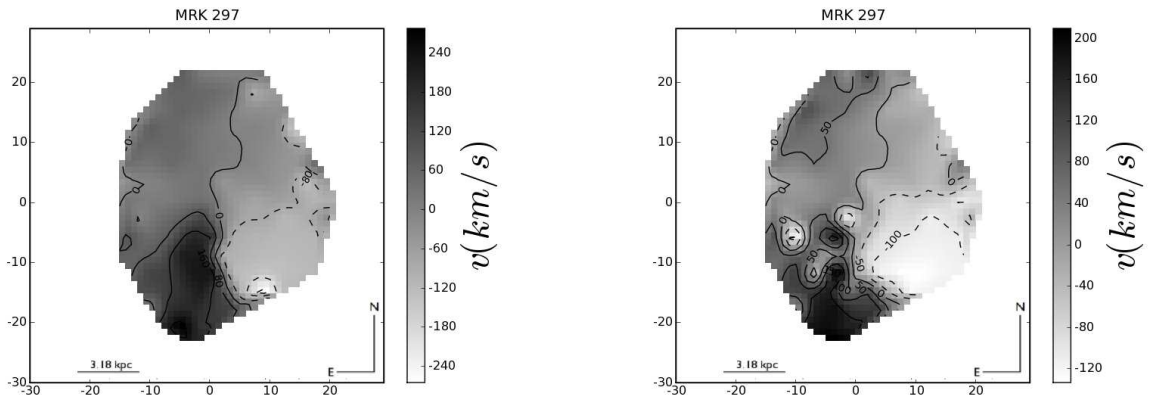

A B

Figure 4-20. A) PPAK Hα velocity map of NGC 6052. When possible, two spectrally resolved kinematic components were measured. In that case the one with a measured velocity in better agreement with its surroundings was used. B) PPAK Hα velocity map of NGC 6052. When possible, two spectrally resolved kinematic components were measured. In that case the one with a measured velocity in worst agreement with its surroundings was used.

With all this in mind, the velocity field may be the result of the superposition of two colliding systems, one in the background, and a second one close to edge-on in the foreground; and the observed east-west velocity gradient might just be due to a projection effect. The overlap is obvious in Figure 4-20B, where blue components can be seen where the edge-on foreground galaxy would be according to the HI observations from Garland et al. (2007). Therefore, our kinematic results corroborate the interaction scenario proposed in previous works (Alloin & Duflot, 1979; Taniguchi & Noguchi, 1991; Garland et al., 2007). In particular, Figure 1 of Garland et al. (2007), enforces this scenario because of the north-south elongation, the overall north-south velocity gradient, and the rather constant velocity throughout the western half of the galaxy (Figure 4-21). In summary, the double nucleus, the tail, the recent star formation, the large velocity gradients in the

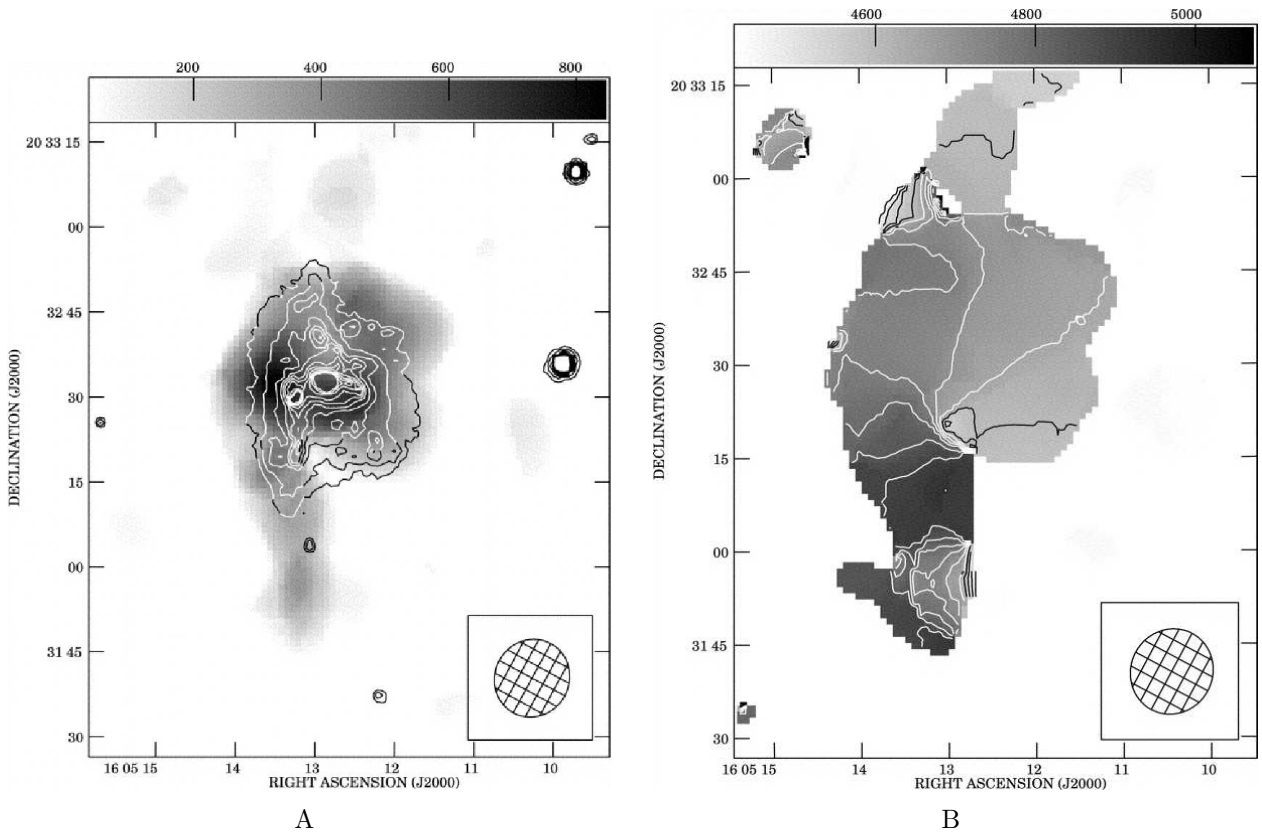

Figure 4-21. A) SDSS optical image (contours) overlaid on a gray-scale map of the HI intensity. The bar indicates the gray-scale range in units of Jy beam^{-1} m s^{-1}; only HI intensities above the 3-σ level, 45 Jy beam^{-1} m s^{-1}, are plotted. The beam for the HI map is shown in the bottom right corner. The optical contours are arbitrary. B) HI velocity field. The bar indicates the gray-scale range, 44315069 km s^{-1}. The contours are at 50 km s^{-1} intervals. The beam is shown in the bottom right corner.

extranuclear regions, and the perturbed gas in the whole FOV are all signs of a merger event.

Alternatively, Castillo-Morales, Gallego, Pérez-Gallego, et al. (2009b) finds for the different components in the high velocity width region, [OIII]λ5007/Hβ and [NII]λ6584/Hα ratios that differ noticeable from one component to the other. The bluer component ratios tend to be $\sim$40% higher. However, when combined to estimate their metallicity by means of the $O3N2$ indicator (Pettini & Pagel, 2004), both components are in agreement within the errors of the Pettini & Pagel (2004) calibration (0.25 dex at

the 95% confidence level; $12 + \log(\mathrm{O/H}) = 8.34$ and 8.36), which would indicate that if two merging galaxies are what we are seeing, they are equally metallic. Note that, while metallicity is proportional to the ratio [NII]λ6584/Hα, it is inversely proportional to the ratio [OIII]λ5007/Hβ.

4.5 NGC 469

NGC 469 is a nearby ($z = 0.013673$) lenticular galaxy that has not been widely studied in the past (Figure 4-22; Garland et al., 2004, 2005). This particular galaxy is a good example of the most compact galaxies in our sample (Table 4-7). Lenticular galaxies are disc galaxies which have used up or lost most of their interstellar matter and therefore have very little ongoing star formation. From PPAK Hα fluxes CM09b derived a star formation rate of just 1.3 ± 0.1 $M_\odot$ yr^{-1}. NGC 469 belongs to the SDSS catalog.

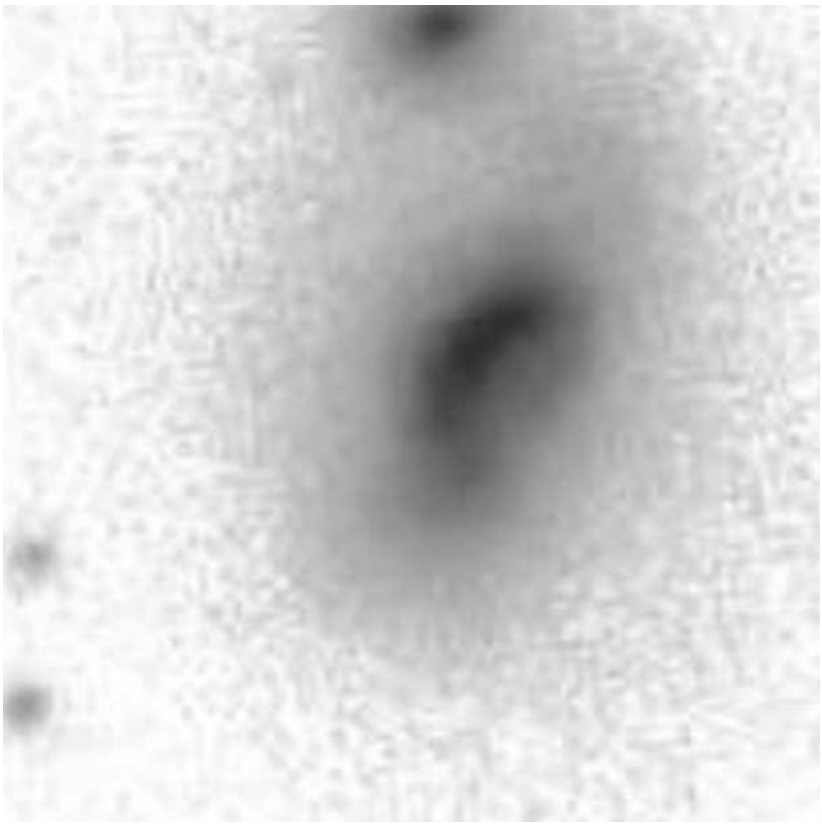

Figure 4-22. SDSS image of NGC 469. North is to the top and East is to the left.

PPAK observations of NGC 469 were made during the nights of 2005 August 12, 13, and 14 using two different setups as discussed in Chapter 2 (Table 4-8).

Table 4-7. NGC 469 Observational Properties

Name	z[a]	$M(B)$[a] (mag)	SB_e[a] (mag arcsec^2)	$B-V$[a] (mag)	R_e[a] (kpc)
NGC 469	0.013673[b]	-19.13	20.05	0.42	1.30
LCBGs[c]	0.0189 ± 0.0019	-19.70 ± 0.20	20.30 ± 0.20	0.40 ± 0.02	2.16 ± 0.25

[a] SDSS Catalog
[b] This gives a scale of 0.275 kpc arcsec^{-1}
[c] Mean and standard deviation of our sample

Table 4-8. NGC 469 Observing Log

Configuration	Dithering	Night	Exposure Time (s)	Offset (arcsec)
V300[b]	1	14 August 2005	3×330	(0.00, 0.00)[a]
V300	2	14 August 2005	3×330	(+1.56, +0.78)
V300	3	14 August 2005	3×330	(+1.56, −0.78)
V1200[c]	1	12 August 2005	3×900	(0.00, 0.00)[a]
V1200	2	12 August 2005	3×900	(+1.56, +0.78)
V1200	3	12 & 13 August 2005	3×900	(+1.56, −0.78)

[a] The original pointing of the telescope is 01:19:32.9 +14:52:19
[b] The V300 configuration was centered at 5361 Å covering the spectral range between 3591 and 6996 Å
[c] The V1200 configuration was centered at 5040 Å covering the spectral range between 4669 and 5395 Å

4.5.1 Velocity Map

The velocity map of NGC 469 can be seen in Figure 4-23. Measurements of the velocity down to our S/N limit were possible for a region extending over 40 arcsec in diameter. The apparent effective radius of NGC 469 is $r_e = 4.6$ arcsec (i.e., $r_e = 1.3$ kpc, at the redshift of the galaxy), which makes it one of the most compact galaxies in our sample. Further away, the S/N was not high enough to proceed to the measurement of the velocity.

The velocity map shows a distorted asymmetric gradual velocity field that expands $\sim$60 km s^{-1} in velocity. The velocities shown in the map are referenced to the redshift of

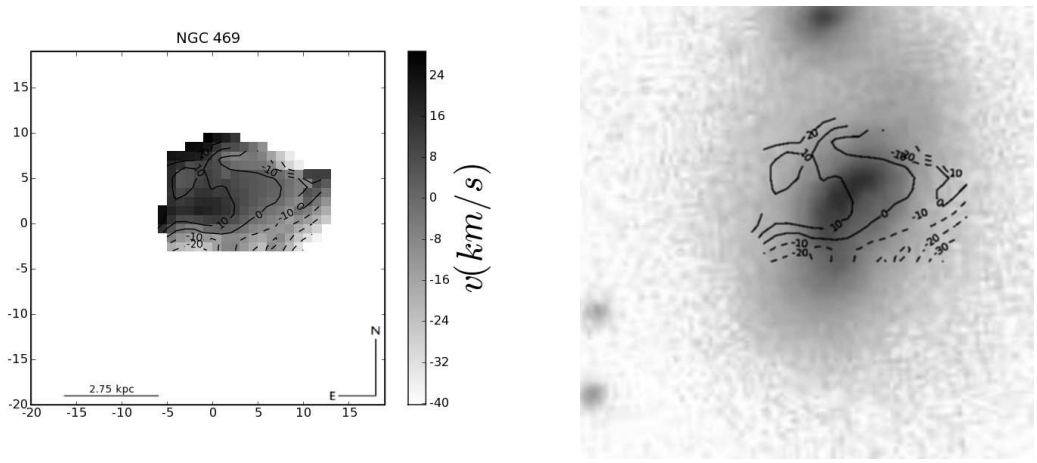

A B

Figure 4-23. A) PPAK Hα velocity map of NGC 469 using the low resolution V300 configuration. B) PPAK Hα velocity map contours overlaid on the SDSS image of NGC 469.

the central peak velocity width of the galaxy (Section 4.5.2). No absolute calibration of the recession velocity was attempted. This redshift roughly coincides within two sigma with the one available in the NASA Extragalactic Database ($z = 0.013673$).

4.5.2 Velocity Width Map

The velocity width map of the galaxy (Figures 4-24 and 4-25), in combination with the velocity map discussed in Section 4.5.1, discards NGC 469 as a rotating disk even though the velocity map shows a distorted but overall rotation.

The velocity width map of NGC 469 shows a rather constant width throughout the entire galaxy ($\sigma \sim 40$ km s^{-1}; Figure 4-18) even though the presence of a distorted asymmetric gradual velocity field. An elliptical background galaxy was needed to be removed from the FOV in order to proceed to this analysis. The velocity width of the galaxy ranges from about 30 to 70 km s^{-1} within a FOV covered by fibers for which S/N is at least 30.

4.5.3 Discussion

Mass. If we assume for NGC 469 a peak to peak velocity range as suggested by the velocity map derived above ($\sim$60 km s^{-1}), the inferred rotational velocity $v_{rot} = \sqrt{\frac{M_{dyn}G}{R_e}}$

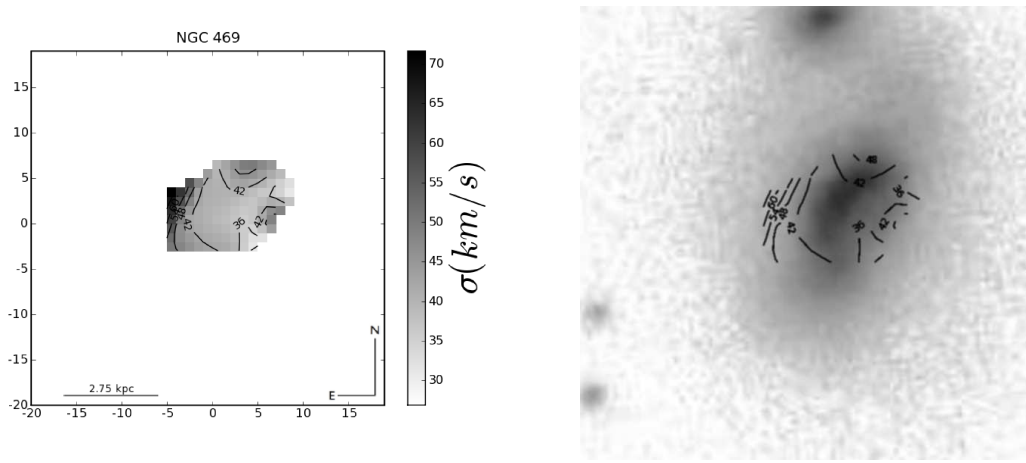

Figure 4-24. A) PPAK [OIII]λ5007 velocity width map of NGC 469 using the V1200 configuration. B) PPAK Hα velocity width map contours overlaid on the SDSS image of NGC 469. North is to the top and East is to the left.

translates into a dynamical mass within $R_e = 1.3$ kpc of around 3.0×10^8 $M_\odot$. An inclination of 84° was assumed as derived from the major and minor axis available in the SDSS catalog by means of Equation 3–1. For this galaxy Garland et al. (2004) found, from their HI study, $M_{\rm HI} = 2.0 \times 10^9$ $M_\odot$, and $M_{dyn}(R_e) = 3.9 \times 10^9$ $M_\odot$. The difference between both dynamical masses can be aggravated by the fact that Garland et al. (2004) used W_{20} to estimate v_{rot} and we have shown in Chapter 3 how by doing this, the value of v_{rot} (and, therefore, M_{dyn}) tends to be higher than the one estimated from the rotation curve for LCBGs. Nevertheless, the difference between the dynamical mass we derive and the HI mass from Garland et al. (2004) might be due to the fact that the velocity gradient we find is not tracing the dynamical mass of this galaxy. Remember that it is not classified as a rotating system because of its rather homogeneous velocity width map.

From our integrated PPAK data we find $W_{20} = 152 \pm 4$ km s^{-1}. If an inclination equal to 84° is also to be considered a rotational velocity $v_{rot} = 76$ km s^{-1} can be derived, which would translate into a mass about four times larger than the one derived from the peak to peak analysis.

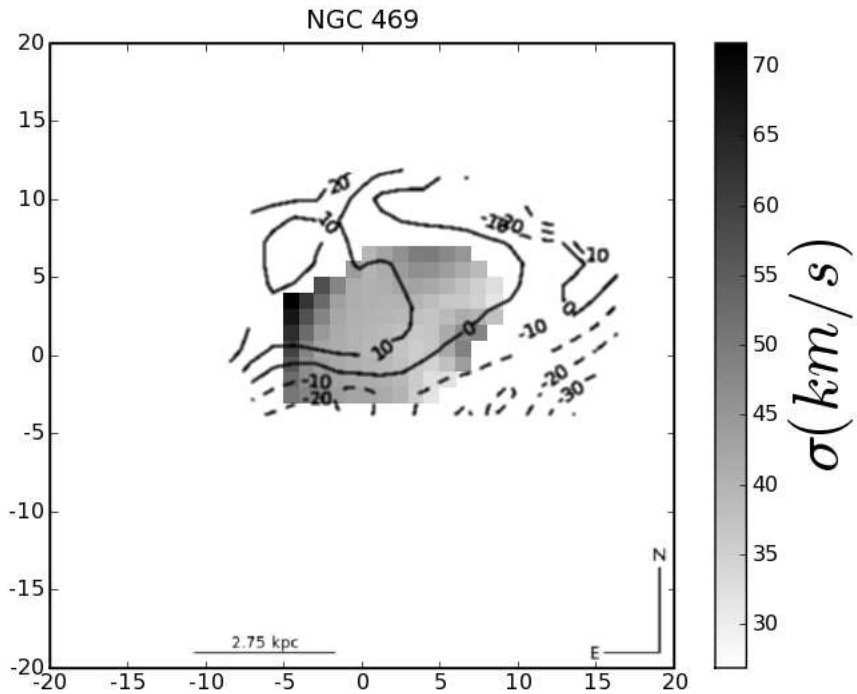

Figure 4-25. PPAK Hα velocity map contours overlaid on PPAK Velocity Width Map of NGC 469.

Evolution Among the galaxies in our representative sample of LCBG, those objects with the lower masses are the most probable to rapidly consume their current supply of gas (given we consider an average SFR for the entire population), fade and become present-day low-mass early-type galaxies, the so-called dwarf elliptical galaxies (Koo et al., 1994; Guzmán et al., 1996, 1997, 1998; Phillips et al., 1997; Noeske et al., 2006; Barton et al., 2006). At the current SFR (CM09a) the HI still present in NGC 469 would be exhausted in about 1 Gyr. Once the gas is exhausted, NGC 469 may be in a position to evolve into a dwarf elliptical galaxy.

The spectra and broadband colors of dwarf elliptical galaxies can best be explained by the presence of an old stellar population and a recent burst of star formation that has now almost or completely ceased. CM09b found for NGC 469 a low SFR, as stated above, and $Z = (0.6 \pm 0.2)\ Z_{\odot}$. The morphology, the dynamical mass, and the metallicity of

NGC 469 show agreement with those of prototypical dwarf elliptical galaxies (Young & Lo, 1997; Richer & McCall, 1995). Furthermore, a velocity gradient accompanied by a rather homogeneous velocity width distribution throughout the galaxy, as it is the case for NGC 469, is also typical of dwarf elliptical galaxies (van Zee et al., 2004). Therefore, despite a slightly larger effective radius, its similarities with the dwarf elliptical population seem to indicate that NGC 469 may evolve into one of them. If we consider the mass-to-light ratio ($M/L = 0.5$) and color $B - V$ ($B - V = 0.42$) of NGC 469 we can qualitatively predict how this galaxy will evolve once the burst is over. Following the model predictions for the evolution of a galaxy such as NGC 469 after a single initial burst of star formation, and after a second burst involving 1% of the total galaxy mass (Figure 3 from Guzmán et al., 1998), we would expect NGC 469 to fade about 3 magnitudes after 1 Gyr, which would place NGC 469 marginally at the TFR for dwarf elliptical galaxies (Figure 3-1; van Zee et al., 2004). Therefore, we can conclude that NGC 469 might be a progenitor of a dwarf elliptical galaxy.

CHAPTER 5
LUMINOUS COMPACT BLUE GALAXIES AT HIGH REDSHIFT

5.1 Distant LCBGs

The new generation of 10- and 30-m class telescopes will allow us to carry out a complete study of galaxies during the era of peak formation ($1 < z < 6$) as never before. While this range accounts for just ∼30% of the age of the Universe, it may account for ∼70% of its total star formation, heavy element production, and black hole accretion (Madau & Shull, 1996; Pei & Fall, 1995; Pei et al., 1999). We have already discussed the existence of a transition epoch at $z \sim 1$ in Chapter 1. The range $1 < z < 6$ is dominated by young, blue, active, late-type galaxies, rather than by older, redder, quiescent, more massive, early-type galaxies. This transition implies that most of the mass assembly occurs at $z > 1$. At $z \sim 2$, actually, is when the overall star formation rate (SFR) in the Universe peaks.

By means of the Hubble Space Telescope and 10-m class telescopes data from large samples of galaxies at $1 < z < 6$ is already available and have helped us in our understanding of the integrated rest-frame ultraviolet properties of the distant starburst population (Lowenthal et al., 1997; Steidel et al., 1999, 2001, 2003; Pettini et al., 2001; Shapley et al., 2001; Bouwens et al., 2004; Bunker et al., 2004; Malhotra et al., 2005). In the near future, major spectroscopic surveys, such as GOYA, will use the next generation of near-infrared (IR) spectrographs to study the integrated rest-frame optical properties of this population.

The goal of the GOYA collaboration is to understand the physical processes that determined the mass assembly and star formation of galaxies at redshift $z > 1$, the epoch of maximum star formation activity in the universe. The foundation of the project is a near-IR spectroscopic survey of 2500 galaxies at $z > 1$ using guaranteed time with EMIR, a cryogenic near-IR multi-slit spectrograph at the 10.4-m Gran Telescopio Canarias (GTC). EMIR will provide simultaneous integrated spectra of up to 50 objects in a field

of view (FOV) of 6×4 arcsec^2 with $R = 4000$. In order to achieve this goal one of the scientific interests of the GOYA collaboration is to study the structure, dynamic, gas content, and stellar population of Luminous Compact Blue Galaxies (LCBGs) at high redshift.

However, the empirical understanding of galaxy formation ultimately requires detailed mapping of the physical properties, including kinematics, metallicity, age, star formation rate, and extinction, as a function of spatial position within each galaxy. Current surveys focus on LCBG-like galaxies with redshifts ranging from $z = 0.4$ to $z = 0.6$ (e.g., Puech et al., 2006; Yang et al., 2008), from $z = 1.2$ to $z = 1.6$ (around the peak of star formation; e.g., Epinat et al., 2009), and at $z \sim 2$ (e.g., Förster Schreiber et al., 2006, 2009), using instruments like GIRAFFE or SINFONI at the Very Large Telescope of the European Southern Observatory. The results of these surveys seem to imply that galaxy kinematics are among the most rapidly evolving properties, because while locally only a few percent of the galaxies in this mass range have complex kinematics, this appears to be a trend at higher redshifts (Le Fèvre et al., 2000). Galaxies undergoing a merger have complex large-scale motions, therefore mergers are likely to be responsible for the strong evolution of galaxy kinematics.

These surveys have the potential to set the basis to understand the essentials behind galaxy formation and evolution. Nevertheless, it will be the combination of the collecting area of the new generation of 30-m class telescopes, the unique capabilities of Adaptive Optics (AO), and the flexibility provided by multiple IR Integral Field Units (IFUs), which may revolutionize the study of galaxies at these and younger epochs, enabling detailed mapping of these physical properties for thousands of galaxies at $z = 2$–6. Such a survey will be a major milestone towards an empirical determination of the physics and timeline of galaxy assembly in this most interesting era of peak star formation activity.

In addition to using local LCBGs as a proxy for learning about the nature and evolution of $z \sim 1$ LCBGs, three dimensional (3D) spectroscopy data of local LCBGs

can also be used to simulate observations of distant LCBGs (e.g., Puech et al., 2008; Gruel, Guzmán, & Pérez-Gallego, 2009). These simulations are essential in order to help in the correct interpretation of the results associated to current and future observations of distant galaxies, and compensate for any possible biases introduced by cosmological factors, low signal-to-noise, and instrument limitations, associated to these observations. In Section 5.2 we summarize the work I have been doing in collaboration with Nicolas Gruel and Rafael Guzmán on this subject. In particular, I was in charge of implementing the simulation method and producing the first simulations of these objects. Later, Nicolas Gruel, was in charge of making these simulations user-friendly, process in which i was also involved by providing everything i learned from my work.

Additionally, if LCBGs are obtained at a variety of redshifts between $2 \leq z \leq 4$, and reliable measurements of their velocity widths are provided, together with redshifts, Hβ luminosities, and metallicities, different cosmological models can be tested by means of a well-stablished standard candle (Melnick, Terlevich, & Moles, 1988; Melnick, Terlevich, & Terlevich, 2000; Siegel, Guzmán, Pérez-Gallego, et al., 2005). This particular method has the potential of providing very tight constraints in the specific measurement of the mass density (Ω_m), independent of any constraints arising from other sources, including cosmic microwave background (CMB) and type Ia supernova (SNIa) data. In Section 5.3 we summarize the work I have been doing in collaboration with Ethan Siegel and Rafael Guzmán on this subject. Aside from actively contributing on all the aspects of the project, I was in charge of compiling the necessary data for the study of the universality of the standard candle discussed, and discussing this universality.

5.2 Simulations

Simulations of well resolved, both spatially and spectrally, local LCBGs are necessary in order to study 3D spectroscopy data sets of LCBGs at $z \geq 1.5$. These simulations may help in the accuracy of the kinematic measurements and classification of distant LCBGs as seen in Chapter 3.

PPAK 3D spectra can be used to simulate spatially and spectrally resolved observations of LCBGs at $z = 1.5$ and $z = 2.5$ as if they had been obtained using FRIDA at the GTC (see Figure 5-1). FRIDA is an infrared imager and IFS, and the first instrument that will be built for the adaptive optics system of the 10.4-m telescope GTC. The input data for these simulations are actual PPAK 3D spectra of a nearby $L^\star$ starburst galaxy (NGC 7714; North is to the left and East is to the bottom; Chapter 4), scaled to the characteristic values of the high-redshift Lyman-break galaxy population (i.e., $L = 4\ L^\star$ $R_e = 4.5$ Kpc, $L_{\mathrm{H}\alpha} = 10^{43}$ erg s^{-1}). We considered a FRIDA instrumental configuration with 30 slits with a spatial scale of 0.02×0.04 arcsec^2, a FOV of 1.2×1.2 arcsec^2, and $R = 4000$. These simulations consist essentially of (i) redshifting the galaxy 3D spectra to the desired redshift, which translates into a drop in the incoming flux because of the different distance moduli; (ii) adding the appropriate sky 3D spectra to our object 3D spectra (e.g., at $z = 2.5$ the rest-frame optical corresponds to the K band); (iii) making the spectra go through the instrumental set-up (i.e., the telescope and the spectrograph); (iv) subtracting the sky from our final 3D spectra composed of the object's, the sky's, and noise due to the observation process, which is generally dominated by background noise. We use different but equivalent sky spectra generated by Monte Carlo simulations, so we do not add and subtract the exact same one. For the simulation at $z = 1.5$, we assumed $t = 1$ hour integration time on source, while for the simulation at $z = 2.5$ we assumed $t = 4$ hours. In Figure 5-1 the right two panels show the actual maps for SFR and velocity as derived from the actual PPAK rest-frame optical spectra of our reference galaxy at $z \sim 0$. The top panel shows the SFR map. There are clearly three giant regions of star formation with typical scales of a few hundred parsecs and SFR ranging from $\sim$12 $M_\odot$/yr to $\sim$1 $M_\odot$/yr superimposed on an extended, underlying population with average SFR $\sim$0.01 $M_\odot$/yr. The bottom panel shows the velocity map derived from the Hα emission line centroids. The derived rotational velocity is $v/\sin i = 98$ km s^{-1}. The middle two panels show the same maps derived from the

simulated FRIDA observations of the same galaxy at $z = 1.5$. The FRIDA detection threshold allows regions with SFR as low as 0.1 $M_\odot$/yr per resolution element to be detected at $z = 1.5$. Finally, the right panels show the SFR and velocity maps derived from the simulated FRIDA observations for the same galaxy at $z = 2.5$, where only regions with $SFR > 0.3$ $M_\odot$/yr are detected in each resolution element.

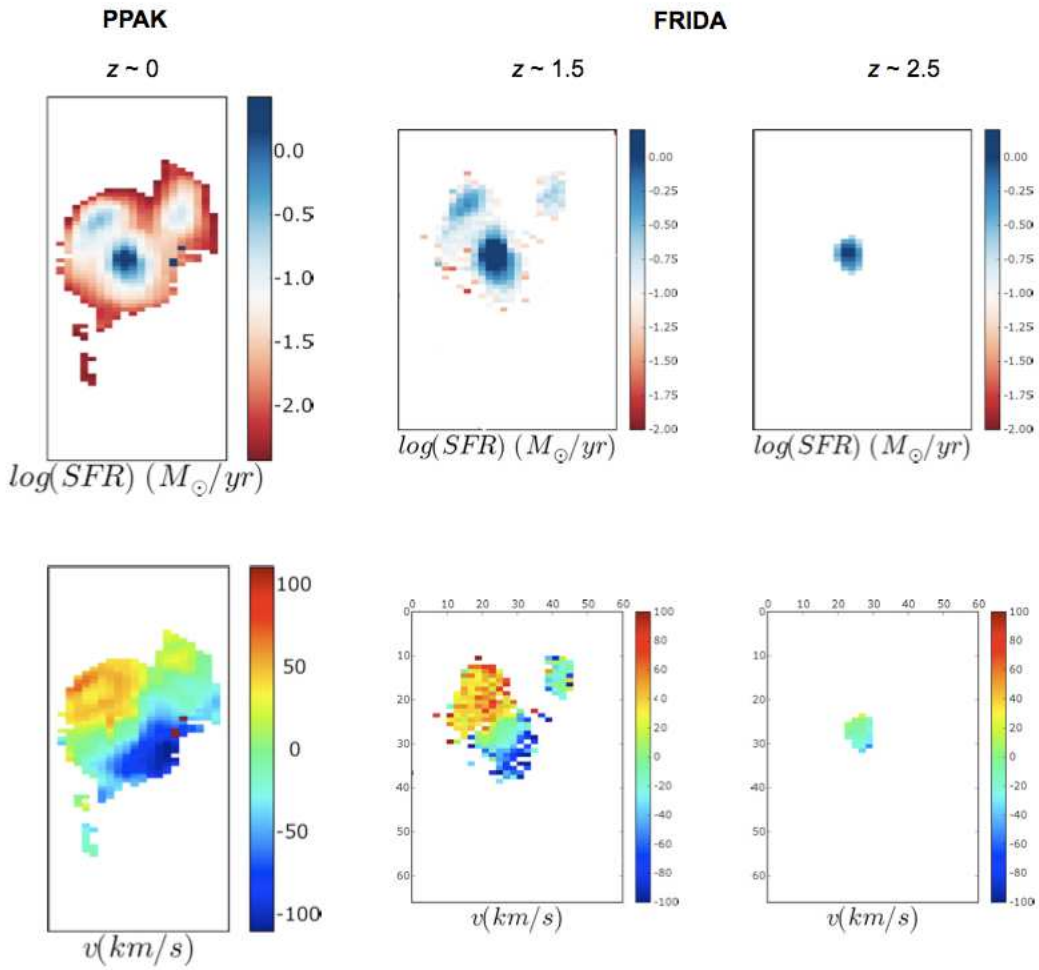

Figure 5-1. *First column:* Actual maps for SFR, and velocity as derived from the actual PPAK rest-frame optical spectra of our reference galaxy at $z \sim 0$. The first panel shows the SFR map. *Middle column:* The same maps derived from the simulated FRIDA observations of the same galaxy at $z = 1.5$. *Last column:* The SFR and velocity maps derived from the simulated FRIDA observations at $z = 2.5$.

A similar instrument (hereafter FRIDA2) but in a 30-m class telescope, is necessary in order to achieve the same data quality as FRIDA is able to provide at $z = 1.5$ further than $z \sim 2$. Again, PPAK 3D spectra can be used to simulate spatial and spectrally resolved observations of distant LCBGs. Figure 5-2 and 5-3 show the results derived from realistic simulated observations of a prototypical LCBG-like Lyman-break galaxy at $z = 2.5$ and at $z = 5.5$.

Figure 5-2 simulates observations of a typical LCBG-like Lyman-break galaxy at redshifts $z = 2.5$ and $z = 5.5$ using FRIDA2 with 20 IFUs at a 30-m telescope. The input data for these simulations are actual PPAK 3D spectra of a nearby $L^\star$ starburst galaxy (NGC 7714; North is to the left and East is to the bottom; Chapter 4), scaled to the characteristic values of the high-redshift Lyman-break galaxy population (i.e., $L = 4\ L^\star$ $R_e = 4.5$ Kpc, $L_{\mathrm{H}\alpha} = 10^{43}$ erg s^{-1}). We considered a FRIDA2 instrumental configuration with 50 mas slitlets width and $R = 4800$. For the simulation at $z = 2.5$, we assumed $t = 1$ hour integration time on source, while for the simulation at $z = 5.5$ we assumed $t = 4$ hours. The top right panel shows an image of the Hubble Ultra Deep Field. Lyman-break galaxy candidates at $z = 2$–6 are identified with green squares (e.g., Elmegreen et al., 2005; Malhotra et al., 2005). An actual FRIDA2 probes configuration is shown in yellow lines. The top left panel shows the simulated deep near-IR image of our prototypical Lyman-break galaxy at $z = 2.5$ as seen in a single FRIDA2 IFU. The IFU FOV is 1.1×2.2 arcsec^2. The two middle right panels show the sky-subtracted spectra at $z = 2.5$ for various slitlets in the wavelength range around Hβ and [OIII]$\lambda\lambda$4959,5007 as observed in H-band, and around Hα as observed in K-band. Spatially resolved emission-line substructure is clearly seen in these 2D spectra. The bottom right panel shows the sky-subtracted spectra at $z = 5.5$ for various slitlets in the wavelength range around [OII]λ3727 as observed in the K-band. The left middle and bottom panels illustrate the characteristic S/N in the observed emission lines at various

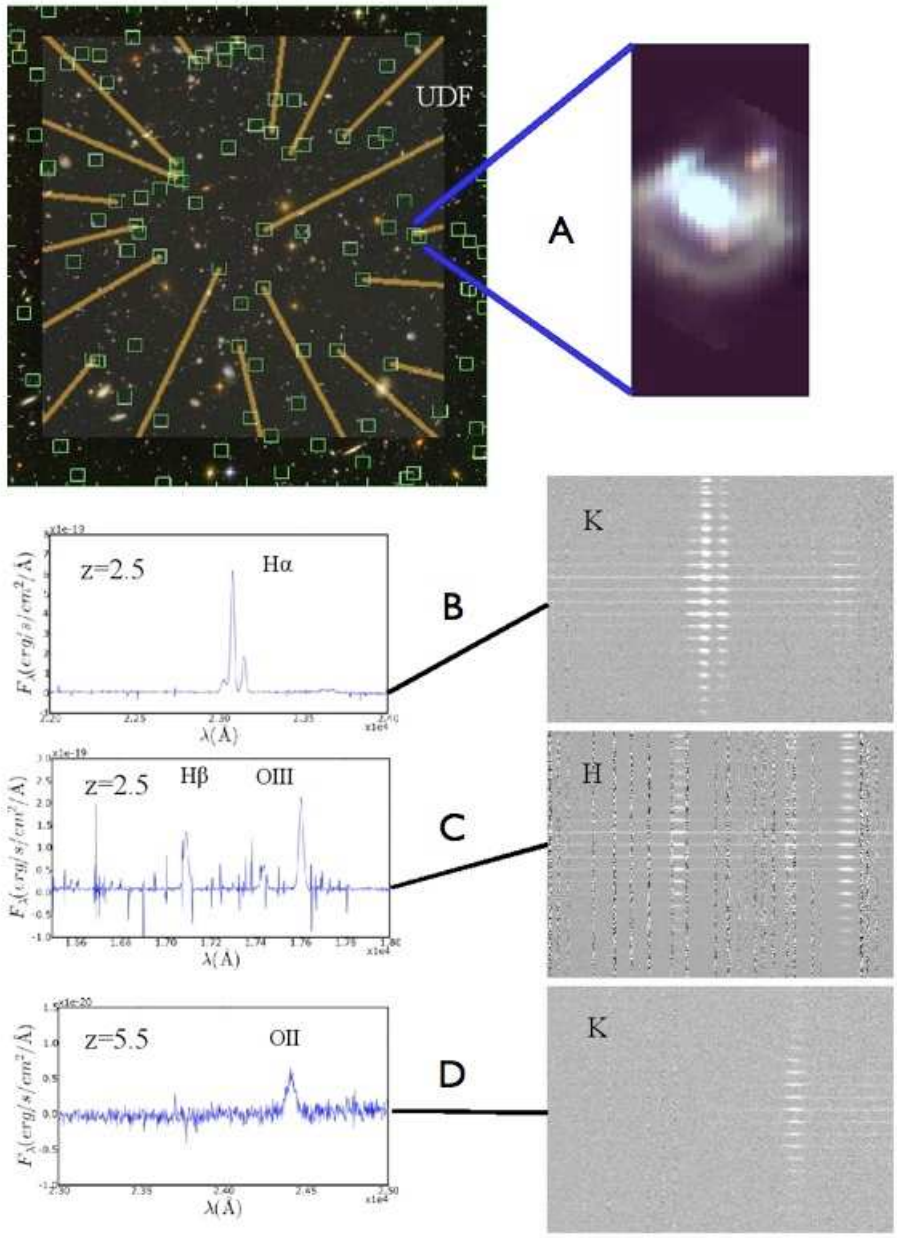

Figure 5-2. A) Simulated deep near-IR image of our prototypical Lyman-break galaxy at $z = 2.5$ as seen in a single FRIDA2 IFU. B–C) 2D sky-subtracted spectra at $z = 2.5$ for various slitlets in the wavelength range around Hβ as observed in H-band, and around Hα as observed in K-band; and at $z = 5.5$ around [OII]λ3727 as observed in the K-band. D) Characteristic S/N in the observed emission lines at various flux levels.

flux levels: 1.6 x 10^{-17} erg s^{-1} cm^{-2} in Hβ at $z = 2.5$, 3.2 x 10^{-18} erg s^{-1} cm^{-2} in Hα at $z = 2.5$, and 3.2 x 10^{-19} erg s^{-1} cm^{-2} in [OII]λ3727 at $z = 5.5$.

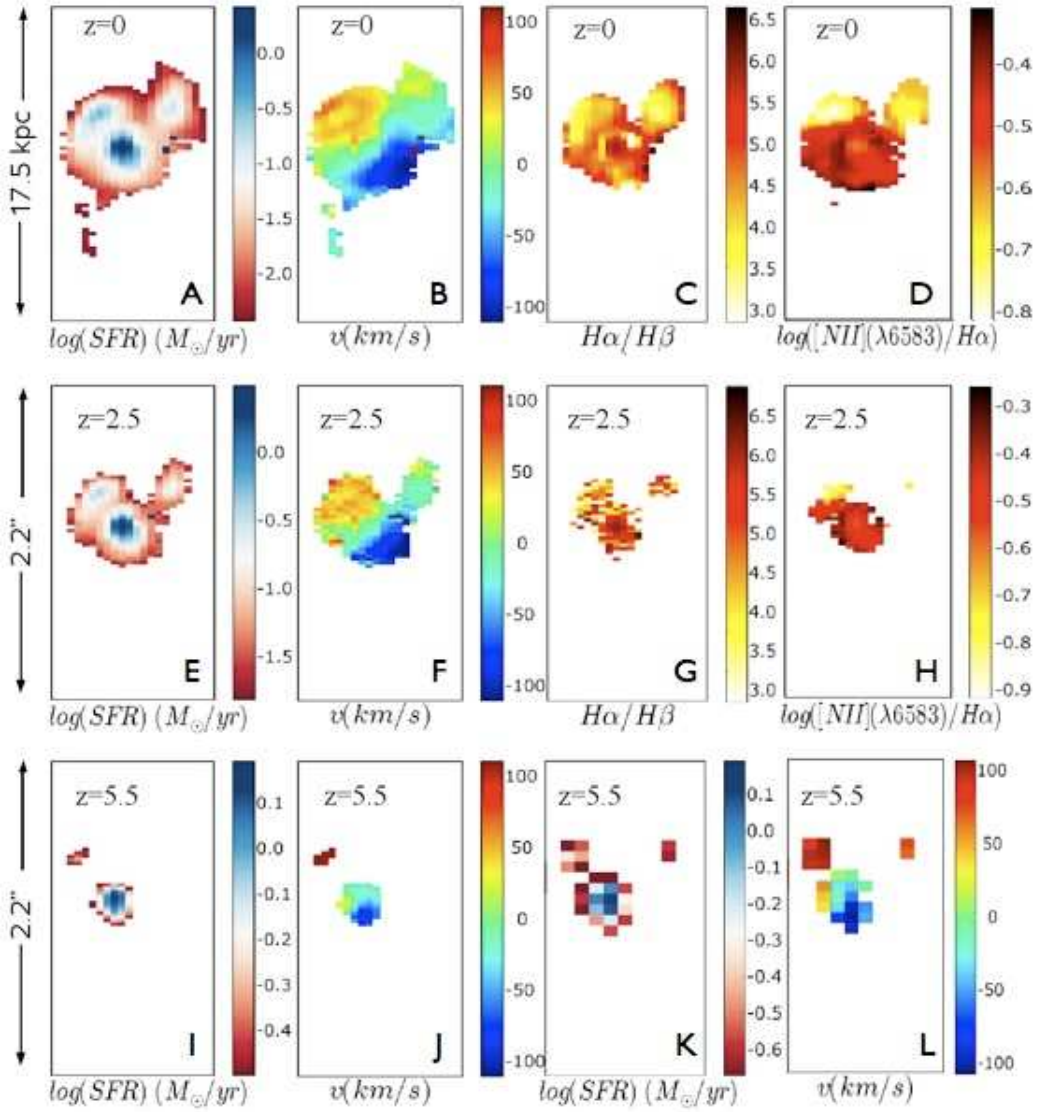

Figure 5-3. A–D) Actual maps for SFR, velocity, extinction, and metallicity as derived from the actual PPAK rest-frame optical spectra of our reference galaxy at $z \sim 0$. The first panel shows the SFR map. E–H) The same maps derived from the simulated FRIDA2 observations of the same galaxy at $z = 2.5$. I–L) The SFR and velocity maps derived from the simulated FRIDA2 observations of [OII]λ3727 for the same galaxy at $z = 5.5$.

On the other hand, in Figure 5-3 the top four panels show the actual maps for SFR, velocity, extinction, and metallicity as derived from the actual PPAK rest-frame optical spectra of our reference galaxy at $z \sim 0$. The first panel shows the SFR map, the second panel shows the velocity map derived from the Hα emission line centroid, and the third panel shows the extinction map as derived from the Hα/Hβ ratio. Finally, the fourth panel shows the metallicity map as derived from the NII/Ha ratio. The increase in extinction and metallicity in the central starburst region compared to the rest of the galaxy is clearly noticeable. The middle four panels show the same maps derived from the simulated FRIDA2 observations of the same galaxy at $z = 2.5$. The FRIDA2 detection threshold allows regions with SFR as low as 0.01 $M_{\odot}$/yr per resolution element to be detected at $z = 2.5$. Finally, the bottom panels show the SFR and velocity maps derived from the simulated FRIDA2 observations of [OII]λ3727 for the same galaxy at $z = 5.5$. Although only regions with SFR > 0.05 $M_{\odot}$/yr are detected in each resolution element, by averaging the information from the lower surface brightness areas, correct values for the SFRs, rotational velocity, extinction and metallicity may still be derived (see bottom right panels). In summary, the spatial resolution and sensitivity of FRIDA2 at a 30-m telescope will allow study of 30Dor-like star forming regions in starburst galaxies up to $z \sim 6$. In addition, intermediate spectral resolutions ($R \sim$ 5000–10000) would provide detailed kinematic measurements down to 10–30 km s^{-1}. This resolution is ideal to study velocity widths of individual star-forming regions, which typically range between 10 and 30 km s^{-1} (Melnick, Terlevich, & Moles, 1988), kinematic components revealing the presence of SN-driven galactic winds over kiloparsec-scale structures expanding at typical velocities of 20–100 km s^{-1} (Marlowe et al., 1995), or galaxy rotation curves. In particular, the direct measure of the amount of thermal energy transferred to the interstellar medium from these kinematic features will allow quantification of the important role SN (or AGN) driven winds may play as the main feedback mechanism in galaxy/star formation models at a very early epoch.

Similarly, PPAK integrated spectroscopic data of a nearby $L^\star$ galaxy can be used to simulate spectrally resolved observations of LCBGs at $z = 2.5$ as they had been obtained using EMIR at the GTC. The input data for these simulations are the actual PPAK integrated spectrum of a nearby L* starburst galaxy (NGC 7714), scaled to the characterisitic values of the high-redshift Lyman-break galaxy population (i.e., $L = 4L^\star$, $L_{\mathrm{H}\alpha} = 10^{43}$ erg s^{-1}; Figure 5-4). These simulations can be compared with actual observations using EMIR at GTC, which will be providing integrated spectra for a statistically representative sample of LCBGs at $z \sim 2$ in the near future, which will facilitate, among other, reliable measurements of the fluxes and velocity dispersions of these objects.

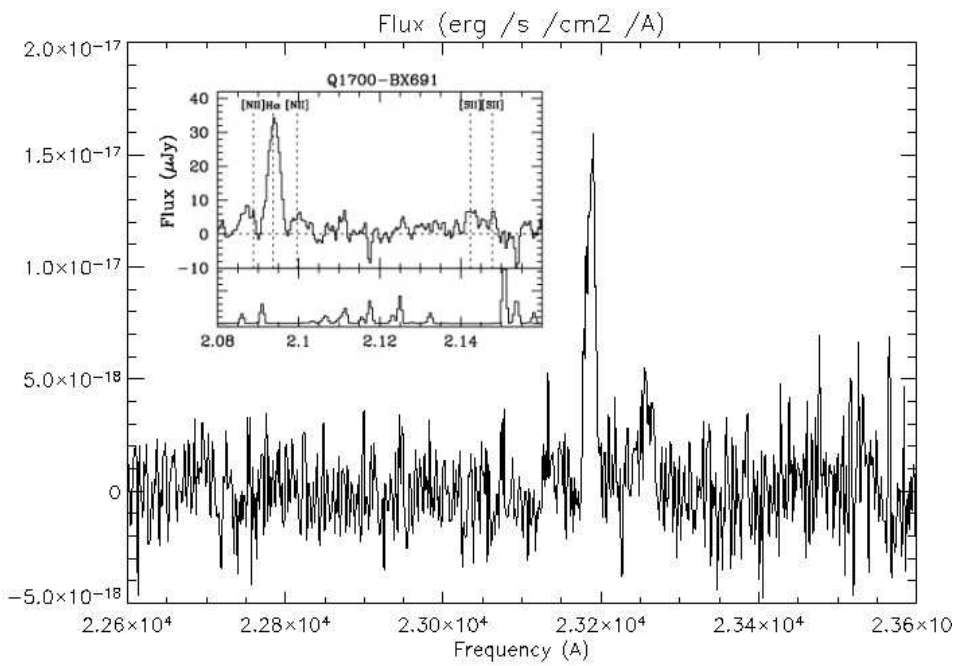

Figure 5-4. Simulated integrated spectrum of a nearby LCBG redshifted to $z = 2.5$ as if it had been obtained using EMIR at the GTC. In the panel we can see an actual observation of a starburst galaxy at $z > 2$ by Erb et al. (2003). Notice that our simulated is spectrum is per Å and not per resolution element.

5.3 Distance Indicators

Recent improvements in the measurements of the CMB (Bennett et al., 2003), SNIa (Riess et al., 2000), and galaxy surveys (Hawkins et al., 2003; Bahcall et al., 2003) have

placed stringent constraints on the cosmological parameters describing the universe. Consistent values have been found for the mass density (Ω_m), vacuum energy density (Ω_Λ), the dark energy equation of state parameter (w), and the value of spatial curvature in the universe (Ω_k). Different independent approaches, however, are necessary for consistency and accuracy, as well as for minimizing systematic errors.

Ω_m is the cosmological parameter with the greatest number of independent measurement approaches: the Sunyaev-Zel'dovich effect (Grego et al., 2001), weak gravitational lensing (Hoekstra et al., 2001), X-ray luminosities (Borgani et al., 2001), large scale clustering (Schuecker et al., 2003), peculiar velocities of galaxy pairs (Feldman et al., 2003), and SNe data (Knop et al., 2003). These approaches have yielded 2-σ consistent results ranging from $\Omega_m = 0.13$–0.35. These approaches, however, are not sensitive enough to Ω_Λ, Ω_k, and w to differentiate between different cosmological models. In order to overcome this, a reliable standard candle is needed at high redshift, where the distance moduli of extragalactic objects become sensitive to these cosmological parameters.

Melnick, Terlevich, & Moles (1988, hereafter MTM) first found a correlation between the luminosity in the Hβ line ($L_{\mathrm{H}\beta}$), the velocity dispersion (σ), and metallicity (O/H) of nearby LCBG-like HII galaxies. This correlation, when applied to distant LCBGs, allows for discrimination between different values of Ω_m (as first suggested by Melnick, Terlevich, & Terlevich, 2000, hereafter MTT), and has the potential of being that standard candle needed for differetiating between different cosmological models, as discussed in more detail in Siegel, Guzmán, Pérez-Gallego, et al. (2005), and summarized here.

LCBG-like HII galaxies (and HII regions) are characterized be the presence of a large star-forming region, where O- and B-type stars are being form and ionizing the surrounding hydrogen gas. The typical spectrum of these galaxies shows, therefore, strong Hα and Hβ emission lines. The $L_{\mathrm{H}\beta}$ of giant HII regions is strongly correlated with their σ (Terlevich & Melnick, 1981). Melnick et al. (1987) and MTM extended this correlation to LCBG-like HII galaxies and showed the potential of this correlation as a distance

indicator. This correlation relates the $L_{\mathrm{H}\beta}$, σ, and O/H of LCBG-like HII galaxies:

$$\log L_{\mathrm{H}\beta} = \log M_z + 29.60 \ , \qquad M_z \equiv \frac{\sigma^5}{\mathrm{O/H}} \ , \tag{5–1}$$

where the constant 29.60 is due to a zero-point calibration of nearby giant HII regions (MTT), and our choice of the Hubble constant ($H_0 = 71$ km s^{-1} Mpc^{-1}). LCBGs observed at different epochs show the same strong Balmer emission lines and intense star formation activity (Pettini et al., 2001; Erb et al., 2003) as nearby LCBG-like HII galaxies.

5.3.1 Selection of the Data Sample

Following the analysis in MTT, the distance modulus (DM) of LCBG-like HII galaxies can be derived from:

$$DM = 2.5\log(\frac{\sigma^5}{F_{\mathrm{H}\beta}}) - 2.5\log(\mathrm{O/H}) - A_{\mathrm{H}\beta} - 26.18 \ , \tag{5–2}$$

where the constant 26.18 is due to H_0, and Equation 5–1. Interestingly, Equation 5–2 expresses DM in terms of only observational parameters. As discussed above, while DM is insensitive to Ω_m, Ω_Λ, Ω_k, and w at low redshifts ($z \leq 0.1$), at high redshifts ($z > 2$), it can differ up to 3 magnitudes depending on the choice of parameters. Among the four cosmological parameters, as already stated by MTT, DM is most sensitive to changes in Ω_m. However, for values of $\Omega_m \leq 0.3$, DM is sensitive to variations in the other parameters by 0.2–0.5 mag. Since other measurements indicate that $\Omega_m \leq 0.3$, we also consider variations in Ω_Λ and Ω_k.

We selected LCBG-like galaxies from Pettini et al. (2001) and Erb et al. (2003). Measurements for many of the desired observational parameters and related quantities for the 36 galaxies in their samples were already available.

As LCBG-like HII galaxies evolve in time and the gas available for star formation is consumed, the death rate of short-lived O- and B-stars exceeds their birth rate, causing a galaxy to be under-luminous in Hα and Hβ for its mass. The correlation between $L_{\mathrm{H}\beta}$, σ, and O/H holds true for galaxies whose dynamics are dominated by O- and B-type stars,

and ionized hydrogen gas surrounding them. By examining the EW of the galaxies in these samples we can cut out the older, more evolved, under-luminous galaxies. With this in mind, we did not include galaxies with $EW \leq 20\,\text{Å}$.

A second cut-off is necessary to account for the fact that a large fraction of local LCBG-like HII galaxies contain multiple bursts of star formation (Melnick et al., 1987). When multiple unresolved burst of star formation are present, relative motions of those will broaden the observed (Melnick et al., 1987). The correlation between $L_{\text{H}\beta}$, σ, and O/H holds true for galaxies dominated by one major burst of star formation. Since we do not have neither the sufficient S/N, nor resolution to remove this effect, we apply a cut on σ. Monte Carlo simulations indicate that when $\sigma > 130$ km s^{-1}, it is likely due to the presence of multiple bursts of star formation, therefore, all galaxies with $\sigma > 130$ km s^{-1} are discarded. When imposing the cuts on σ and EW we were left with 15 out of the 36 original galaxies, creating the sample used for our analysis (Table 5-1; Siegel, Guzmán, Pérez-Gallego, et al., 2005).

Unfortunately, not all of the necessary data to calculate DM using Equation 5–2 were available in the literature for these galaxies, so assumptions were necessary to account for the missing information. z was measured for all galaxies by the vacuum heliocentric redshifts of the nebular emission lines. σ was obtained for all galaxies from the broadening of the Balmer emission lines, Hα for the galaxies from Erb et al. (2003), and Hβ for the galaxies from Pettini et al. (2001). $F_{\text{H}\beta}$ was measured directly for the galaxies in Pettini et al. (2001), but Erb et al. (2003) measured $F_{\text{H}\alpha}$ instead, thus $F_{\text{H}\alpha}$ was converted to $F_{\text{H}\beta}$. The conversion for the emitted flux is given by Osterbrock (1989) as $F_{\text{H}\alpha} = 2.75\,F_{\text{H}\beta}$, where observed fluxes must be corrected for extinction. Therefore, the complete conversion is given by

$$F_{\text{H}\beta} = \frac{1}{2.75}\,F_{\text{H}\alpha}\,10^{\left(\frac{A_{\text{H}\alpha}-A_{\text{H}\beta}}{2.5}\right)}\,, \tag{5–3}$$

where $A_{\text{H}\alpha}$ and $A_{\text{H}\beta}$ are the extinctions in Hα and Hβ, respectively. Obtaining O/H was more difficult, as measurements of metallicity only existed for 5 of the 36 original galaxies.

Table 5-1. Selected starburst galaxies with their properties and DM.

Name	z	σ (km s^{-1})	$F_{\mathrm{H}\beta}$ (10^{-17} erg s^{-1} cm^{-2})	12+log (O/H) (mag)	EW (Å)	DM[a] (mag)	
Q0201-B13	2.17	62 ± 29	0.9 ± 0.2	8.55	0.013	23	$47.49^{+2.10}_{-3.43}$
Q1623-BX432	2.18	51 ± 22	1.9 ± 0.5	8.55	0.157	72	$45.45^{+1.97}_{-3.07}$
Q1623-MD107	2.54	≤ 42	1.3 ± 0.3	8.55	0.141	21	$44.82^{+0.31}_{-1.58}$
Q1700-BX717	2.44	≤ 60	1.3 ± 0.3	8.55	0.285	25	$46.64^{+0.31}_{-1.58}$
Q1700-MD103	2.32	75 ± 21	2.4 ± 0.6	8.55	0.735	47	$46.72^{+1.38}_{-1.80}$
SSA22a-MD41	2.17	107 ± 15	2.6 ± 0.7	8.55	0.214	31	$48.96^{+0.78}_{-0.85}$
CDFa C1	3.11	≤ 63	3.4 ± 1.0	8.55	0.505	28	$45.77^{+0.31}_{-1.58}$
Q0347-383 C5	3.23	69 ± 4	≤ 1.7	8.55	0.237	≤ 27	$47.12^{+0.44}_{-0.32}$
B2 0902+343 C12	3.39	87 ± 12	2.7 ± 0.3	8.70 ± 0.08	0.773	37	$46.96^{+0.71}_{-0.81}$
Q1422+231 D81	3.10	116 ± 8	4.1 ± 0.4	8.62 ± 0.07	0.237	43	$48.81^{+0.38}_{-0.40}$
SSA22a-MD46	3.09	67 ± 6	≤ 2.3	8.55	0.110	≤ 31	$46.76^{+0.56}_{-0.51}$
SSA22a-D3	3.07	113 ± 7	1.3 ± 0.3	8.39 ± 0.16	1.01	25	$49.71^{+0.43}_{-0.41}$
DSF2237+116a C2	3.32	100 ± 4	3.5 ± 0.4	8.55	0.852	25	$47.73^{+0.25}_{-0.25}$
B2 0902+343 C6	3.09	55 ± 15	3.0 ± 1.0	8.55	0.284	40	$45.22^{+1.38}_{-1.76}$
MS1512-CB58	2.73	81	1.35 ± 0.2	8.49 ± 0.10	1.14	26	$47.49^{+1.22}_{-1.57}$

[a] DM is given in mag with 1-σ random errors.

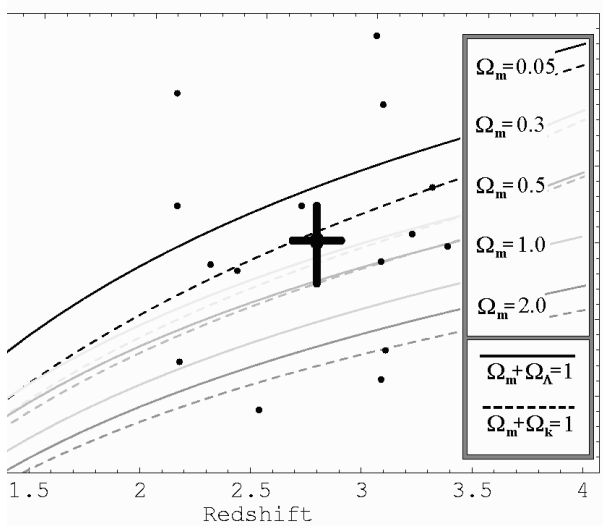

Figure 5-5. DM vs. z for various cosmological models, with the selected galaxies. The crosshairs represents the 1-σ constraints on the DM vs. z parameter space from the selected data sample.

An average value of O/H was used for those galaxies for which O/H measurements were not available.

Values of O/H for five galaxies in Pettini et al. (2001) were obtained by means of measurements of the [OII]λ3727, and [OIII]$\lambda\lambda$4959,5007 emission lines. The R_{23} (Patel et al., 1979) index was assumed to have its temperature-metallicity degeneracy broken towards the higher value of O/H, as it seems to be the case for LCBGs at intermediate redshifts (Kobulnicky & Koo, 2000). The mean of the values of O/H for these five galaxies was then taken to be the average metallicity for each of the other galaxies where such line measurements were not available. Alternatively, Shapley et al. (2004), using the [NII]$\lambda\lambda$6548,6584/Hα ratio as their metallicity indicator, obtained an average O/H of 8.33 for the galaxies found in Erb et al. (2003).

$A_{\mathrm{H}\beta}$ was derived from the $E(B-V)$ color excess of the galaxy in question. While extinction laws are known and established for the Milky Way, the Large and Small Magellanic Clouds (LMC and SMC, respectively), and the HII regions of the LMC and SMC (Gordon et al., 2003), they have not been established for starburst galaxies in general. If we assume dust in LCBGs to be comparable to that in giant HII regions, $A_{\mathrm{H}\beta}$

for starburst galaxies can be approximated by the $A_{\mathrm{H}\beta}$ derived in Gordon et al. (2003) for the HII regions of the LMC and SMC. A best fit applied to the data in Gordon et al. (2003) yielded $A_{\mathrm{H}\beta} = (3.28 \pm 0.24)\, E(B-V)$ and $A_{\mathrm{H}\alpha} = (2.14 \pm 0.17)\, E(B-V)$ for starburst galaxies. These results were also applicable to the flux conversion in Equation 5–3. For the galaxies from Pettini et al. (2001), for which $E(B-V)$ was not available, $E(B-V)$ was derived from the correlation between $E(B-V)$ and $(G-R)$ corrected colors for starburst galaxies in Erb et al. (2003) (i.e., $E(B-V) \approx 0.481\,(G-R)$).

Finally, EW was measured for all galaxies in Pettini et al. (2001), but not for those in Erb et al. (2003). For the latter only the spectra for the Hα line. EW was estimated for the Erb et al. (2003) galaxies by estimating the continuum height from each spectra and the area under each Hα peak, calculating the equivalent width in Hα, and converting to Hβ using the Balmer decrements of Osterbrock (1989). The complete data set is listed in Table 5-1 (Siegel, Guzmán, Pérez-Gallego, et al., 2005).

5.3.2 Results

The comparison between the calculated distance modulus for each galaxy in our sample and the predicted values of DM at a given redshift for different cosmological models provides a constraint on the cosmological parameters. As pointed out by MTT, at high redshifts, DM is most sensitive to the variation of the cosmological parameter Ω_m. Each galaxy yields a measurement for DM and for z. Although there are multiple models consistent with each individual measurement, observations of many galaxies at different redshifts will allow the construction of a best-fit curve, which is unique to the choice of cosmological parameters Ω_m, Ω_Λ, Ω_k, and w. A data sample of 15 galaxies is insufficient to distinguish between models in this fashion, as the uncertainties in each individual measurement of DM are too large. The method by which the uncertainties can be reduced is to bin the data according to redshift and find a best-fit value of DM at that point. Due to the size of our sample, all 15 points were averaged into one point of maximum likelihood to constrain the cosmology, with errors arising from the random errors of the

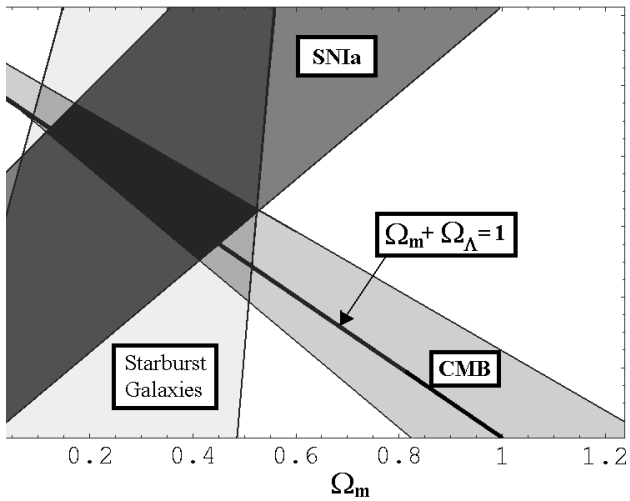

Figure 5-6. 1-σ constraints in Ω_m vs. Ω_Λ parameter space from starburst galaxies, along with older constraints from CMB and SNIa data, found in de Bernardis et al. (2000).

individual points and from the distribution of points. The average value obtained is $DM = 47.03^{+0.46}_{-0.56}$ at a redshift $z = 2.80 \pm 0.11$. The different cosmological models, along with the most likely point and the raw data points, are displayed in Figure 5-5 (Figure 1 of Siegel, Guzmán, Pérez-Gallego, et al., 2005), with $H_0 = 71$ km s^{-1} Mpc^{-1}.

The constraints placed on Ω_m from the analysis described here are $\Omega_m = 0.21^{+0.30}_{-0.12}$ in a Λ-dominated universe ($\Omega_m + \Omega_\Lambda = 1$; $\Omega_k = 0$) and $\Omega_m = 0.11^{+0.37}_{-0.19}$ in an open universe ($\Omega_m + \Omega_k = 1$; $\Omega_\Lambda = 0$) (Siegel, Guzmán, Pérez-Gallego, et al., 2005). Figure 5-6 (Figure 2 of Siegel, Guzmán, Pérez-Gallego, et al., 2005) shows the comparison in Ω_m vs. Ω_Λ parameter space between the preliminary constraints of this work and early constraints arising from CMB data and SNIa data (from de Bernardis et al., 2000).

CMB and SNIa constraints led to the first reliable estimates of Ω_m and Ω_Λ. The preliminary constraints presented here are comparable to early constraints from CMB and SNIa data, as shown in Figure 5-6 (Figure 2 of Siegel, Guzmán, Pérez-Gallego, et al., 2005). The accuracy in Ω_m and Ω_Λ, as determined from recent CMB and SNIa data (Bennett et al., 2003) is now ± 0.04 in each parameter. A similar, and perhaps even

superior accuracy can be achieved using starburst galaxies at high redshifts, as discussed in the next section.

5.3.3 Discussion

The most important assumption we have made is the assumption of universality of the distance indicator used for both local LCBG-like HII galaxies and LCBGs at different epochs. Support for this assumption is provided by the fact that both galaxy populations follow the empirical correlation of Equation 5–1, as shown in Figure 5-7 (Figure 3 of Siegel, Guzmán, Pérez-Gallego, et al., 2005). The validity of the correlation between $L_{\mathrm{H}\beta}$ and M_z can be tested directly to determine its range of applicability. By assuming a cosmology, $\log L_{\mathrm{H}\beta}$ can be written purely in terms of luminosity distance (d_L), $F_{\mathrm{H}\beta}$, and $A_{\mathrm{H}\beta}$, which are either measurable or computable from observables for each galaxy. $\log M_z$ can be determined through measured values for σ and O/H. Comparing the quantities $\log L_{\mathrm{H}\beta}$ and $\log M_z$ then allows a test of the correlation in Equation 5–1 for all galaxies of interest. All available LCBG-like HII galaxies and LCBGs with appropriately measured quantities are included to test the correlation. Local galaxies are taken from MTM and from the UCM catalog (Gallego et al., 1996; Vitores et al., 1996), intermediate LCBGs are taken from Guzmán et al. (1997), and high redshift LCBG-like Lyman-break galaxies are from Pettini et al. (2001) and Erb et al. (2003). The cosmology assumed to test universality is $\Omega_m = 0.3$, $\Omega_\Lambda = 0.7$, and cuts are applied to all samples so that $EW > 20\,\text{Å}$ and $\sigma < 130$ km s^{-1}.

The major reasons to conclude that the assumption of universality is valid lie in Figure 5-7 (Figure 3 of Siegel, Guzmán, Pérez-Gallego, et al., 2005), where these results are shown. There is an overlap between all four samples in both $L_{\mathrm{H}\beta}$ and M_z, from the sample where the correlation is well established (nearby samples, MTM and UCM), to intermediate redshift LCBGs (Guzmán et al., 1997), to the high redshift sample used in this paper, from Erb et al. (2003) and Pettini et al. (2001). These four samples all follow the same correlation between $L_{\mathrm{H}\beta}$ and M_z within the same intrinsic scatter (although

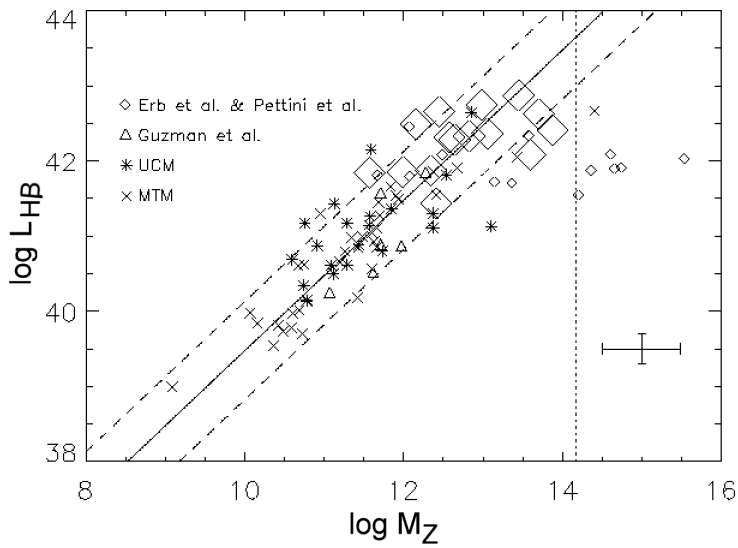

Figure 5-7. $\log M_z$ vs. $\log L_{\mathrm{H}\beta}$ for local HII galaxies and starburst galaxies at intermediate and high redshifts. The solid line is the best fit of the correlation to the local data set, flanked by the dashed lines, which give the 2-σ rms scatter. The large diamonds represent the selected high redshift data sample; the small diamonds are the data not selected on the basis of either EW or σ. The vertical dotted line is the derived cut on σ of 130 km s^{-1}. The crosshairs represents the typical uncertainty in each selected data point.

the observed scatter broadens at high redshifts due to measurement uncertainties). All samples are consistent with the same choice of slope and the same choice of zero-point. For these reasons, the correlation of Equation 5–1 appears to be just as valid for LCBGs as for nearby LCBG-like HII galaxies.

The other assumptions which are inherent to this method are the choices of where to cut on EW and on σ, and the assumption that $A_{\mathrm{H}\beta}$ is the same for starburst galaxies as it is for local HII regions. Moving the EW cut from $EW > 20\,\text{Å}$ up to $EW \geq 25\,\text{Å}$, as suggested in MTT, would systematically raise the DM by 0.14 mag for this sample. On the other hand, a cut on σ at 130 km s^{-1} retains 95% of the valid, single LCBG-like HII galaxies, while eliminating 75% of the contaminating objects. Additionally, it can be shown that the contaminating objects which are not eliminated depart only slightly from the empirical correlation of Equation 5–1. Finally, the derived $A_{\mathrm{H}\beta}$ itself has an uncertainty of ±38%, due to the fact that there are competing extinction laws that

give different results (Gordon et al., 2003; Calzetti et al., 1994, 2000). Both laws are comparably grey, but have different normalizations. The difference between the two laws leads to a systematic uncertainty in the DM of ± 0.17 mag.

There have also been assumptions made specifically to compensate for incomplete data in the Pettini et al. (2001) and Erb et al. (2003) data sets. The systematic uncertainties that these assumptions induce can be eliminated in future surveys through measurements of all required quantities. Future surveys, for example, will allow multiple, independent techniques to be used to measure abundances of high redshift starburst galaxies, significantly reducing errors and overcoming assumptions regarding the O/H of these objects. Uncertainties included in our analysis by means of the measurements of the EW of the galaxies in the Erb et al. (2003) sample will be removed by measuring equivalent widths in Hβ with a higher S/N spectra for all galaxies in future surveys. On the other hand, uncertainties included in our analysis by using an approximate correlation between $E(B-V)$ and the corrected $(G-R)$ colors to derive the extinction for the galaxies in Erb et al. (2003) will be eliminated when $A_{\mathrm{H}\beta}$ measurements are explicity taken for all galaxies.

Random errors, due to both uncertainties in measurement and to the large scatter in the distribution of points, are perhaps the best understood of the sources of error. Measurements of $A_{\mathrm{H}\beta}$ are uncertain by 0.04 to 0.11 dex, depending on the galaxy's brightness. Improved measurements, which rely on the $H\alpha/H\beta$ ratio instead of solely on $E(B-V)$ colors, may reduce the uncertainty significantly. Measurements of $F_{\mathrm{H}\beta}$ are uncertain by roughly 20 to 25% on average, and random uncertainties in O/H are of order 0.10 dex. The largest measurement uncertainty comes from measurements of σ, which is obtained by the broadening of the Balmer emission lines. Even relatively small uncertainties in σ of order 15% can induce uncertainties in DM of 0.8 mag per galaxy. The induced uncertainty is so large because, as seen in Equation 5–2, DM is dependent on σ^5, whereas it depends only linearly on the other quantities. Future work will be able

to measure the Hα and Hβ lines, as well as three oxygen lines, which should improve the measurements of σ, further reducing the random uncertainties. The distribution of points may not improve as statistics improve due to the intrinsic scatter on the M_z vs. $L_{\mathrm{H}\beta}$ relation, but random errors all fall off as the sample size increases. The errors decrease as $N^{-1/2}$, where N is the number of galaxies in the sample. Even if random errors associated with intrinsic properties (such as $F_{\mathrm{H}\beta}$, σ, or O/H) remain large for individual galaxies, increasing the sample size will drive down the overall random errors. Hence, a sample of 500 galaxies, as opposed to 15, will have its random uncertainties reduced by a factor of 6 or better. The new generation of near-IR spectrographs with multi-object capabilities (such as FLAMINGOS and EMIR) in 10-m class telescopes will be ideal for obtaining all necessary measurements for such a sample.

Using LCBGs at high redshift as a standard candle is a promising and well-motivated avenue to explore for precision cosmology. A future survey of high redshift starburst galaxies with measurements of z, σ, $A_{\mathrm{H}\beta}$, $F_{\mathrm{H}\beta}$, O/H, and EW, such as GOYA at the GTC, will reduce both random and systematic errors dramatically. Since the inherent scatter of the method is large, a large sample size is required to obtain meaningful constraints. This paper contains a sample size of only 15 galaxies, but future surveys should be able to obtain hundreds of starburst galaxies that survive the selection cuts. For a sample of 500 galaxies, this will improve constraints on Ω_m to a restriction of ± 0.03 due to random errors. Additionally, all of the systematics specific to this sample due to incomplete data will disappear.

CHAPTER 6
CONCLUSIONS

Luminous Compact Blue Galaxies (LCBGs) are high surface brightness starburst galaxies bluer than a typical SBc spiral galaxy and brighter than $\sim 0.25L^{\star}$ which are undergoing a major burst of star formation. LCBGs are selected to be the closest counterparts of the numerous population of distant starburst galaxies, including Lyman-break galaxies at $z \sim 2$. Therefore, LCBGs in the nearby universe may hold the key to understanding the nature of the distant population and their evolution into today's galaxy population. We have selected a representative sample of 22 LCBGs in the local universe from the Sloan Digital Sky Survey, and the Universidad Complutense de Madrid catalogs, to be observed with an Integral Field Unit (IFU). Three dimensional (3D) optical spectroscopy data provide a complete description of the physical properties of galaxies as a function of spatial position within the galaxy. Although small, this representative sample provides an excellent reference for studying the kinematic properties of LCBGs as a class, and comparing with current and future observations of the distant LCBG population with optical and infrared integral field units in 10- and 30-m class telescopes. In particular, we are able to shed light into the following three fundamental questions about the nature of LCBGs, as well as their formation and evolution.

What is triggering the burst of star formation? From our detailed analysis of velocity and velocity width maps we are able to study the effects that mergers and galaxy pair interactions have on the kinematic properties of LCBGs. Interactions and both major and minor mergers are responsible for the presence of kinematic asymmetries in galaxies.

In particular, velocity and velocity width maps allow us to classify the kinematics of LCBGs between three different classes: rotating disks (RD), perturbed rotation (PR), and complex kinematics (CK). We find 48% RDs, 28% PRs, and 24% CKs. Traditionally, PRs and CKs have been linked to the presence of both minor and major mergers, or galaxy pair interactions. According to this, half of the galaxies in our representative sample (PRs

plus CKs) shows kinematics in agreement with either an interaction or a merging scenario. Furthermore, at least two of the galaxies identified as RDs, show evidence of being a minor merger. On the other hand, 43% of the galaxies in our representative sample are found to have a companion. Interactions in galaxy pairs are able to trigger star formation, and might have been the triggering mechanism of the current burst. All the galaxies in our representative sample with a companion are either classified as PRs or CKs, or show spatially resolved kinematic components. This shows clear evidence of the importance of the effects companions have on the kinematic properties of LCBGs.

Spatially resolved kinematic components are found in 14% of the galaxies in our representative sample. While the kinematic component found in NGC 7714 is linked to a spiral arm, those found in NGC 7673 and UCM 2327 may be proof of a recent minor merger. In particular, the spatially resolved kinematic component found at the location of clump B in NGC 7673, shows no evidence for neither Active Galactic Nuclei (AGN) activity, nor supernova (SN) galactic winds, and is in agreement with being either an extremely giant H II region, or an infalling dwarf galaxy. While we find spatially resolved kinematic components that might due to a minor merger in 10% of the galaxies in our representative sample, proof of an ongoing major merger is found only in one of our galaxies (5% of the sample).

What is the mechanism responsible for quenching star formation and limiting the stellar mass? The star formation may be stopped via heating from massive halos, AGNs and/or SN-driven galactic winds. While halo mass estimates from HI dynamical mass measurements are necessary to study the former, our high resolution 3D optical spectroscopy data provide insight into the latter.

Out of the 22 LCBGs in our representative sample, 21 (95% of the sample) show no evidence AGN activity. This suggest that such a phenomena is not common in LCBGs. On the other hand, one galaxy (5% of the sample) show clear evidence for AGN activity.

UCM 0000 shows both a spectrally resolved broad kinematic component ($\sigma \sim 200$ km s^{-1}) and emission line flux ratios characteristic of an AGN.

On the other hand, 27% of the galaxies in our representative sample show spectrally resolved kinematic components. Even though we cannot unambiguously state the nature of these components, both their intensities and offsets are in agreement with SN-driven galactic winds previously discussed by Marlowe et al. (1995) in a sample of dwarf galaxies with star formation activity. Nevertheless, SN-driven galactic winds do not seem to be typical among our representative sample of local LCBGs either.

What can the study of local LCBGs tell us about the distant population of LCBGs? Again, we find 48% RDs, 28% PRs, and 24% CKs among our representative sample of local LCBGs. These percentages are not in agreement with those found for distant LCBGs (Yang et al., 2008). Nevertheless, our classification is only carried out after a thorough analysis of each object is performed. This analysis allow us to find the rotating nature of LCBGs after removing asymmetries introduced by spatially and spectrally resolved kinematic components. Before this analysis is carried out, the percentages for both the nearby and distant populations are in agreement. It is important to notice that such an analysis is not possible for the distant population of LCBGs because of the intrinsic limitations of observations of distant galaxies.

In particular, only after investigating the velocity and velocity width maps of NGC 6052 we were able to discard the apparently rotating nature of this galaxy. We find that our analysis, together with the double nucleus, the tail, the recent star formation, the large velocity gradients in the extranuclear regions, and the perturbed gas in the whole FOV are all signs of a merger event.

From our detailed analysis of velocity and velocity width maps we conclude that even though most LCBGs show highly asymmetric maps, 48% of these galaxies rotate and both a dynamical center and a position angle can accurately be derived. Using this information we can derive rotational velocities by considering rotation curves along the major axis of

the galaxy. Our data show that for those galaxies for which an analysis of this nature is possible, the ionized gas extends towards the plateaus of the rotation curve at the low surface brightness outskirts of the galaxy. The ionized gas therefore may be a good tracer of the dynamical mass of these rotating galaxies. These galaxies show rotational velocities that range between $\sim$50 and $\sim$200 km s^{-1}, which translates into dynamical masses that range between $\sim 1 \times 10^9$ and $\sim 3 \times 10^{10} M_\odot$. These masses place this galaxy population at the location of the critical stellar mass value observed in the "blue cloud."

Those objects in our representative sample of 22 LCBGs which show rotating natures can be compared with the spiral galaxies used to calibrate the Tully-Fisher Relation (TFR; Tully & Pierce, 2000). We find that LCBGs, like spiral galaxies, show a correlation between direct measurements of their rotational velocities and estimates from their integrated velocity widths. Nevertheless, a dispersion five times bigger than the one found for spiral galaxies implies that the velocity widths of those LCBGs that rotate, rather than accounting exclusively for this rotation, may account as well for other kinematic components.

Therefore, an accurate estimation of the dynamical mass of these objects is needed. When compared, dynamical masses derived from rotation curves and integrated velocity widths differ in our representative sample of LCBGs up to a factor of $\sim$4. Such a difference may have an important impact on the study of distant LCBGs when observed through multi-object long-slit spectrographs. These kind of surveys rely on integrated spectral measurements to derive different physical properties, such as dynamical masses.

Furthermore, LCBGs show larger M_B for a particualr rotational velocity than spiral galaxies. Therefore, their mass-to-light ratios are lower that those found for the latter. By combining the dynamical masses and the absolute B-magnitudes of LCBGs, we find $M/L_B \sim 0.6$. Such a lower value is in agreement with those found for late-type galaxies (Dickel & Rood, 1978).

Finally, we have showed the importance and true potential of using a representative sample of local LCBGs as a key reference for high redshift studies. Reliable simulations of the different galaxies in our sample can help understand the properties of the distant population of blue galaxies. These simulations, for example, can shed light into the possibility or not of detecting minor mergers among the distant population. Furthermore, an understanding of the integrated properties of LCBGs is also necessary, for example, to improve the work of Siegel, Guzmán, Pérez-Gallego, et al. (2005) on a powerful standard candle that relies on accurate measurements of the fluxes and velocity widths of these galaxies at different redshifts.

REFERENCES

Abraham, R. G., van den Bergh, S., Glazebrook, K., Ellis, R. S., Santiago, B. X., Surma, P., & Griffiths, R. E. 1996, ApJS, 107, 1

Adelman-McCarthy, J. K., et al. 2006, ApJS, 162, 38

Alloin, D., & Duflot, R. 1979, A&A, 78, L5

Arnouts, S., Schiminovich, D., Ilbert, O., Tresse, L., et al. 2005, ApJ, 619, L43

Arp, H. 1966, Atlas of Peculiar Galaxies (Pasadena: California Inst. Technology)

Bahcall, N. A., Dong, F., Bode, P., Kim, R., et al. 2003, ApJ, 585, 182B

Baldry, I. K., Glazebrook, K., Brinkmann, J., Ivezić, Ž., Lupton, R. H., Nichol, R. C., & Szalay, A. S. 2004, ApJ, 600, 681

Baldwin, J. A., Phillips, M. M., & Terlevich, R. 1981, PASP, 93, 5

Balogh, M. L., Baldry, I. K., Nichol, R., Miller, C., Bower, R., & Glazebrook, K. 2004, ApJ, 615, L101

Barton, E. J., & van Zee, L. 2001, ApJ, 550, L35

Barton, E. J., van Zee, L., & Bershady, M. A. 2006, ApJ, 649, 129

Bell, E. F., McIntosh, D. H., Katz, N., & Weinberg, M. D. 2003, ApJS, 149, 289

Bell, E .F., Wolf, C., Meisenheimer, K., Rix, H.-W., Borch, A., Dye, S., Kleinheinrich, M., Wisotzki, L., McIntosh, Daniel H., et al. 2004, ApJ, 608, 752

Bell, E. F., Papovich, C., Wolf, C., Le Floc'h, E., et al. 2005, ApJ, 625, 23

Bennett, C. L., Hill, R. S., Hinshaw, G., Nolta, M. R., et al. 2003, ApJS, 148, 1B

Bernloehr, K. 1993, A&A, 268, 25

Blanton, M. R., Hogg, D. W., Bahcall, N. A., Baldry, I. K., et al. 2003, ApJ, 594, 186

Blanton, M. R., Eisenstein, D., & Hogg, D. W., & Zehavi, I. 2006, ApJ, 645, 977

Borgani, S., Rosati, P., Tozzi, P., Stanford, S. A., Eisenhardt, P. R., Lidman, C., Holden, B., della Ceca, R., Norman, C., Squires, G. 2001, ApJ, 561, 13B

Bouwens, R. J., Illingworth, G. D., Thompson, R. I., Blakeslee, J. P., Dickinson, M. E., Broadhurst, T. J., Eisenstein, D. J., Fan, X., Franx, M., Meurer, G., van Dokkum, P., et al. 2004, ApJ, 606, L25

Brinchmann, J., Charlot, S., White, S. D. M., Tremonti, C., Kauffmann, G., Heckman, T., & Brinkmann, J. 2004, MNRAS, 351, 1151

Bunker, A. J., Stanway, E. R., Ellis, R. S., & McMahon, R. G. 2004, MNRAS, 355, 374

Burenkov, A. N. 1988, Astrofizika, 28, 47

Cairós, L. M., Caon, N., Vílchez, J. M., González-Pérez, J. N., & Muñoz-Tuñón, C. 2001, ApJS, 136, 393

Calzetti D., Kinney A. L., & Storchi-Bergmann T. 1994, ApJ, 429, 582C

Calzetti D., Armus L., Bohlin R. C., Kinney A. L., Koornneef J., & Storchi-Bergmann T. 2000, ApJ, 533, 682

Capak, P., Abraham, R. G., Ellis, R. S., Mobasher, B., Scoville, N., Sheth, K., & Koekemoer, A. 2007, ApJS, 172, 284

Castander, F. J., Guzmán, R., Pérez-Gallego, J., Garland, C. A., Pisano, D. J., & Gruel, N. 2009, in preparation

Castillo-Morales, A., Gallego, J., Pérez-Gallego, J., Guzmán, R., & Muñoz-Mateos, J. C. 2009a, A&A, submitted

Castillo-Morales, A., Gallego, J., Pérez-Gallego, J., Guzmán, R., & Muñoz-Mateos, J. C. 2009b, A&A, in preparation

Castillo-Morales, A., Gallego, J., Pérez-Gallego, J., Guzmán, R., & Muñoz-Mateos, J. C. 2010, A&A, in preparation

Cattaneo, A., Dekel, A., Devriendt, J., Guiderdoni, B., & Blaizot, J. 2006, MNRAS, 370, 1651

Cox, T. J., Dutta, S. N., Di Matteo, T., Hernquist, L., Hopkins, P. F., Robertson, B., & Springel, V. 2006, ApJ, 650, 791

Cumming, R. J., Fathi, K., Östlin, G., Marquart, T., Márquez, I., Masegosa, J., Bergvall, N., & Amram, P. 2008, A&A, 479, 725

de Bernardis, P., Ade, P. A. R., Bock, J. J., Bond, J. R., et al. 2000, Nature, 404, 955

De Rijcke, S., Prugniel, P., Simien, F., & Dejonghe, H. 2006, MNRAS, 369, 1321

de Vaucouleurs, G., de Vaucouleurs, A., Corwin, H. G., Jr., Buta, R. J., Paturel, G., & Fouque, P. 1991, Third Reference Catalog of Bright Galaxies (New York: Springer-Verlag)

Dickel, J. R., & Rood, H. J. 1978, ApJ, 223, 391

Dressler, A., & Gunn, J. E. 1983, ApJ, 270, 7

Driver, S. P., Fernandez-Soto, A., Couch, W. J., Odewahn, S. C., Windhorst, R. A., Phillips, S., Lanzetta, K., & Yahil, A. 1998, ApJ, 496, L93

Duflot-Augarde, R., & Alloin, D. 1982, A&A, 112, 257

Elmegreen, D. M., Elmegreen, B. G., Rubin, D. S., & Schaffer, M. A. 2005, ApJ, 631, 85

Epinat, B., Contini, T., Le Fèvre, O., Vergani, D., Amram, P., Garilli, B., Queyrel, J., Kissler-Patig, M., Tasca, L., & Tresse, L. 2009, A&A, in press

Erb D. K., Shapley A. E., Steidel C. C., Pettini M., Adelberger K. L., Hunt M. P., Moorwood A. F. M., & Cuby J.-G. 2003, ApJ, 591, 110

Faber, S. M., Willmer, C. N. A., Wolf, C., Koo, D. C., et al. 2007, ApJ, 665, 265

Feldman, H., Juszkiewicz, R., Ferreira, P., Davis, M., et al. 2003, ApJ, 596L, 131F

Ferguson, H. C., Ravindranath, S., Giavalisco, M., Mobasher, B., et al. 2004, ApJ, 600, L107

Förster Schreiber, N. M., Genzel, R., Lehnert, M. D., Bouché, N., et al. 2006, ApJ, 645, 1062

Förster Schreiber, N. M., Genzel, R., Bouche, N., Cresci, G., et al. 2009, arXiv:0903.1872

Freedman, W. L., Madore, B. F., Gibson, B. K., Ferrarese, L., et al. 2001, ApJ, 553, 47F

Gallego J., Zamorano J., Rego M., Alonso O., & Vitores A. G. 1996, A&AS, 120, 323G

García-Lorenzo, B., Cairós, L. M., Caon, N., Monreal-Ibero, A., & Kehrig, C. 2008, ApJ, 677, 201

Garcia-Vargas, M. L., Gonzalez-Delgado, R. M., Perez, E., Alloin, D., Diaz, A., & Terlevich, E. 1997, ApJ, 478, 112

Garland, C. A., Pisano, D. J., Williams, J. P., Guzmán, R., & Castander, F. J. 2004, ApJ, 615, 689

Garland, C. A., Williams, J. P., Pisano, D. J., Guzmán, R., Castander, F. J., & Brinkmann, J. 2005, ApJ, 624, 714

Garland, C. A., Pisano, D. J., Williams, J. P., Guzmán, R., Castander, F. J., & Sage., L.J. 2007, ApJ, 671, 310

Gil de Paz, A., Aragón-Salamanca, A., Gallego, J., Alonso-Herrero, A., Zamorano, J., & Kauffmann, G. 2000, MNRAS, 316, 357

Gil de Paz, A., Madore, B. F., Sohn, Y.-J., Lee, Y.-W., et al. 2005, ApJ, 619, L115

Gil de Paz, A., Boissier, S., Madore, B. F., Seibert, M., et al. 2007, ApJS, 173, 185

González-Delgado, R. M., Perez, E., Diaz, A. I., Garcia-Vargas, M. L., Terlevich, E., & Vilchez, J. M. 1995, ApJ, 439, 604

González Delgado, R. M., García-Vargas, M. L., Goldader, J., Leitherer, C., & Pasquali, A. 1999, ApJ, 513, 707

Gordon K. D., Clayton G. C., Misselt K. A., Landolt A. U., & Wolff M. J. 2003, ApJ, 594, 279

Granato, G. L., De Zotti, G., Silva, L., Bressan, A., & Danese, L. 2004, ApJ, 600, 580

Grego L., Carlstrom J. E., Reese E. D., Holder G. P., Holzapfel W. L., Joy M. K., Mohr J. J., & Patel S. 2001, ApJ, 522, 2G

Gronwall, C. 1999, After the Dark Ages: When Galaxies were Young (Maryland: American Institute of Physics Press)

Gruel, N., Guzmán, R., & Pérez-Gallego, J. 2009a, A&A, in preparation

Guzmán, R., Koo, D. C., Faber, S. M., Illingworth, G. D., Takamiya, M., Kron, R. G., & Bershady, M. A. 1996, ApJ, 460, L5

Guzmán, R., Gallego, J., Koo, D. C., Phillips, A. C., Lowenthal, J. D., Faber, S. M., Illingworth, G. D., & Vogt, N. P. 1997, ApJ, 489, 559

Guzmán, R., Jangren, A., Koo, D. C., Bershady, M. A., & Simard, L. 1998, ApJ, 495, L13

Guzmán, R., Östlin, G., Kunth, D., Bershady, M. A., Koo, D. C., & Pahre, M. A. 2003, ApJ, 586, L45

Hagiwara, K., Hikasa, K., Nakamura, K., Tanabashi, M., et al. 2002, Phys. Rev. D, 66, 010001

Hammer, F., Gruel, N., Thuan, T. X., Flores, H., & Infante, L. 2001, ApJ, 550, 570

Hawkins, E., Maddox, S., Cole, S., Lahav, O., Madgwick, D. S., et al. 2003, MNRAS, 346, 78H

Heidmann, J. 1987, Star Forming Regions (Dordrecht: D. Reidel Publishing Co.)

Hoekstra, H., Franx, M., Kuijken, K., Carlberg, R. G., Yee, H. K. C., Lin, H., Morris, S. L., Hall, P. B., Patton, D. R., Sawicki, M., Wirth, G. D. 2001, ApJ, 548L, 5H

Hopkins, P. F., Somerville, R. S., Hernquist, L., Cox, T. J., Robertson, B., & Li, Y. 2006, ApJ, 652, 864

Hogg, D. W., Cohen, J. G., Blandford, R., & Pahre, M. A. 1998, ApJ, 504, 622

Hogg, D. W., Blanton, M. R., Eisenstein, D. J., Gunn, J. E., et al. 2003, ApJ, 585, L5

Hogg, D. W., Blanton, M. R., Brinchmann, J., Eisenstein, D. J., Schlegel, D. J., Gunn, J. E., McKay, T. A., Rix, H.-W., Bahcall, N.A., Brinkmann, J., Meiksin, A. 2004, ApJ, 601, L29

Homeier, N. L., & Gallagher, J. S. 1999, ApJ, 522, 199

Homeier, N., Gallagher, J. S., III, & Pasquali, A. 2002, A&A, 391, 857

Hopkins, A. M. 2004, ApJ, 615, 209

Howk, J. C., & Savage, B. D. 2000, AJ, 119, 644

Hoyos, C., Koo, D. C., Phillips, A. C., Willmer, C. N. A., & Guhathakurta, P. 2005, ApJ, 635, L21

Huchra, J. P., Vogeley, M. S., & Geller, M. J. 1999, ApJS, 121, 287

Ilbert, O., Lauger, S., Tresse, L., Buat, V., et al. 2006, A&A, 453, 809

Im, M., Faber, S. M., Gebhardt, K., Koo, D. C., Phillips, A. C., Schiavon, R. P., Simard, L., & Willmer, C. N. A. 2001, AJ, 122, 750

James, P. A., O'Neill, J., & Shane, N. S. 2008, A&A, 486, 131

Jogee, S., Scoville, N., & Kenney, J. D. P. 2005, ApJ, 630, 837

Kannappan, S. J. 2004, ApJ, 611, L89

Kauffmann, G., Heckman, T. M., White, S. D. M., Charlot, S., Tremonti, C., Peng, E. W., Seibert, M., Brinkmann, J., Nichol, R. C., Subbarao, M., York, D. 2003, MNRAS, 341, 54

Kelz, A., Verheijen, Marc A. W., Roth, M. M., Bauer, S. M., Becker, T., Paschke, J., Popow, E., Snchez, S. F., Laux, U. 2006, PASP, 118, 129

Kennicutt, R. C., Jr. 1998, ApJ, 498, 541

Kewley L. J., & Dopita M. A. 2002, ApJS, 142, 35K

Knop, R. A., Aldering, G., Amanullah, R., Astier, P., et al. 2003, ApJ, 598, 102K

Kobulnicky H. A., & Koo D. C. 2000, ApJ, 545, 712

Koo, D. C., Bershady, M. A., Wirth, G. D., Stanford, S. A., & Majewski, S. R. 1994, ApJ, 427, L9

Koo, D. C., Guzmán, R., Faber, S. M., Illingworth, G. D., Bershady, M. A., Kron, R. G., & Takamiya, M. 1995, ApJ, 440, L49

Kunth, D., Östlin, G. 2000, A&A Rev., 10, 1

Lançon, A., Goldader, J. D., Leitherer, C., & Delgado, R. M. G. 2001, ApJ, 552, 150

Le Fèvre, O., Abraham, R., Lilly, S. J., Ellis, R. S., et al. 2000, MNRAS, 311, 565

Lilly, S. J., Le Fèvre, O., Hammer, F., & Crampton, D. 1996, ApJ, 460, L1

Lilly, S., Schade, D., Ellis, R., Le Fèvre, O., et al. 1998, ApJ, 500, 75

Lilly, S. J., Le Fèvre, O., Renzini, A., Zamorani, G., et al. 2007, ApJS, 172, 70

Liu, C. T., & Green, R. F. 1998, AJ, 116, 1074

Lowenthal, J. D., Koo, D. C., Guzmán, R., Gallego, J., Phillips, A. C., Faber, S. M., Vogt, N. P., Illingworth, G. D., Gronwall, C. 1997, ApJ, 481, 673

Madau, P., & Shull, J. M. 1996, ApJ, 457, 551

Madau, P., Pozzetti, L., & Dickinson, M. 1998, ApJ, 498, 106

Malhotra, S., Rhoads, J. E., Pirzkal, N., Haiman, Z., et al. 2005, ApJ, 626, 666

Mallén-Ornelas, G., Lilly, S. J., Crampton, D., & Schade, D. 1999, ApJ, 518, L83

Markarian, B. E., Lipovetsky, V. A., Stepanian, J. A., Erastova, L. K., & Shapovalova, A. I. 1989, Soob. Spets. Astrofiz. Obs., 62, 5

Marlowe, A. T., Heckman, T. M., Wyse, R. F. G., & Schommer, R. 1995, ApJ, 438, 563

Martínez-Delgado, I., Muoz-Tun, C., Cairs, L. M., & Tenorio-Tagle, G. 2008, ApJ, submitted

Melbourne, J., Phillips, A. C., Harker, J., Novak, G., Koo, D. C., & Faber, S. M. 2007, ApJ, 660, 81

Melnick J. 1978, A&A, 70, 157

Melnick, J., Moles, M., Terlevich, R., & Garcia-Pelayo, J.-M. 1987, MNRAS, 226, 849

Melnick J., Terlevich R., & Moles M. 1988, MNRAS, 235, 313M

Melnick J., Terlevich R., & Terlevich E. 2000, MNRAS, 311, 629

Metcalfe, L., O'Halloran, B., McBreen, B., Delaney, M., et al. 2005, A&A, 444, 777

Mihos, J. C., & Hernquist, L. 1994, ApJ, 427, 112

Mihos, J. C., & Hernquist, L. 1996, ApJ, 464, 641

Murray, N., Quataert, E., & Thompson, T. A. 2005, ApJ, 618, 569

Noeske, K. G., Koo, D. C., Phillips, A. C., Willmer, C. N. A., Melbourne, J., Gil de Paz, A., & Papaderos, P. 2006, ApJ, 640, L143

Noeske, K. G., Weiner, B. J., Faber, S. M., Papovich, C., et al. 2007, ApJ, 660, L43

Nordgren, T. E., Chengalur, J. N., Salpeter, E. E., & Terzian, Y. 1997, AJ, 114, 77

Obrić, M., et al. 2006, MNRAS, 370, 1677

Osterbrock, D. E. 1989, Astrophysics of Gaseous Nebulae and Active Galactic Nuclei (Mill Valley: Univ. Science Books)

Östlin, G., Amram, P., Bergvall, N., Masegosa, J., Boulesteix, J., & Márquez, I. 2001, A&A, 374, 800

Östlin, G., Cumming, R. J., Amram, P., Bergvall, N., Kunth, D., Márquez, I., Masegosa, J., & Zackrisson, E. 2004, A&A, 419, L43

Papaderos, P., Izotov, Y. I., Fricke, K. J., Thuan, T. X., & Guseva, N. G. 1998, A&A, 338, 43

Pasquali, A., & Castangia, P. 2008, MNRAS, 183

Patel B. E. J., Edmunds M. G., Blackwell D. E., Chun M. S., & Smith, G. 1979, MNRAS, 189, 95

Pei, Y. C., & Fall, S. M. 1995, ApJ, 454, 69

Pei, Y. C., Fall, S. M., & Hauser, M. G. 1999, ApJ, 522, 604

Pérez-Gallego, J., Guzmán, R., Castillo-Morales, A., R., Castander, F. J., Gallego, J., Garland, C. A., Gruel, N., Pisano, D. J., Sánchez, S. F., & Zamorano, J. 2009a, A&A, submitted

Pérez-Gallego, J., Guzmán, R., Castillo-Morales, A., R., Castander, F. J., Gallego, J., Garland, C. A., Gruel, N., Pisano, D. J., & Zamorano, J. 2009b, A&A, in preparation

Pérez-Gallego, J., Guzmán, R., Castillo-Morales, A., R., Castander, F. J., Gallego, J., Garland, C. A., Gruel, N., Pisano, D. J., & Zamorano, J. 2009b, A&A, in preparation

Pérez-González, P. G., Gallego, J., Zamorano, J., Alonso-Herrero, A., Gil de Paz, A., & Aragón-Salamanca, A. 2003, ApJ, 587, L27

Pettini M., Shapley A. E., Steidel C. C., Cuby J.-G., Dickinson M., Moorwood A. F. M., Adelberger K. L., & Giavalisco M. 2001, ApJ, 554, 981

Pettini, M., & Pagel, B. E. J. 2004, MNRAS, 348, L59

Phillips, A. C., Guzman, R., Gallego, J., Koo, D. C., Lowenthal, J. D., Vogt, N. P., Faber, S. M., & Illingworth, G. D. 1997, ApJ, 489, 543

Pisano, D. J., Kobulnicky, H. A., Guzmán, R., Gallego, J., & Bershady, M. A. 2001, AJ, 122, 1194

Pisano, D. J., Wilcots, E. M., & Liu, C. T. 2002, ApJS, 142, 16

Pisano, D. J., Garland, Pérez-Gallego, J., C. A., Guzmán, R., Castander, F. J., & Gruel, N. 2009a, in preparation

Pisano, D. J., Garland, C. A., Pérez-Gallego, J., Guzmán, R., Castander, F. J., & Gruel, N. 2009b, in preparation

Prugniel, P., & Maubon, G. 2000, 197, 403

Puech, M., Hammer, F., Flores, H., Östlin, G., & Marquart, T. 2006, A&A, 455, 119

Puech, M., Flores, H., Lehnert, M., Neichel, B., Fusco, T., Rosati, P., Cuby, J.-G., & Rousset, G. 2008, MNRAS, 390, 1089

Rawat, A., Kembhavi, A. K., Hammer, F., Flores, H., & Barway, S. 2007, A&A, 469, 483

Rickes, M. G., Pastoriza, M. G., & Bonatto, C. 2008, MNRAS, 384, 1427

Riess, A. G., Filippenko, A. V., Liu, M. C., Challis, P., et al. 2000, PASP, 112, 1284R

Richer, M. G., & McCall, M. L. 1995, ApJ, 445, 642

Salpeter, E. E. 1955, ApJ, 121, 161

Sanders, D. B., & Mirabel, I. F. 1996, ARA&A, 34, 749

Sánchez, S. F. 2006, Astronomische Nachrichten, Vol.327, Issue 9, p.850

Sánchez, S. F., Aceituno, J., Thiele, U., Pérez-Ramírez, D., & Alves, J. 2007, PASP, 119, 1186

Schiminovich, D., Ilbert, O., Arnouts, S., Milliard, B., et al. 2005, ApJ, 619, L47

Schuecker P., Böhringer H., Collins C. A., & Guzzo L. 2003, A&A, 398, 8675

Scoville, N., Aussel, H., Benson, A., Blain, A., et al. 2007, ApJS, 172, 150

Shapley, A. E., Steidel, C. C., Adelberger, K. L., Dickinson, M., Giavalisco, M., & Pettini, M. 2001, ApJ, 562, 95

Shapley, A. E., Erb, D. K., Pettini, M., Steidel, C. C., & Adelberger, K. L. 2004, ApJ, 612, 108

Siegel, E. R., Guzmán, R., Gallego, J. P., Orduña López, M., & Rodríguez Hidalgo, P. 2005, MNRAS, 356, 1117

Smith, D. A., Neff, S. G., Bothun, G. D., Fanelli, M. N., Offenberg, J. D., Waller, W. H., Bohlin, R. C., O'Connell, R. W., Roberts, M. S., Smith, A. M., Stecher, Theodore P. 1996, ApJ, 473, L21

Smith, B. J., Struck, C., & Pogge, R. W. 1997, ApJ, 483, 754

Solomon, P. M., & Sage, L. J. 1988, ApJ, 334, 613

Springel, V., Di Matteo, T., & Hernquist, L. 2005, MNRAS, 361, 776

Steidel, C. C., Giavalisco, M., Pettini, M., Dickinson, M., & Adelberger, K. L. 1996, ApJ, 462, L17

Steidel, C. C., Adelberger, K. L., Giavalisco, M., Dickinson, M., & Pettini, M. 1999, ApJ, 519, 1

Steidel, C. C., Pettini, M., & Adelberger, K. L. 2001, ApJ, 546, 665

Steidel, C. C., Adelberger, K. L., Shapley, A. E., Pettini, M., Dickinson, M., & Giavalisco, M. 2003, ApJ, 592, 728

Struck, C., & Smith, B. J. 2003, ApJ, 589, 157

Sullivan, M., Treyer, M. A., Ellis, R. S., Bridges, T. J., Milliard, B., & Donas, J. 2000, MNRAS, 312, 442

Taniguchi, Y., & Tamura, S. 1987, A&A, 181, 265

Taniguchi, Y., & Noguchi, M. 1991, AJ, 101, 1601

Terlevich R., & Melnick J. 1981, MNRAS, 195, 839

Thomas, D., Maraston, C., & Korn, A. 2004, MNRAS, 351, L19

Tresse, L., & Maddox, S. J. 1998, ApJ, 495, 691

Tresse, L., Maddox, S. J., Le Fèvre, O., & Cuby, J.-G. 2002, MNRAS, 337, 369

Tully, R. B., & Fouque, P. 1985, ApJS, 58, 67

Tully, R. B., & Fisher, J. R. 1988, Catalog of Nearby Galaxies (UK: Cambridge University Press)

Tully, R. B., & Pierce, M. J. 2000, ApJ, 533, 744

van Zee, L., Skillman, E. D., & Haynes, M. P. 2004, AJ, 128, 121

Vergani, D., Scodeggio, M., Pozzetti, L., Iovino, A., et al. 2008, A&A, 487, 89

Vitores A. G., Zamorano J., Rego M., Alonso O., & Gallego J. 1996, A&AS, 118, 7V

Weedman, D. W., Feldman, F. R., Balzano, V. A., Ramsey, L. W., Sramek, R. A., & Wuu, C.-C. 1981, ApJ, 248, 105

Weedman, D. W. 1983, ApJ, 266, 479

Weiner, B. J.; Phillips, A. C.; Faber, S. M.; Willmer, Christopher N. A., et al. 2005, ApJ, 620, 595

Werk, J. K., Jangren, A., & Salzer, J. J. 2004, ApJ, 617, 1004

Whelan, D. G., Devost, D., Charmandaris, V., Marshall, J. A., & Houck, J. R. 2007, ApJ, 666, 896

Wilson, G., Cowie, L. L., Barger, A. J., & Burke, D. J. 2002, AJ, 124, 1258

Wolf, C., Bell, E. F., McIntosh, D. H., Rix, H.-W., et al. 2005, ApJ, 630, 771

Yang, Y., Flores, H., Hammer, F., Neichel, B., et al. 2008, A&A, 477, 789

Yoshii, Y., & Arimoto, N. 1987, A&A, 188, 13

Young, L. M., & Lo, K. Y. 1997, ApJ, 476, 127

Zamojski, M. A., Schiminovich, D., Rich, R. M., Mobasher, B., et al. 2007, ApJS, 172, 468

Zamorano, J., Rego, M., Gallego, J. G., Vitores, A. G., Gonzalez-Riestra, R., & Rodriguez-Caderot, G. 1994, ApJS, 95, 387

Zucca, E., Ilbert, O., Bardelli, S., Tresse, L., et al. 2006, A&A, 455, 879

BIOGRAPHICAL SKETCH

Jorge Pérez Gallego was born in 1980, in the city of Terrassa, in the province of Barcelona, Spain.

He was born into a humble, but happy, family home. He is son of Constantino and Trinidad, and brother of Nuria. Apart from being his family and house mates, together with his maternal grand mother, who also lived at the house, they are also his best friends.

He grew up in Can Parellada, a little neighborhood where everyone knew him because everyone knew either his father or his mother. He played everlasting soccer matches and had epic adventures in the streets of Can Parellada. With him, there was always his inseparable neighbor. They have been friends since they were born and they will always be.

He does not remember crying the first time he went to school, when he was four years old. For ten years he studied at the Colegio Público Francesc Aldea, known in Terrassa for being shaped after a ship. Still today, he retains good memories from those years, most of them, related to his classmates. Three of them, he will never forget, two who are no longer among us, and a third one that has always time for him when life brings him back home.

Because of his early academic success, he changed from a public elementary school from the outskirts of Terrassa to a downtown renowned high school. Even though he felt out of place at the beginning in a new environment, early enough he found himself enjoying this new opportunity. It was then, when he laid the foundations of who he is today. He still remembers his classmates and professors. Among those, four have been walking with him ever since: the Three Musketeers and John the Fearless

It was then when he started working at an auto electric shop under the supervision of, literally, the greatest man on Earth, an enlightened being. During those days he learned how to make good contacts both with corporation businessmen and petty thieves. Furthermore, he also worked as a warehouse keeper and at a cinema, where he watched as many movies as he could.

Before going to college he considered three majors: aeronautical engineering, physical education, and physics. He finally decided to major in the latter, mainly because of the influence of two of his professors, one from his elementary school years, one from his high school years. He also thought about being a graphic designer, but, for the time being, he decided to park that impulse.

He went to the Universitat Autònoma de Barcelona for three years before he transfered to the Universidad de La Laguna. While in the Universitat Autònoma de Barcelona, he met one of his best friends. Nevertheless, he decided to turn his physics major into a physics and astrophysics major, and after learning about the Universidad de La Laguna program through another friend of his, he left for the Canary Islands.

He graduated from the Universidad de La Laguna after two more intense years in every possible aspect. Two years that he shared with the A Team, the Fairy Goodmother, and a kiss. Following his undergraduate advisor's piece of advice he applied for graduate school at the University of Florida.

He has always liked to travel. Before going to Gainesville, Florida, United States of America, he had traveled as much as he could around Europe: Italy, France, Belgium, Holland, Portugal, Andorra, etc. Like a good friend of his, his graduate school office mate, says, traveling opens your mind. He learned a lot in Gainesville, not only about astronomy, but also about life, and about himself.

After two demanding years he got a Master of Science and decided to keep working on an amazing journey towards a Doctor of Philosophy degree, under the supervision of a great adviser and better person.

And now, after being granted with a Doctor of Philosophy degree in Astronomy from the University of Florida, it is time for him to decide what he wants to do with his life. And, once again, it is an easy decision.